Ni-RICH $LiNi_xMn_yCo_zM_vO_2$ (X>0.6) CATHODE MATERIAL DEVELOPMENT FOR LI-ION BATTERIES

A THESIS SUBMITTED TO
THE GRADUATE SCHOOL OF NATURAL AND APPLIED SCIENCES
OF
MIDDLE EAST TECHNICAL UNIVERSITY

BY

MUSTAFA ALP YILDIRIM

IN PARTIAL FULFILLMENT OF THE REQUIREMENTS
FOR
THE DEGREE OF MASTER OF SCIENCE
IN
METALLURGICAL AND MATERIALS ENGINEERING

SEPTEMBER 2022

Approval of the thesis:

Ni-RICH $LiNi_xMn_yCo_zM_vO_2$ (X>0.6) CATHODE MATERIAL DEVELOPMENT FOR LI-ION BATTERIES

submitted by **MUSTAFA ALP YILDIRIM** in partial fulfillment of the requirements for the degree of **Master of Science** i**n Metallurgical and Materials Engineering, Middle East Technical University** by,

Prof. Dr. Halil Kalıpçılar
Dean, Graduate School of **Natural and Applied Sciences** _____

Prof. Dr. Ali Kalkanlı
Head of the Department, **Metallurgical and Materials Eng.** _____

Prof. Dr. M. Kadri Aydınol
Supervisor, **Metallurgical and Materials Eng., METU** _____

Examining Committee Members:

Prof. Dr. Emren Nalbant
Chemical Eng., METU _____

Prof. Dr. M. Kadri Aydınol
Metallurgical and Materials Eng., METU _____

Prof. Dr. Zafer Evis
Engineering Sciences, METU _____

Assoc. Prof. Dr. Burak Ülgüt
Chemistry, Bilkent Uni. _____

Assoc. Prof. Dr. Harun Koku
Chemistry, METU _____

Date: 01.09.2022

I hereby declare that all information in this document has been obtained and presented in accordance with academic rules and ethical conduct. I also declare that, as required by these rules and conduct, I have fully cited and referenced all material and results that are not original to this work.

Name Last name : Mustafa Alp Yıldırım

Signature :

ABSTRACT

NI-RICH $LiNi_xMn_yCo_zM_vO_2$ (X>0.6) CATHODE MATERIAL DEVELOPMENT FOR LI-ION BATTERIES

Yıldırım, Mustafa Alp
Master of Science, Metallurgical and Materials Engineering
Supervisor : Prof. Dr. Mehmet Kadri Aydınol

September 2022, 102 pages

The nickel-rich lithium nickel manganese cobalt oxide (NMC) cathode materials are the driving force of Lithium-ion batteries. Despite the high capacity and high energy they offer, their structural stability needs to be improved. The production method and element doping are among prominent research topics in the studies to increase the structural stability of the Ni-rich NMC materials.

In this study, Ni-rich $LiNi_xMn_yCo_zO_2$ (x>0.6) and Ni-rich $Li(NMC)_{1-v}Nb_vO_2$ (v=0.2, 0.4, 0.8) were produced using the citric acid assisted Pechini sol-gel method. The physical and chemical properties of pure and niobium doped materials with different nickel, manganese, and cobalt ratios were examined and compared. Discharge capacities, discharge energies, and discharge capacity retentions of all materials at 0.1 C were examined, and impedance changes before and after the cycles were compared. Also, the rate capability tests of the materials at 0.3 C and 1 C were examined.

In XRD analysis, it was seen that $LiNi_xMn_yCo_zO_2$ (x>0.6) samples were produced successfully. In XRD analyzes of $Li(NMC)_{1-v}Nb_vO_2$ (v=0.2, 0.4, 0.8) samples, it was understood that Li_3NbO_4 phase was formed as a secondary phase besides the $LiNi_xMn_yCo_zO_2$ phase.

In the capacity tests performed at 0.1 C during the electrochemical performance test process, the first discharge capacities increased as the nickel content in the material increased. At the end of 20 cycles, the capacity retention decreased as the nickel content in the structure increased. It was observed that the initial discharge capacities of the niobium doped materials were lower than those of the undoped ones. After 20 cycles at 0.1 C, the capacity retentions of the doped ones were higher than the undoped ones. In the tests carried out at 0.3 C, the niobium doped and undoped materials showed similarity with the tests carried out at 0.1 C. In the capacity tests carried out at 1 C, there was no difference between the capacity retentions of the undoped materials and the capacity retentions of the niobium doped materials. However, in the cycle tests performed at 1 C, the materials showed higher capacity retention as the nickel ratio in the structure increased.

Keywords: Lithium-Ion Battery, Nickel Rich NMC, Niobium Doped, Sol-Gel Method, Cathode Active Material

ÖZ

Lİ-İYON BATARYALAR İÇİN Nİ-ZENGİN $LiNi_xMn_yCo_zM_vO_2$ (X>0.6) KATOT MALZEME GELİŞTİRME

Yıldırım, Mustafa Alp
Yüksek Lisans, Metalürji ve Malzeme Mühendisliği
Tez Yöneticisi: Prof. Dr. Mehmet Kadri Aydınol

Eylül 2022, 102 sayfa

Nikelce zengin NMC katot malzemeleri lityum iyon pillerin itici gücü konumundadır. Sundukları yüksek kapasite ve yüksek enerjiye rağmen yapısal kararlılıklarının iyileştirilmesi gerekmektedir. Ni bakımından zengin NMC malzemelerin yapısal kararlılığını arttırmaya yönelik çalışmalarda üretim yöntemi ve element katkılama öne çıkan araştırma konuları arasındadır.

Bu çalışmada sitrik asit destekli Pechini sol-jel metodu kullanılarak nikelce zengin $LiNi_xMn_yCo_zO_2$ (x>0.6) ve nikelce zengin $Li(NMC)_{1-v}Nb_vO_2$ (v=0.2, 0.4, 0.8) üretildi. Nikel, mangan ve kobalt oranları farklı olan saf ve niobyum katkılı malzemelerin fiziksel ve kimyasal özellikleri incelendi ve karşılaştırıldı. Tüm malzemelerin 0,1 C'deki deşarj kapasiteleri, deşarj enerjileri, deşarj kapasite korunumları incelendi ve çevrim öncesi ile sonrası empedans değişimleri karşılaştırıldı. Ayrıca malzemelerin 0,3 C ve 1 C'deki deşarj kabiliyet testleri incelendi.

XRD analizlerinde $LiNi_xMn_yCo_zO_2$ (x>0.6) numunelerin başarılı bir şekilde üretildiği görüldü. $Li(NMC)_{1-v}Nb_vO_2$ (v=0.2, 0.4, 0.8) numunelerinin XRD

analizlerinde ise $LiNi_xMn_yCo_zO_2$ fazının yanında ikincil faz olarak Li_3NbO_4 fazının oluştuğu anlaşıldı.

Elektrokimyasal performans test sürecinde 0,1 C'de yapılan kapasite testlerinde ilk deşarj kapasiteleri malzeme içindeki nikel oranı arttıkça arttı. 20 çevrim sonunda kapasite korunumu yapıdaki nikel oranı arttıkça azaldı. Niobiyum katkılı malzemelerin ilk deşarj kapasitelerinin katkısız olanlardan daha düşük olduğu fakat 20 çevrim sonunda kapasite korunumlarının katkısızlardan fazla olduğu görüldü. 0,3 C'de yapılan testlerde niobyum katkılı ve katkısız malzemeler 0,1 C'de yapılan testler ile benzerlik gösterdi. 1 C'de yapılan kapasite testlerinde ise katkısız malzemelerin kapasite korunumları ile niobyum katkılı malzemelerin kapasite korunumları arasında bir fark görülmedi. Bununla birlikte 1 C'de yapılan çevrim testlerinde yapıdaki nikel oranı arttıkça malzemeler daha yüksek kapasite korunumu gösterdi.

Anahtar Kelimeler: Lityum-İyon Pil, Nikelce Zengin NMC, Niyobyum Katkılı, Sol-Jel Metodu, Katot Aktif Malzeme

To my dear wife Gamze

and my family

ACKNOWLEDGEMENTS

I wish to express my deepest gratitude to my supervisor Prof. Dr. M. Kadri Aydınol for his guidance and support during the study of this thesis. Working under his supervision has been a great pleasure for me.

I also want to thank Dr. Cansu Savaş Uygur who was like a teacher to me during my research and experiments. Her knowledge and experience greatly helped me.

I would like to thank Doruk Bahtiyar for his good friendship. Our brainstorming has been very helpful. And I would like to thank Dr. Şerif Kaya, Kadir Özgün Köse Nevzat Karaduman, Bayram Yıldız, and Zahid Sarıgöl for their friendship.

Besides, I would like to thank my family for their support, and encouragement in my life.

Finally, I am grateful to my dear wife Gamze Yıldırım for the encouragement and the endless support she gave me during this study.

TABLE OF CONTENTS

ABSTRACT v

ÖZ vii

ACKNOWLEDGEMENTS x

TABLE OF CONTENTS xi

LIST OF TABLES xiii

LIST OF FIGURES xv

CHAPTERS

1 INTRODUCTION 1

1.1 Li-Ion Batteries 1

1.2 Motivation and Aim 2

2 LITERATURE REVIEW 5

2.1 Li-Ion Cathode Materials 5

2.2 Nickel Rich NMC Cathode Materials 13

2.3 Cathode Active Material Synthesis Methods 25

2.4 The Effect of Doping on NMC 28

2.5 Nb Doping to NMC 33

3 EXPERIMENTAL PROCEDURE 35

3.1 Sol-Gel Synthesis 35

3.2 Niobium Doping to NMC 38

3.3 Characterization of The Samples 40

3.4 Cell Preparation and Electrochemical Tests 42

4 RESULTS AND DISCUSSION 45

4.1 Characterization of Powders 49
4.1.1 ICP Results of Powders 50
4.1.2 XRD Results of Powders 53
4.1.3 SEM Application of Powders 61
4.2 Electrochemical Tests 70
4.2.1 Capacity Test of Materials 70
4.2.2 Impedance Test of Samples 78
4.2.3 Rate Capability Test of Samples 81
5 CONCLUSION 89
REFERENCES 93

LIST OF TABLES

Table 2.1 Intensity ratios of $I_{(003)}/I_{(004)}$ of the $Li[Ni_xCo_yMn_z]O_2$ (x = 1/3, 0.5, 0.6, 0.7, 0.8 and 0.85)[33]..... 21
Table 3.1. The amounts of metal nitrate and corresponding citric acid required to produce 0.1 mol of $LiN_xM_yC_zO_2$ with sol-gel method. 36
Table 3.2. Mass values for Nb doping process. 39
Table 4.1. $I_{(003)}/I_{(104)}$ ratio of samples calcined at different temperatures. 46
Table 4.2 The lattice parameters of samples calcined at different temperatures. ... 47
Table 4.3. $I_{(003)}/I_{(104)}$ ratio of samples calcined at different times. 48
Table 4.4. The lattice parameters of samples calcined at different times. 49
Table 4.5 Calculated and obtained weights for sol-gel method. 50
Table 4.6. ICP results and corresponding mole ratios of pure NMC samples. 51
Table 4.7. ICP results and corresponding mole ratios of pre-pure NMC samples. 52
Table 4.8. ICP results and corresponding mole ratios of Nb containing NMC samples. 53
Table 4.9. The lattice parameters of pure samples. 55
Table 4.10. The lattice parameters of 2% Nb containing samples. 56
Table 4.11. Phase ratio according to Rietveld analysis. 57
Table 4.12. The lattice parameters of 4% Nb containing samples. 59
Table 4.13. Phase ratio according to Rietveld analysis. 59
Table 4.14. The lattice parameters of 8% Nb containing samples. 61
Table 4.15. Phase ratio according to Rietveld analysis. 61
Table 4.16. EDS results of pre - pure NMCs. 63
Table 4.17. EDS results of pure NMCs. 65
Table 4.18. EDS results of 2% Nb containing NMCs. 67
Table 4.19. EDS results of 8% Nb containing NMC 622 from different points..... 69
Table 4.20. First discharge, 20^{th} discharge and capacity retention at 0.1 C of pure samples. 72

Table 4.21. First discharge, 20th discharge and capacity retention at 0.1 C of 2% Nb containing samples. 76
Table 4.22. Resistance values of P622, P721, P712, and P811 samples i) before and ii) after 0.1 C at 20 cycle. 80
Table 4.23. Resistance values of D622, D721, D712, and D811 samples i) before and ii) after 0.1 C at 20 cycle. 81
Table 4.24. The discharge capacities of the P622, P721, P712, and P811 between 2.7 V - 4.2 V at 0.1 C, 0.3 C, 1 C, and 0.1 C. 84
Table 4.25. The discharge capacities of the D622, D721, D712, and D811 between 2.7 V - 4.2 V at 0.1 C, 0.3 C, 1 C, and 0.1 C. 87

LIST OF FIGURES

Figure 1.1. Working principle of Li-Ion battery[3]. 2
Figure 2.1.Graphical representation of lithium-insertion compound's layered, spinel, or olivine crystal structures[9]. 6
Figure 2.2. Lithium manganese oxide charge/discharge graph. 7
Figure 2.3. Layered structure of LCO. All layered cathode materials share a similar structure with only minor variations in lattice parameter lengths. They are reproduced from ref.[13], under the terms of the CC BY 3.0 license, https://creativecommons.org/ licenses/by/3.0/. 8
Figure 2.4. Phase diagram of the ternary system generated from $LiNiO_2$, $LiCoO_2$, and $LiMn_2O_4$ shows some representative compositions[27]. 11
Figure 2.5. The ex-situ EXAFS spectra at: (a) Mn K-edge, (b) Co K-edge and (c) Ni K-edge for $Li[Ni_{1/3}Co_{1/3}Mn_{1/3}]O_2$ charged up to 4.7 V (M: transition metal atom)[28]..... 12
Figure 2.6. The XRD results and 006/012, 018/110 peaks of NMC 622 samples produced by Niang et al., by co-precipitation method at different pH values[34]. 14
Figure 2.7. Evolution of the Ni and Co oxidation states in the bulk of the NMC532 electrode as a function of the charging voltage revealed by Ni-L_3 (a) and Co-L_3 (b) sXAS spectra collected in TFY mode. In (a) and (b), the calculated TFY sXAS spectra with the defined oxidation states in an octahedral crystal field are shown at the bottom, and the experimental spectra collected on NMC532 electrodes at different voltages are shown on top. The dashed line in (a) is the simulated spectrum which reveals the relative Ni^{2+}, Ni^{3+} and Ni^{4+} concentrations in the charged electrodes[38]. 15
Figure 2.8. Phase diagram of the ternary system generated from $LiNiO_2$, $LiCoO_2$, and $LiMn_2O_4$ shows Ni-rich NMC compositions. 17
Figure 2.9. Representation of the cation mixing[44]. 18

Figure 2.10. The energy vs. density of states showing the relative Fermi level of the Ni^{3+}/Ni^{4+} and Co^{3+}/Co^{4+} redox couples for $Li_xNi_yMn_yCo_{1-2y}O_2$ during the charge, for three states of charge determined by the Li concentration x; (a) x = 1; (b) x = 0.5; (c) x = 0 [50].....20
Figure 2.11. SEM images of as-prepared $Li[Ni_xCo_yMn_z]O_2$ powders: (a) x = 1/3, (b) x = 0.5, (c) x = 0.6, (d) x = 0.7, (e) x = 0.8 and (f) x = 0.85 where ' indicates the magnified images of the corresponding samples[33].....22
Figure 2.12. Variation of the chemical diffusion coefficient, $D\mathrm{Li}^+$, of $Li[Ni_xCo_yMn_z]O_2$ (x = 1/3, 0.5, 0.6, 0.7, and 0.8) as a function of the state of charge[33].....24
Figure 2.13. Schematic illustration of the synthesis procedure of Ni-rich NMC cathode materials with the co-precipitation method.....26
Figure 2.14. Schematic representation of the synthesis procedure of Ni-rich NMC cathode materials with the hydrothermal/solvothermal method[55].....27
Figure 2.15. Lattice parameter trends of different doped NMC-622 cathode materials in the fully lithiated (black squares) and the 60% delithiated (red squares) state (left). Illustration of the Li-interlayer movement along the c-axis due to doping effects (right)[58]. 30
Figure 3.1. Photographs of a) dissolved lithium, manganese, nickel, and cobalt nitrates in citric acid-water solution, b) mixing of all solutions with ethylene glycol and ammonium hydroxide, c) the gelation stage, and d) the gel after drying. 37
Figure 3.2. A chemical representation of Pechini modified sol-gel mechanism[69]. .38
Figure 3.3. Schematic representation of the experimental routes. 40
Figure 3.4. Schematic representation of Li-Gap in $LiTMO_2$ structure[72].....41
Figure 4.1. XRD patterns of temperature-dependent calcinations of pure NMC 622. 46
Figure 4.2. XRD patterns of time-dependent calcinations of pure NMC 622.....48
Figure 4.3. Pure nickel rich NMCs XRD graph. 54
Figure 4.4. 2% Nb contained nickel rich NMCs XRD graph.....56
Figure 4.5. 4% Nb containing nickel rich NMCs XRD graph. 58

Figure 4.6. 8% Nb containing nickel rich NMCs XRD graph. 60
Figure 4.7. SEM images of pre-pure a) $LiNi_{0.6}Mn_{0.2}Co_{0.2}O_2$, b) $LiNi_{0.7}Mn_{0.2}Co_{0.1}O_2$, c) $LiNi_{0.7}Mn_{0.1}Co_{0.2}O_2$, d) $LiNi_{0.8}Mn_{0.1}Co_{0.1}O_2$ ([i] 5000, [ii] 10000, and [iii] 20000 magnification for every type of powder). 62
Figure 4.8. SEM images of pure a) $LiNi_{0.6}Mn_{0.2}Co_{0.2}O_2$, b) $LiNi_{0.7}Mn_{0.2}Co_{0.1}O_2$, c).$LiNi_{0.7}Mn_{0.1}Co_{0.2}O_2$, d) $LiNi_{0.8}Mn_{0.1}Co_{0.1}O_2$ ([i] 5000, [ii] 10000, and [iii] 20000 magnification for every type of powder). 64
Figure 4.9. SEM images of 2% Nb containing a) $LiNi_{0.6}Mn_{0.2}Co_{0.2}O_2$, b).$LiNi_{0.7}Mn_{0.2}Co_{0.1}O_2$, c) $LiNi_{0.7}Mn_{0.1}Co_{0.2}O_2$, d) $LiNi_{0.8}Mn_{0.1}Co_{0.1}O_2$ ([i] 5000, [ii] 10000, and [iii] 20000 magnification for every type of powder). 66
Figure 4.10. SEM images of the NMC622 samples a) in the pure form b) with 2% Nb containing c) with 4% Nb containing and d) with 8% Nb containing ([i] 5000, [ii] 10000, and [iii] 20000 magnification for every type of powder). 68
Figure 4.11. SEM images of 8% Nb containing NMC 622 from different points. The circles represent the points where the EDS data was collected. 69
Figure 4.12. The initial discharge curves of P622, P721, P712, and P811 between 2.7 V - 4.2 V at 0.1 C. 70
Figure 4.13. The discharge capacities of the P622, P721, P712, and P811 between 2.7 V - 4.2 V at 0.1 C. 71
Figure 4.14. The discharge energies of the P622, P721, P712, and P811 between 2.7 V - 4.2 V at 0.1 C. 72
Figure 4.15. The initial discharge curves of D622, D721, D712, and D811 between 2.7 V - 4.2 V at 0.1 C. 73
Figure 4.16. The initial discharge voltage curves of a) P622 and D622, b) P721 and D721, c) P712 and D712, and d) P811 and D811 at 0.1C. 74
Figure 4.17. The discharge capacities of the D622, D721, D712, and D811 between 2.7 V - 4.2 V at 0.1 C. 75
Figure 4.18. The discharge capacities of a) P622 and D622, b) P721 and D721, c) P712 and D712, and d) P811 and D811 between 2.7 V – 4.2 V at 0.1 C. 77

Figure 4.19. The discharge energies of the D622, D721, D712, and D811 between 2.7 V - 4.2 V at 0.1 C. 77
Figure 4.20. The discharge energies of a) P622 and D622, b) P721 and D721, c) P712 and D712, and d) P811 and D811 between 2.7 V – 4.2 V at 0.1 C..... 78
Figure 4.21. Nyquist plots of P622, P721, P712, and P811 samples a) before and b) after 20 cycles at 0.1C. 79
Figure 4.22. Nyquist plots of D622, D721, D712, and D811 samples a) before and b) after 0.1 C at 20 cycle. 80
Figure 4.23. The initial discharge voltage curves of P622, P721, P712, and P811 at a) 0.3 C, and b) 1 C..... 82
Figure 4.24. The discharge capacity graph of the P622, P721, P712, and P811 between 2.7 V - 4.2 V at 0.1 C, 0.3 C, 1 C, and 0.1 C. 83
Figure 4.25. The discharge energy graph of the P622, P721, P712, and P811 between 2.7 V - 4.2 V at 0.1 C, 0.3 C, 1 C, and 0.1 C. 84
Figure 4.26. The initial discharge voltage curves of D622, D721, D712, and D811 at a) 0.3 C, and b) 1 C..... 85
Figure 4.27. The discharge capacity graph of the D622, D721, D712, and D811 between 2.7 V - 4.2 V at 0.1 C, 0.3 C, 1 C, and 0.1 C. 86
Figure 4.28. The discharge energy graph of the D622, D721, D712, and D811 between 2.7 V - 4.2 V at 0.1 C, 0.3 C, 1 C, and 0.1 C. 87

CHAPTER 1

INTRODUCTION

1.1 Li-Ion Batteries

In the world of energy storage technologies, batteries are unique because they create energy through chemical reactions and then store it in the same device. In 1912, G.N. Lewis started pioneering work on lithium batteries. However, the first non-rechargeable lithium batteries were not commercially available until the 1970s.

In the 1980s, efforts for producing rechargeable lithium batteries were unsuccessful because of issues with the metallic lithium used as anode material. Instead of metallic Li-ion, graphite was employed by the Sony brand. Accordingly, the first Li-Ion battery was launched in 1991. It continues to be the market's most promising and powerful battery[1].

Briefly explained, a Li-ion battery is a rechargeable battery where Li-ions move between the negative (i.e anode) and positive (i.e. cathode) electrodes in order to charge and discharge the battery. A lithium ion battery consists of the negative and positive electrodes, a separator between the anode and cathode, and an electrolyte taking up the remainder of the battery's volume and facilitating ion movement. In Figure 1.1, its working mechanism is explained in detail.

Among these four components, the most important part that determines the capacity and operating voltage of the lithium-ion battery is the anode and cathode materials. The cathodes are composed of compounds that contain lithium in which lithium should easily enter and leave the structure. The amount of lithium that leaves the structure and enters the structure without changing the structure determines the

capacity of Lithium-ion battery. The potential difference between the cathode and the anode determines the working voltage. Because anode materials have a more limited range of potentials, the cathode is the key component in determining the voltage of the battery[2]. Therefore, the compounds that host lithium are very important. While these compounds determine properties such as capacity, specific energy and working voltage, they also determine properties such as battery safety, battery cost, and cycle life. Today, the main cathode compounds used in both commercial and research fields are lithium iron phosphate (LFP), nickel manganese cobalt (NMC), nickel cobalt aluminum (NCA), lithium titanium oxide (LTO), lithium cobalt oxide (LCO), and lithium manganese oxide (LMO).

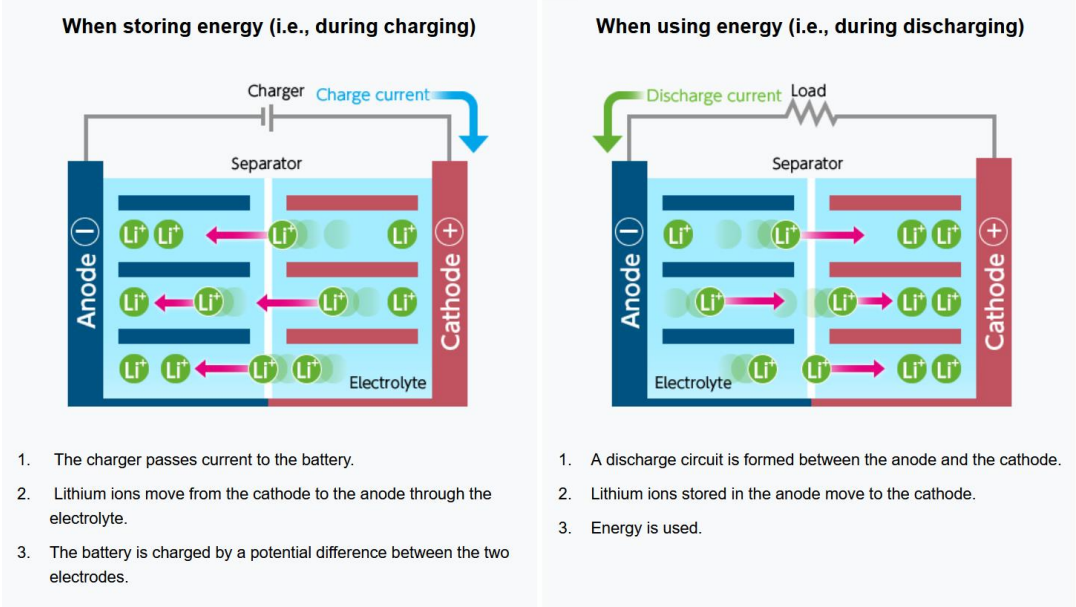


Figure 1.1. Working principle of Li-Ion battery[3].

1.2 Motivation and Aim

NMC is one of the most used cathode materials in commercial and research fields among other candidates in terms of its improved stability and electrochemical performance as well as environmental friendliness. The specific capacity of the

compound in NMC lithium ion battery cathode is very much dependent on the Ni content, which adversely affects the structural stability. This study aims to investigate the effect of Ni content in the samples on the structure of the NMC cathode active material and its electrochemical property accordingly.

Moreover, the effects of niobium element, which has been proven to increase the stability of the NMC cathode materials, on the structure of NMC cathode materials with different nickel ratios were investigated[4–6]. Nb-doped NMC materials with different nickel ratios were compared to each other in terms of their electrochemical properties and structures. Also, they were compared to their corresponding undoped-NMC materials with respect to their electrochemical properties and structures. All samples in the study were sythesized by citric acid assisted Pechini modified sol-gel method.

CHAPTER 2

LITERATURE REVIEW

2.1 Li-Ion Cathode Materials

In the 1970s, intercalation cathode materials appeared with host materials that undergo electrochemical ionic intercalation reactions[7]. As the successors have higher electrochemical potentials, these types of electrodes were overtaken by TM oxides (e.g. $LiCoO_2$ and $LiMn_2O_4$) and polyanion compounds (e.g. $LiFePO_4$). Nowadays, cathodes are oxide or phosphate-based materials are commonly utilized in lithium ion batteries (LIBs)[8].

Intercalation positive electrode active materials typically have layered, spinel, or olivine crystal structures[9,10]. The graphical representations of their structures are shown in Figure 2.1.

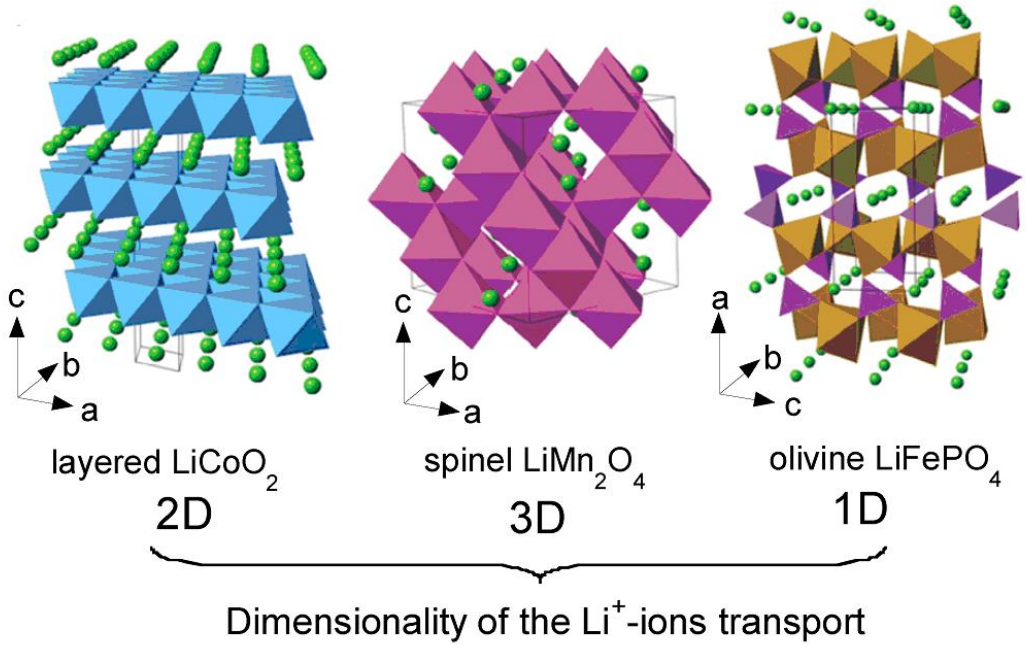


Figure 2.1.Graphical representation of lithium-insertion compound's layered, spinel, or olivine crystal structures[9].

The phospho-olivine $LiFePO_4$ (LFP) is a positive electrode material for lithium rechargeable cells, with a theoretical specific capacity of 160 mAh/g at medium current densities. Its outstanding features are being non-toxic and inexpensive. Yet, the LFP's poor electronic conductivity ($\sigma_e < 10^{-9}$ S cm^{-1}) and low Li^+ ion diffusion coefficient ($D \approx 10^{-14}$ cm^2 s^{-1}) might cause the capacity to decrease during high-rate discharge. To solve the low electronic conductivity issue, research into the carbon coated LFP started. This significantly improved electrical transmission among particles, which ensures high-rate capability while minimizing particle agglomeration[11]. Lithium extraction from LFP gives a 3.45 V redox potential with a change of Fe^{2+}/Fe^{3+} versus Li/Li^+.

Manganese, the other compound candidate, is abundant in nature and is inexpensive compared to other metals. The spinel $LiMn_2O_4$ has an octahedral lattice and is structurally stable during the charge-discharge process. However, $LiMn_2O_4$ has several disadvantages, such as a poor discharge capacity and significant capacity

fading during cycling. The other problem is not being able to use standard electrolytes as they operate at high voltages. $LiMn_2O_4$ is demonstrated to work at high cutoff voltages in Figure 2.2. (3 - 4.85 V). Future studies in the field of conductivity and electrolytes may pave the way for inexpensive and stable manganese compounds[9].

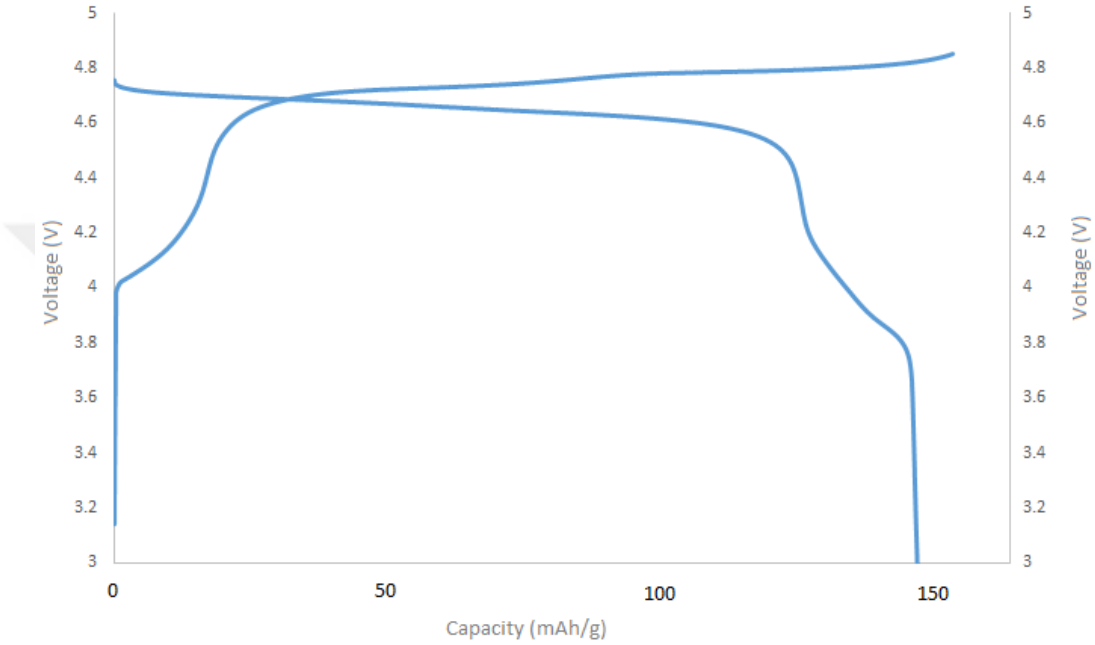


Figure 2.2. Lithium manganese oxide charge/discharge graph.

$LiCoO_2$ (LCO) has the α-$NaFeO_2$ structure where the oxygen ions are close-packed in a cubic arrangement, and the cobalt and lithium ions occupy the octahedral sites of alternating layers. LCO is a fundamental structure of lithium layered oxide structures-oriented Li-O-TM-O-(Li-O-…). Its structure is shown in Figure 2.3. By using X-Ray Diffraction (XRD) analysis, the material's crystal structure can be determined. With this way, the lattice parameters a and c of the material's crystal structure can be obtained. Studies show that one of the most important characteristics indicating that the produced material has a layered structure was that the c/a ratio was higher than 4.9[12].

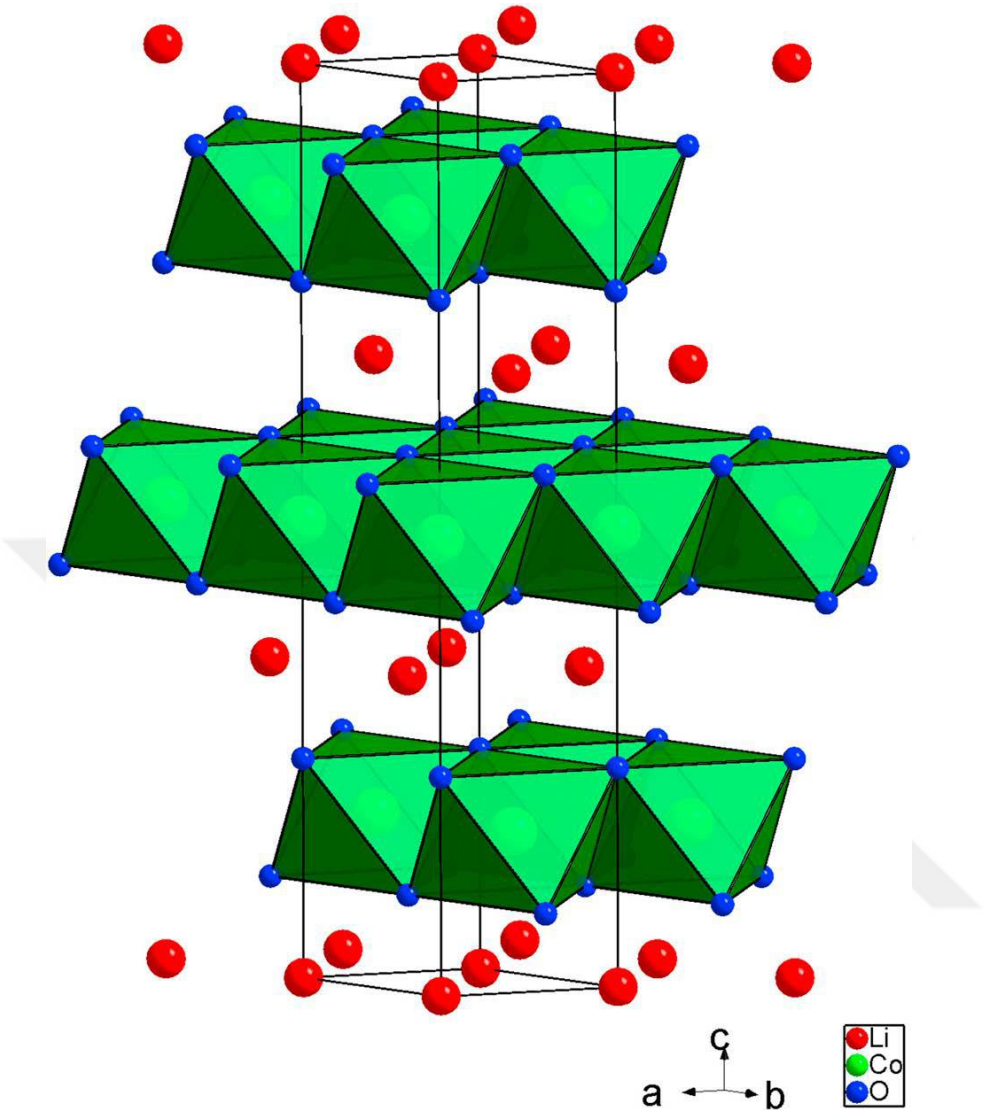


Figure 2.3. Layered structure of LCO. All layered cathode materials share a similar structure with only minor variations in lattice parameter lengths. They are reproduced from ref.[13], under the terms of the CC BY 3.0 license, https://creativecommons.org/ licenses/by/3.0/.

The $LiCoO_2$ structure allows for high Li-Ion charge and discharge rates. Additionally, thanks to its structure, there are minimal volume changes when Li-Ions are intercalated or de-intercalated. $LiCoO_2$ was employed in the first commercial lithium-ion batteries due to its ease to synthesize, good cyclability, and high capacity. It is still commonly used in today's modern lithium ion batteries[14]. The theoretical

capacity of $LiCoO_2$ is 247 mAh/g. However, only half of the Li-ions can be de-intercalated safely without severe structural damage and oxygen release[15,16]. Although cobalt is the best choice for lithium ion batteries, researchers have been studying to find its alternative because of its high cost and environmentally dangerous nature.

Nickel-Containing $LiNiO_2$ (LNO) is isostructural with $LiCoO_2$ and has a layered oxide structure. Nickel is cheaper and safer to use when compared to cobalt. Additionally, LNO also has the same advantages as LCO, such as high capacity and ease of production. It is a good sample for Li-Ion batteries because of these factors. However, it has been noticed that LNO has a few drawbacks. Firstly, irreversible phase transitions occur during the charge-discharge process. The radius of lithium Li^+ (0.076 nm) and nickel Ni^{2+} (0.069 nm) ions are similar[17]. Therefore, nickel ions occupy the lithium sites while charging discharging. This causes the capacity to fade in later cycles. This phenomenon is called cation mixing. The second drawback of the LNO is the exothermic release of oxygen (O_2) at high temperatures and security concerns in the charged state[18]. Therefore, it was concluded that $LiNiO_2$ was not a proper ingredient for industrial Li-ion batteries.

To overcome the main disadvantages exhibited by both $LiCoO_2$ and $LiNiO_2$ oxides, the $LiNi_{1-y}Co_yO_2$ has been studied. The results of the electrochemical charge-discharge studies have shown that the various compositions of $LiNi_{1-y}Co_yO_2$ with better capacity and reversibility were obtained. However, the desired product with low cost and high capacity retention to be used in the industry could not be synthesized[19]. Therefore, the researchers have shifted their directions toward $LiNi_{1-y}Co_yO_2$ alloys with manganese and aluminum elements.

By doping aluminum to $LiNi_{1-y}Co_yO_2$, the $LiNi_xCo_yAl_{1-x-y}O_2$ (NCA) material was obtained. Therefore, its structure was stabilized, and its thermal stability was increased[20,21]. $LiNi_{0.8}Co_{0.15}Al_{0.05}O_2$ has been the subject of most research among NCA materials with various ratios of the elements Ni, Co, and Al. This is probably because of its low cost, low toxicity, and high energy density[22]. Tesla is the first

company to utilize NCA cathode materials in electric vehicles[23]. In summary, NCA's large capacity and superior structural stability make it a potential cathode material. The cycle and rate performance of NCA materials, however, continue to restrict their wide-scale adoption[24].

Besides these, the layered $LiNi_xMn_yCo_{1-x-y}O_2$ (NMC) materials with a hexagonal single-phase structure have drawn lots of interest as electrode materials to replace $LiNi_{1-y}Co_yO_2$ in lithium ion batteries. This results from their greater capacity, thermal stability in the charged state, and developed cycling stability even at elevated temperatures. Although the addition of manganese to $LiNi_{1-y}Co_yO_2$ provides electrochemical stability, it decreases the electronic conductivity.

NMC's theoretical capacity changes between 160 and 200 mAh/g according to the elemental ratio of nickel, manganese, and cobalt. As seen in Figure 2.4, there are different compositions of the NMC being worked on[25–27].

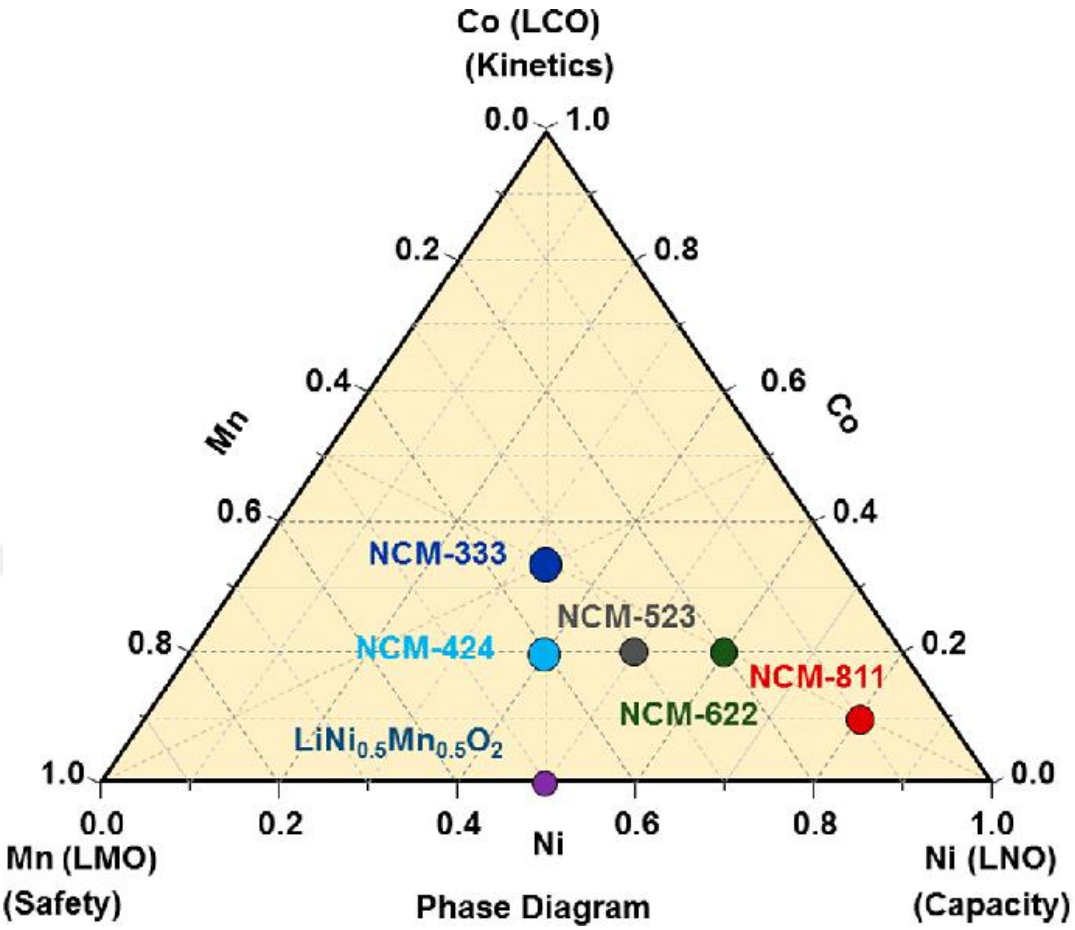


Figure 2.4. Phase diagram of the ternary system generated from $LiNiO_2$, $LiCoO_2$, and $LiMn_2O_4$ shows some representative compositions[27].

In the study of Kim and Chung[28], the experiment was used to observe the change in the valence states of nickel, manganese, and cobalt in NMC 111 according to the voltages (between 2 V and 4.7 V). During charging, the ex-situ EXAFS spectrum was obtained at OCV, 3.9, 4.1, 4.3, 4.5, and 4.7 voltages.

According to the extended X-ray absorption fine structure (EXAFS) data, the researchers received information regarding the inter-atomic distance of Ni-O, Mn-O, and Co-O. As shown in Figure 2.5-a, there is no change in the Mn-O bond length during charging. This means the valence state of Mn does not vary. On the other hand, the inter-atomic distance of Co-O decreases at a slow rate until 4.7 V as indicated in Figure 2.5-b. When looking at the third element, the bond length of Ni-

O reduces up to 4.1 V. After 4.1 Volts, its valence state stays constant, as shown in Figure 2.5-c. According to the results of the study, the oxidation reaction of Ni^{2+}/Ni^{3+}, Ni^{3+}/Ni^{4+}, and Co^{3+}/Co^{4+} occurred during the charge of the NMC 111. In conclusion, Ni^{2+} and Co^{3+} ions directly affect the electrochemical capacity of the material (NMC)[28].

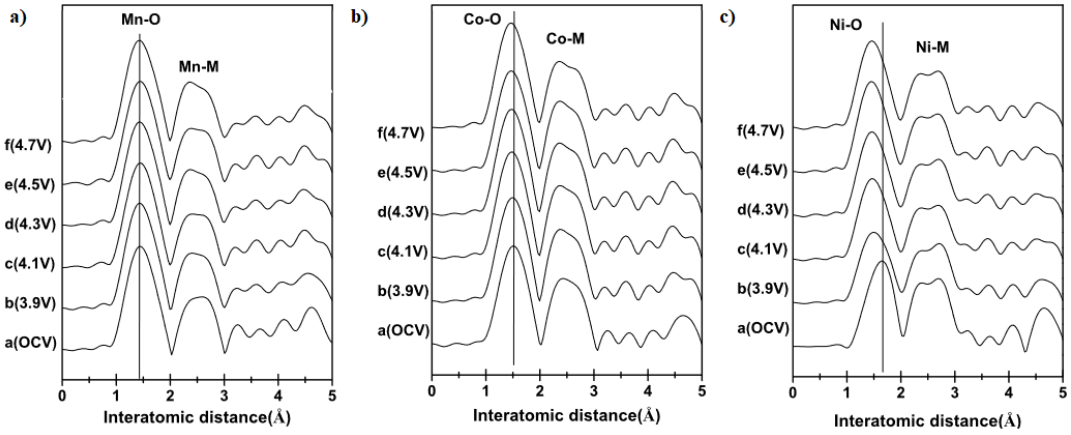


Figure 2.5. The ex-situ EXAFS spectra at: (a) Mn K-edge, (b) Co K-edge and (c) Ni K-edge for $Li[Ni_{1/3}Co_{1/3}Mn_{1/3}]O_2$ charged up to 4.7 V (M: transition metal atom)[28].

To examine the effect of cobalt, NMC 422 and NMC 333 were produced by Li et al[29]. The lattice parameters (a and c) of NMC 422 and NMC 333 were 2.87 Å and 14.27 Å and 2.86 Å and 14.24 Å, respectively. It was observed that the increasing cobalt content caused to decrease in the lattice parameters (from 2.87 Å to 2.86 Å and from 14.27 Å to 14.24 Å). When looking at the EXAFS measurements, it was seen that the Co-M bond distance (2.80 Å) was shorter than the Mn-M bond distance (2.85 Å), resulting in the decrease in a and c. In another word, the lattice parameters got shorter with increasing Co content because the Co-M bond distance was shorter than the Mn-M bond distance[29,30].

2.2 Nickel Rich NMC Cathode Materials

Generally, some varieties in the chemical valence and electronic structure of the TM elements occur after the insertion and extraction of lithium. Both structural instabilities in the electrode and side reactions at the electrode-electrolyte interface might result from this mechanism. Electronic and crystal structures are essential for the electrochemical performance of the material. Several electrochemical data regarding diverse NMC materials with distinct stoichiometric ratios of Ni, Mn, and Co elements support that nickel makes a contribution to the high capacity at the expense of security features; cobalt increases rate performance at the expense of cost, and manganese increases structural stability at the expense of capacity.

Lithium layer on the 3a site, transition metals (NMC) layer on the 3b site, and oxygen layer on the 6c site make up the R-3m structure (rhombohedral symmetry) of NMC oxide[31–33] and can be seen in the splitting of the (018) and (110) peaks as well as the (006) and (012) peaks. NMC 622 samples produced by Niang et al.[34], by co-precipitation method at different pH values are given in Figure 2.6. The clear separation of the 006/012 and 108/110 peaks indicated that the materials had a well-layered structure. For instance, in situ XRD measurements in the cell voltage windows of 3.0 - 4.0 V and 4.0 - 4.4 V can be used to observe the expansion and contraction of the c-axis (14.21 Å) of NMC811 lattices, where (003) peaks can reduce from 18.96° (3.0 V) and then increase to 19.09° (4.4 V)[35].

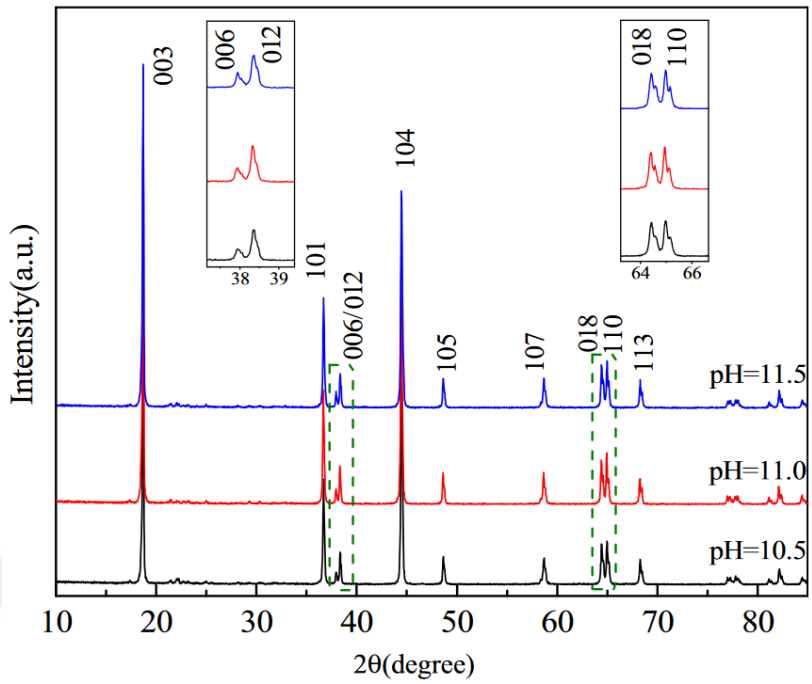


Figure 2.6. The XRD results and 006/012, 018/110 peaks of NMC 622 samples produced by Niang et al., by co-precipitation method at different pH values[34].

The valence of transition metals increases due to self-redox reaction at highly delithiated states, and as a result of the low-spin $Co^{3+/4+}$:t_{2g} band's overlap with the 2p band of O_2^{2-} oxidized transition metal ions can be reduced by electron transfer from O_2^{2-} to $Co^{3+/4+}$ so that O_2 is released into the battery cells[35]. As a result, transition metals that have been oxidized to 4+ are reduced by O_2 during the first charging period, causing oxygen release. O_2 release from nickel rich NMC-based cathode materials is dominated by similar effects on Ni^{4+} [36,37].

This is because large amounts of Ni^{4+} on cathode surface regions can lead to side reactions and Ni^{2+} may result in cation mixing.

The entrance to the Ni-rich NMC studies began with the synthesis of $LiNi_{0.5}Mn_{0.3}Co_{0.2}O_2$ (NMC532). Ruimin Qiao and Jun Liu studied the related material up to 4.5 cut-off voltages. Theoretically, it was expected to obtain NMC532 with 60% Ni^{2+}, 40% Ni^{3+}, and 0% Ni^{4+} stoichiometrically, because the oxidation states of manganese and cobalt are 4+ and 3+, respectively. However, according to

the calculated TFY (total fluorescence yield) sXAS spectra with the identified oxidation states, the percentages of Ni^{2+}, Ni^{3+}, and Ni^{4+} were 63%, 17%, and 20%.

After charging up to 4.5 V, the identified oxidation states of Ni^{2+}, Ni^{3+}, and Ni^{4+} were 12%, 1%, and 87% as calculated from the sXAS spectra. When it is compared to the pristine electrode in Figure 2.7, the Ni^{2+} and Ni^{3+} are mostly oxidized to Ni^{4+} when charging the NMC532 to 4.2 V. Although the Ni^{3+} amount left on the charged sample is insignificant/negligible, the 12% of Ni^{2+} is still in the charged electrode as it is electrochemically inactive.

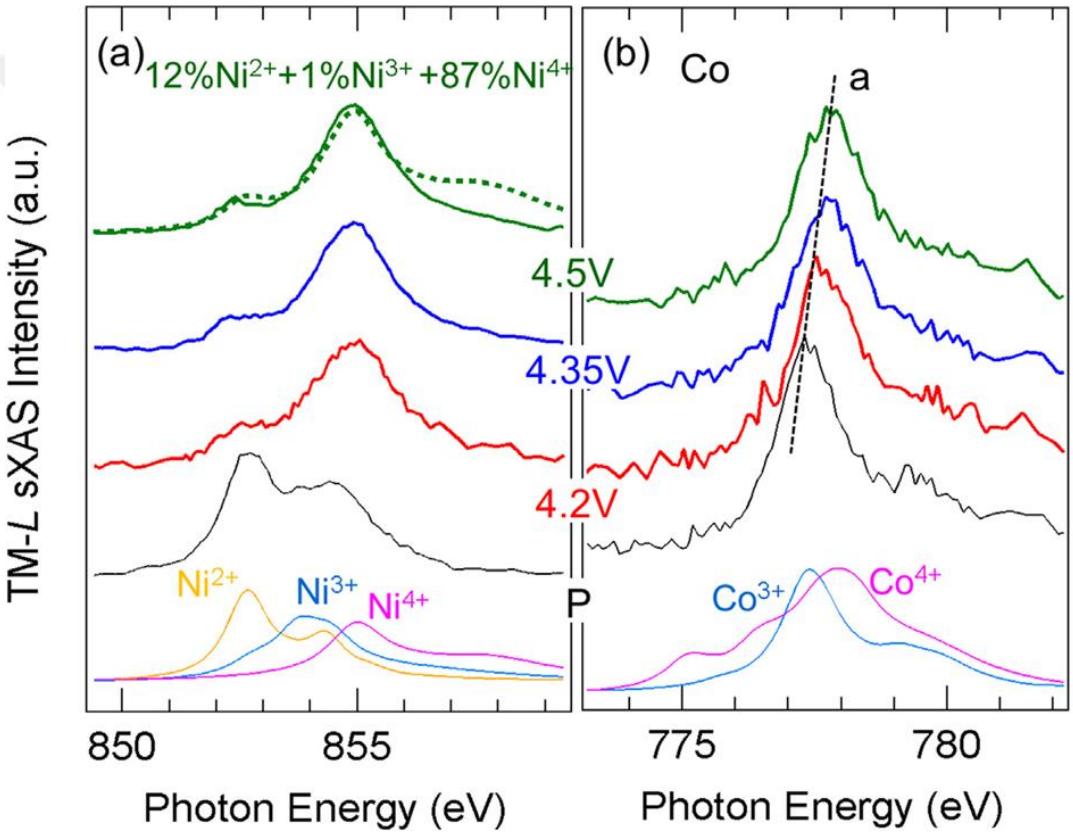


Figure 2.7. Evolution of the Ni and Co oxidation states in the bulk of the NMC532 electrode as a function of the charging voltage revealed by Ni-L_3 (a) and Co-L_3 (b) sXAS spectra collected in TFY mode. In (a) and (b), the calculated TFY sXAS spectra with the defined oxidation states in an octahedral crystal field are shown at the bottom, and the experimental spectra collected on NMC532 electrodes at different voltages are shown on top. The dashed line in (a) is the simulated spectrum

which reveals the relative Ni^{2+}, Ni^{3+} and Ni^{4+} concentrations in the charged electrodes[38].

At the same time, the Co demonstrates intermediate valence states throughout the charging. Therefore, the cobalt supports an itinerant electron system in NMC532. This is quite important because it improves the rate capability of NMC via the Co doping. Moreover, Mn^{4+} is not oxidized or reduced during the charging process[38].

Hajime Arai reported that the $LiNiO_2$ reversible capacity of the battery reaches 220 mAh/g in the voltage range of 3.0-4.5V. But a low cycle efficiency of approximately 80% is observed in the first charge-discharge cycle[39]. The radius values of lithium Li^+ (0.076 nm) and nickel Ni^{+2} (0.069 nm) ions are similar. Therefore, during the charge-discharge cycle, nickel ions occupy the lithium sites. This causes capacity loss. This phenomenon is called cation mixing[17,40–43].

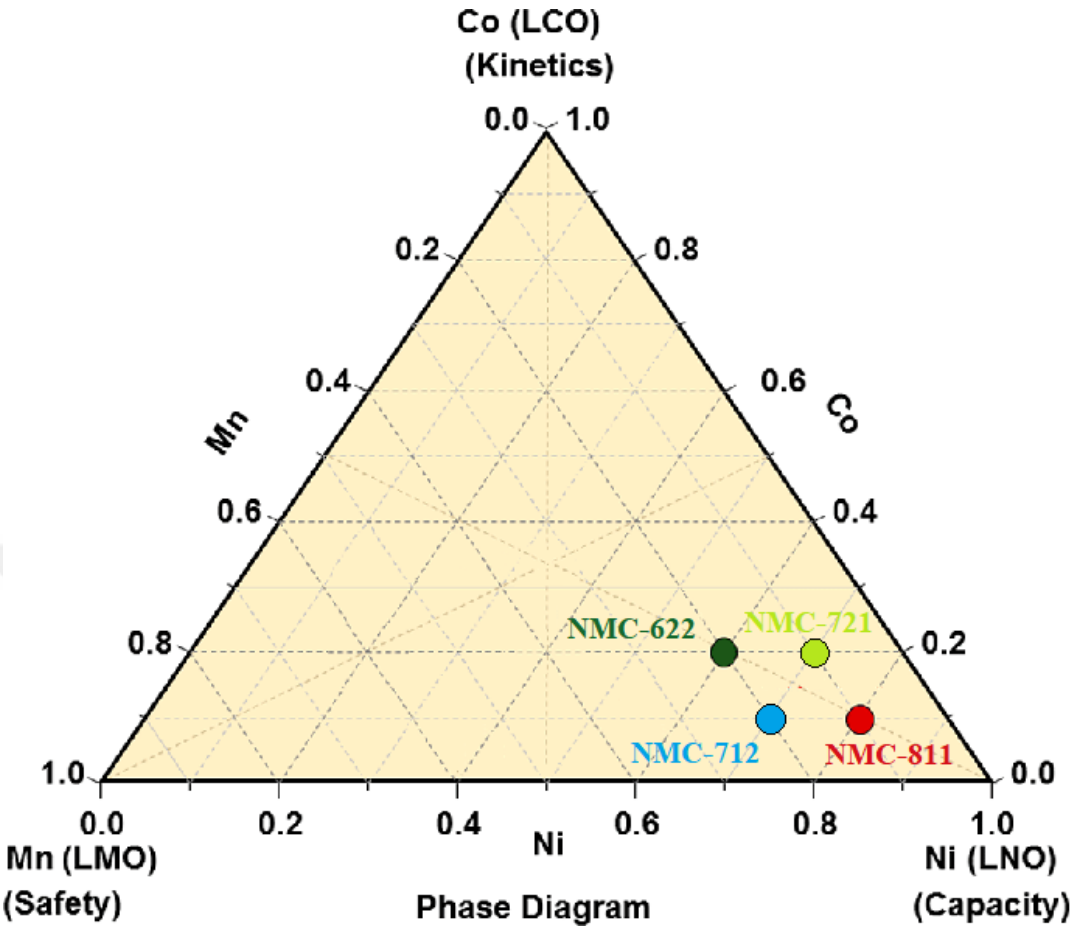


Figure 2.8. Phase diagram of the ternary system generated from $LiNiO_2$, $LiCoO_2$, and $LiMn_2O_4$ shows Ni-rich NMC compositions.

In Figure 2.9, the cation mixing phenomenon is represented in detail. The requested structure of the $LiNMCO_2$ is indicated in Figure 2.9-a. At the delithiated (charged) state, its structure is like in Figure 2.9-c, where lithium ions move to the anode. As mentioned above, nickel ions occupy the lithium sites during the discharge cycle. This is also schematically represented in Figure 2.9-d.

Moreover, the corresponding intensity values to (104) and (003) planes in Figure 2.9-d can be collected from XRD graphs. The calculated intensity ratio (i.e., $I_{(003)}/I_{(104)}$) can be employed as a parameter to review the effect of cation mixing on the structure. If the intensity ratio is higher than 1.2, the effect of cation mixing will be lower.

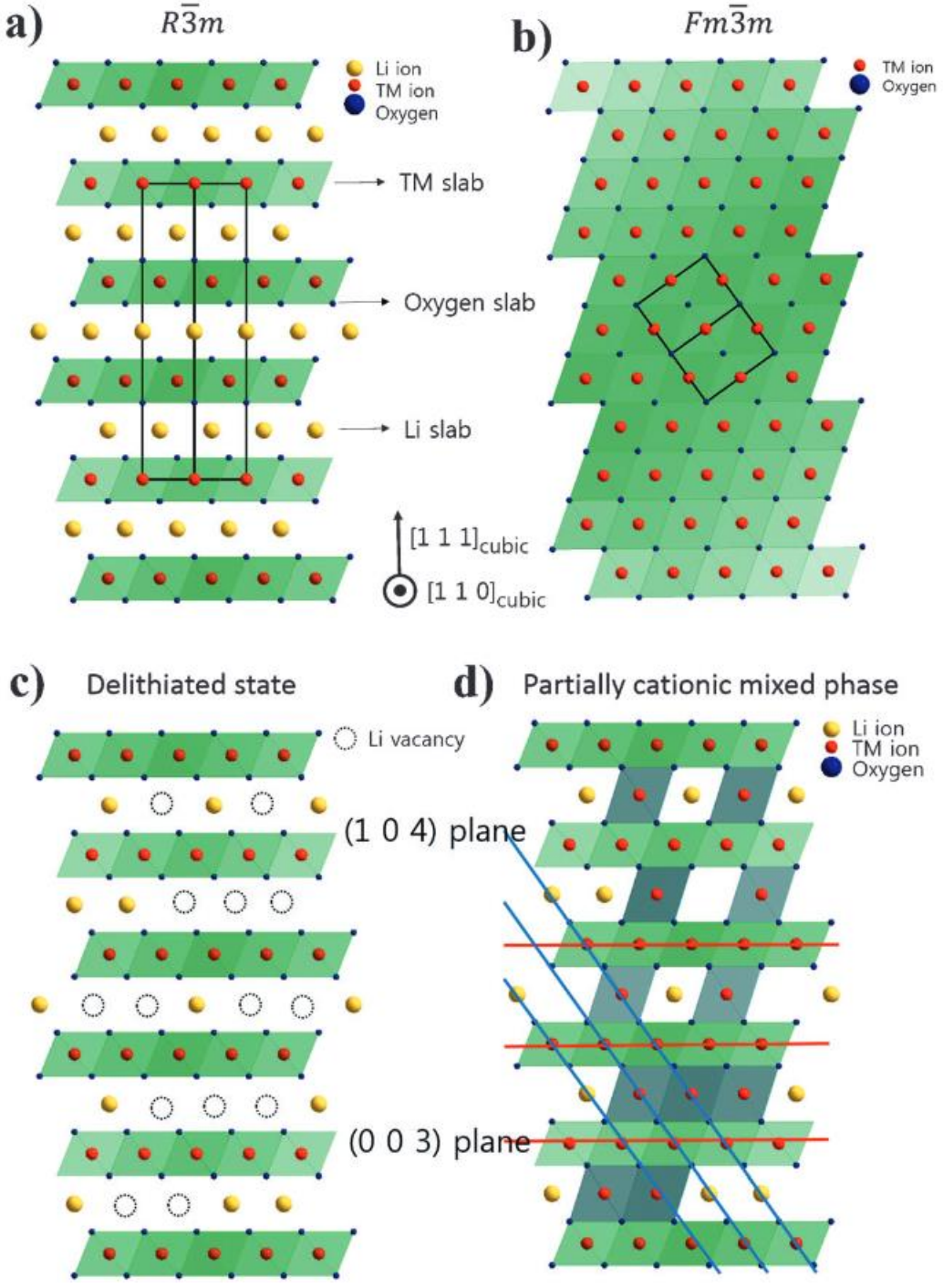


Figure 2.9. Representation of the cation mixing[44].

How $Li(Ni_{1-x-y}Mn_xCo_y)$ emerged is explained in part 2.1. Therefore, it is not mentioned again in this section. Liu et al. noticed the first layered $Li(Ni_{1-x-y}Mn_xCo_y)O_2$ cathode material in 1999. According to their studies, its layered

structure could be stabilized by substituting nickel partially with cobalt and manganese, and hence its stoichiometry could be protected. Additionally, the cation mixing between transition metal and lithium ions could be prevented[45].

The nickel content in NMC leads to significant changes in the resulting electrode properties. Although the specific capacity of nickel rich NMC batteries improves with the increase in the nickel content, their thermal and structural stabilities decrease[46]. At this point, the study of Johannes Kasnatscheew was examined in order to support this idea. According to his study, the lithium extraction from the cathode while discharging was reported to be 61%, 62%, 70%, and 81% in the NMC111, NMC532, NMC622, and NMC811, respectively. The results demonstrated there is a direct relationship between the Li^+ extraction ratio and the nickel ratio[47].

The effect of Ni, Mn, and Co ratios on Ni-rich NMC batteries is indicated in Figure 2.8. Even though the capacity of Ni-rich NMC batteries increases with the decrease in manganese content, their safety diminishes. With the addition of manganese, the production cost of Ni-rich NMC batteries decreases, and their safety thrives because it strengthens the structure. On the other hand, their capacity decreases because manganese does not contribute to the discharge capacity in a layered structure, and it remains fully oxidized as Mn^{4+}. Battery cost is also reduced by decreasing the cobalt content. However, it also leads to a decrease in its stability. This can be compensated for by preventing nickel atoms from interacting with lithium cites[48,49]. All of the identified nickel Rich NCM cathode materials share a layered structure with $LiCoO_2$ and $LiNiO_2$ called α-$NaFeO_2$.

According to the Rigid-Band Model, the relative positions of the Fermi level and the O:2p band regarding the Ni^{3+}/Ni^{4+} and Co^{3+}/Co^{4+} redox couples for NMC as a function of x(Li) are shown in Figure 2.10. During delithiation, the stability of $Li(Ni_{(1-x-y)}Mn_xCo_y)O_2$ electrodes are higher than $LiCoO_2$ electrodes between 2.8 and 4.6 V potential regions[9,50].

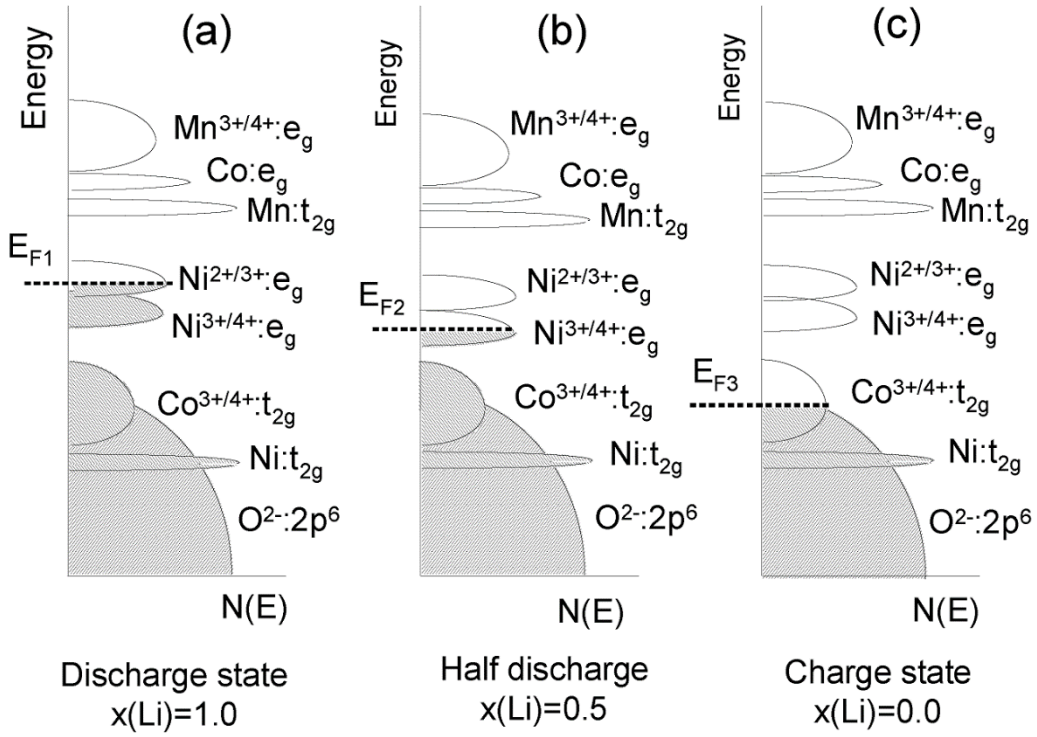


Figure 2.10. The energy vs. density of states showing the relative Fermi level of the Ni^{3+}/Ni^{4+} and Co^{3+}/Co^{4+} redox couples for $Li_xNi_yMn_yCo_{1-2y}O_2$ during the charge, for three states of charge determined by the Li concentration x; (a) x = 1; (b) x = 0.5; (c) x = 0 [50].

In the study of Noh et al.[33], the Ni^{2+} ions in the lithium layer decrease both the discharge capacity of NMC materials and the ionic diffusivity of Li^+. These are the major reasons why the electrochemical performance is weak.

In Table 2.1, the intensity ratios (i.e., $I_{(003)}/I_{(104)}$) are 1.35 and 1.18 for x = 0.33 and 0.85, respectively. There is a decrease because the increase in Ni content leads to cation mixing.

Table 2.1 Intensity ratios of $I_{(003)}/I_{(004)}$ of the $Li[Ni_xCo_yMn_z]O_2$ (x = 1/3, 0.5, 0.6, 0.7, 0.8 and 0.85)[33].

Compositions	**$I_{(003)}/I_{(104)}$**
$Li[Ni_{1/3}Co_{1/3}Mn_{1/3}]O_2$	1.35
$Li[Ni_{0.5}Co_{0.2}Mn_{0.3}]O_2$	1.32
$Li[Ni_{0.6}Co_{0.2}Mn_{0.2}]O_2$	1.26
$Li[Ni_{0.7}Co_{0.15}Mn_{0.15}]O_2$	1.20
$Li[Ni_{0.8}Co_{0.1}Mn_{0.1}]O_2$	1.19
$Li[Ni_{0.85}Co_{0.075}Mn_{0.075}]O_2$	1.18

In Figure 2.11, the secondary and primary particles of all samples are indicated. As seen from the figure, all the secondary particles have a spherical shape, and their diameters are 10 μm on average. However, the primary particles differ in size because their diameters are different from each other. The poor cycle life of NMC consisting of small-sized primary particles may be due to its large surface area in contact with electrolytes.

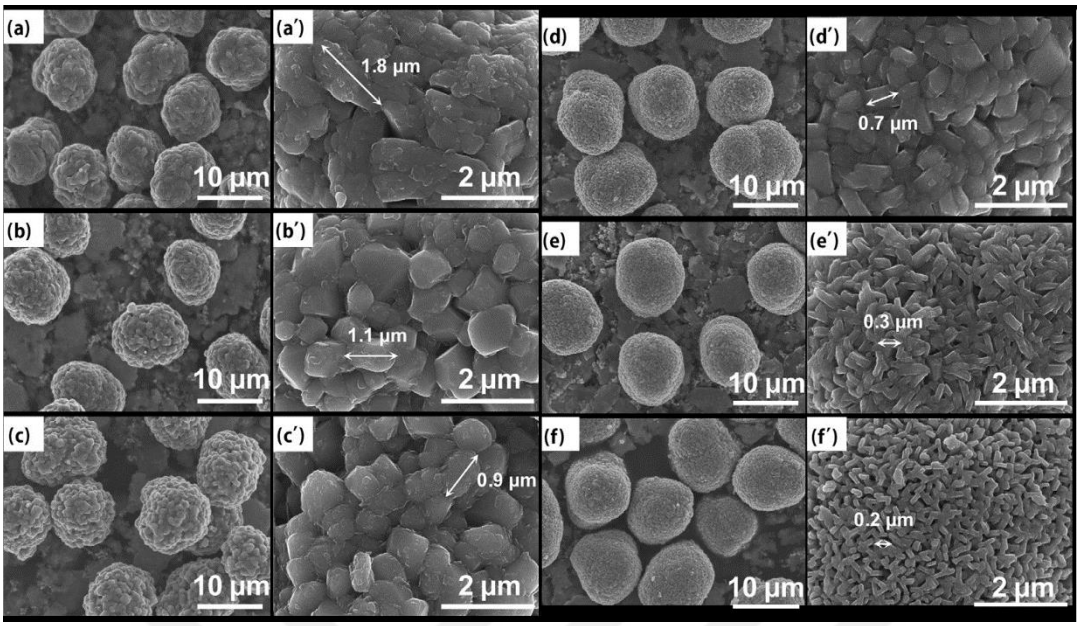


Figure 2.11. SEM images of as-prepared $Li[Ni_xCo_yMn_z]O_2$ powders: (a) x = 1/3, (b) x = 0.5, (c) x = 0.6, (d) x = 0.7, (e) x = 0.8 and (f) x = 0.85 where ’ indicates the magnified images of the corresponding samples[33].

Charge-discharge tests from 3.0 and 4.3 V with 0.1 C-rate show that $Li[Ni_xCo_yMn_z]O_2$ electrodes' initial discharge capacity increases as the Ni content (x) increases. The $Li/Li[Ni_xCo_yMn_z]O_2$ (x = 1/3) cell displayed redox peaks at approximately 3.76 V while charging and 3.72 V during discharging during the first cycle. With increasing Ni content, a recent oxidation peak at 3.64 Volts appeared. The redox peaks for the $Li/Li[Ni_xCo_yMn_z]O_2$ (where x = 1/3) cell seem to be remarkably stable throughout the cycling process. However, as the Ni content (x) rose, the redox peaks shifted apart and became more polarized. In particular, after 100 cycles, the oxidation peak for the $Li/Li[Ni_xCo_yMn_z]O_2$ (x = 0.8) cell got smaller and shifted to 3.76 Volts.

According to reports, $Li[Ni_xCo_yMn_z]O_2$'s capacity fading is mostly affected by the rapid shrinkage of volume that occurs during the structural change from H2 to H3[51]. The $Li[Ni_xCo_yMn_z]O_2$ electrode shows good reversibility since there is no H2-H3 phase transition as the nickel content decreases. This is reflected in the stability of

the host structure, which is well matched with smaller volume change after cycling. This means that the good cycling performance of the Ni-deficient $Li[Ni_xCo_yMn_z]O_2$ electrode is thought to be primarily caused by the suppression of the H2 + H3 transition. The reduction in the discharge voltage with cycling indicated by the arrow demonstrates a rise in the internal resistance (IR). The magnitude of the decrease in IR rose with the increase in the nickel content.

Another experiment was conducted to understand the behavior of Ni-rich NMCs at high temperatures. The reduction in the thermal stability of NMC is expected with rising Ni content. To prove this statement, a study was conducted on NMC materials with different stoichiometric ratios between the Ni, Mn, and Co atoms at 55 C for 100 cycles. According to the results of the study, NMC 111 had capacity retention of higher than 92.4%. This was 90.0%, 85.1%, 78.5% and 70.2% for NMC 523, 622, 712, and 811, respectively[33].

The rate capability of the battery is how much of the given capacity is recovered during rapid charge-discharge of the battery. Even if the material is charged slowly, the calculated discharge capacity may not be obtained due to rapid discharge. It is considered that at different compositions, the electronic conductivity of NMC and the chemical diffusivity of lithium ion change and thus affect the high-rate capability of NMC. In discharge tests for NMC 111 and NMC 811, at 5 C, the discharge capacity of NMC 111 reached 75% of its capacity at 0.2 C, while at 5 C, NMC811 achieved 90% of its capacity at 0.2 C. Figure 2.12 demonstrates the correlation between the Li^+ diffusivity and Ni content (x). According to the figure, the diffusivity increases from 10^{-11} to 10^{-8} cm^2 S^{-1} with the increase in the Ni content from 0.3 to 0.8 moles in NMC.

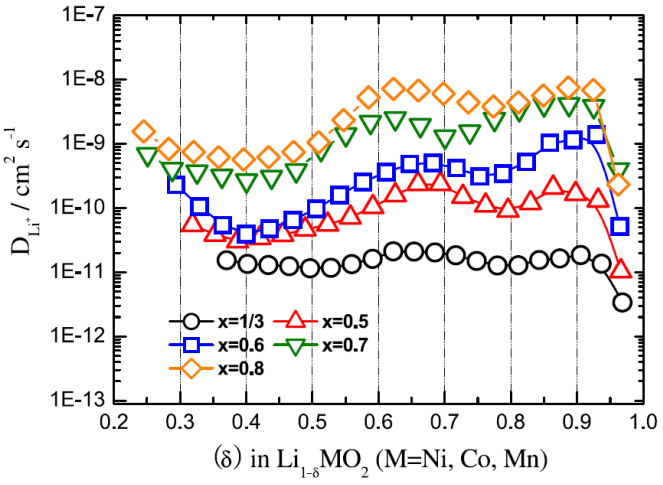


Figure 2.12. Variation of the chemical diffusion coefficient, *D*Li^+, of $Li[Ni_xCo_yMn_z]O_2$ (x = 1/3, 0.5, 0.6, 0.7, and 0.8) as a function of the state of charge[33].

The electronic conductivity is also pertaining to the nickel content in NMC materials. The increase in the Ni content leads to increasing Ni^{3+} and hence an increase in the electronic conductivity caused by the Ni^{2+}/Ni^{3+} mixed valence effect.

In the study of Sun et al.[52], the improvement in the thermal stability of NMC materials was related to the rise in the stable Mn^{4+} ions and the decrease in the Ni^{4+}, causing the suppression of the increased charge transfer resistance.

In the study Noh et al.[33], the oxygen release measurement from chemically delithiated $Li[Ni_xCo_yMn_z]O_2$ using the thermal gravimetric analysis (TGA) was made for evaluating the differences in the safety characteristics of the NMC materials with distinct stoichiometric ratios between the Ni, Mn, and Co elements (NMC111, NMC532, NMC622, NMC721, and NMC811). Additionally, the increase in the oxygen release from 18.4% for NMC111 to 51.7% for NMC811 was observed as a result of the increase in the nickel content. On the other hand, the stability of NMC materials was reduced due to the transformation of unstable and reactive Ni^{4+} ions to more stable Ni^{2+} as well as the O_2 release. According to the results, even though NMC111 had the best capacity retention and thermal stability, the discharge capacity

of the related material was limited because of its low Ni content. Conversely, NMC811 experienced severe capacity reduction due to its high Ni content.

2.3 Cathode Active Material Synthesis Methods

A Ball-Milling Assisted Solid-State was employed by Jotti Karunawan to synthesize NMC materials. Based on their study, they reported it as promising due to its simple procedure, as the required parameters are only mixing rpm and mixing time. In the study, lithium acetate dihydrate, nickel acetate tetrahydrate, cobalt acetate tetrahydrate, and manganese acetate tetrahydrate were employed as precursors. All of them were mixed (around 30 minutes) in a 100 ml ethanol solution until a homogeneous solution was obtained. Afterward, the resulting sample/solution was dried in an oven at 120 degrees Celsius overnight. The following step was to mix it in a planetary ball mill at 1200 rpm for 30 minutes. Before its calcination for 6 hours at 800 °C, the resulting powder was preheated in a furnace for 4 hours at 400 °C[53].

The widely applied method to synthesize a layered $LiTMO_2$ is co-precipitation, where TM represents transition metal (Ni, Mn, or Co). Based on this method, Li et al. produced $Li_{1+x}(Ni_{1/3}Mn_{1/3}Co_{1/3})_{1-x}O_2$. In their study, transition-metal hydroxide and lithium carbonate were employed as starting materials[49].

The production procedure began with dissolving sulfates of the transition metals (Ni, Mn, or Co) in distilled water. NaOH and NH_4OH were simultaneously added to the solution for optimizing the pH. The homogeneously precipitated hydroxide powder $(Ni_{1/3}Mn_{1/3}Co_{1/3})(OH)_2$ was obtained as a result of strong mixing at 40-60 °C for 12 hours. The schematic representation of the procedure explained up to this point is provided in Figure 2.13 Afterward, it was filtered and dried at 120 degrees Celsius for 12 hours. The lithium carbonate (Li_2CO_3) was included in the sample. After grinding and mixing properly, the mixture was heated at 500 °C for 5 hours. The resulting product $Li(Ni_{1/3}Mn_{1/3}Co_{1/3})O_2$ was fired at 950 °C for 10 hours in an air atmosphere.

With the same method, Liang et. al.[54], successfully synthesized the $LiNi_{0.6}Mn_{0.2}Co_{0.2}O_2$ with a spherical shape. In their study, they proved that the products with a spherical shape have high discharge capacity and cycling stability. They also stated that the co-precipitation method is the best way of producing spherical shape NMC materials.

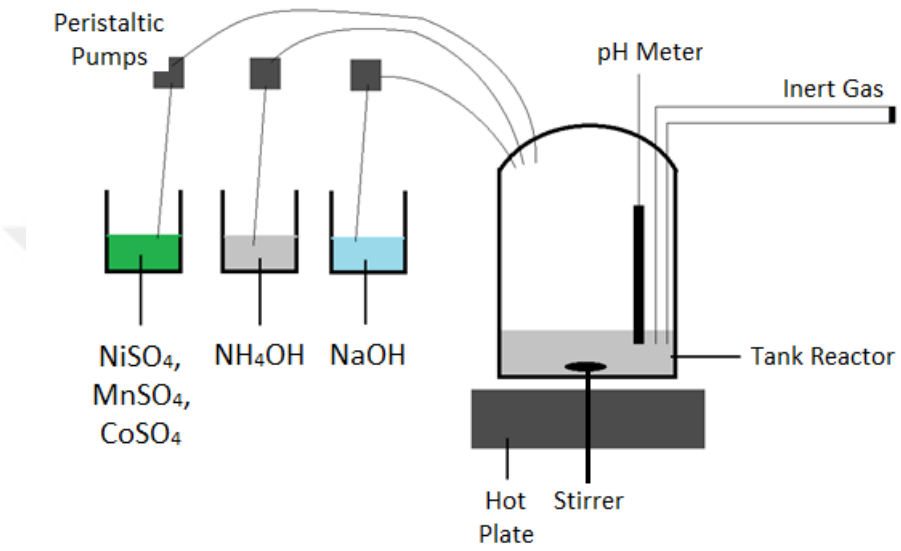


Figure 2.13. Schematic illustration of the synthesis procedure of Ni-rich NMC cathode materials with the co-precipitation method.

Hydrothermal or Solvothermal Synthesis is a synthesizing method whose combination with other conventional technics is possible to enhance the quality of cathode materials. In this regard, it is similar to the co-precipitation method. Another benefit of this method is that it employs less energy than the solid state reaction method, as it reacts faster. Based on the related method, $Li(Ni_{0.6}Mn_{0.2}Co_{0.2})O_2$ was produced by Wang et al.[55]. They began the procedure by dissolving stoichiometric quantities of nickel, manganese, and cobalt acetate in deionized water or ethylene glycol. Then, the obtained solution was conveyed to a continuously stirred reactor tank with pH adjusters. Simultaneously, oxalic acid or ammonium hydroxide was put in it. After the mixing process, the solution was inserted in a Teflon-Lined stainless-steel autoclave with a volume filling ratio of 80%. To obtain the precursors,

the autoclave was sealed and heated at 200 °C for 6 to 18 hours. Afterward, the centrifugal filter with distilled water and ethanol was applied three times separately to them. After filtering, the precursors were dried overnight. They were then mixed with a lithium source and preheated for 5 hours at 450 °C and calcined for 12 hours at 900 °C.

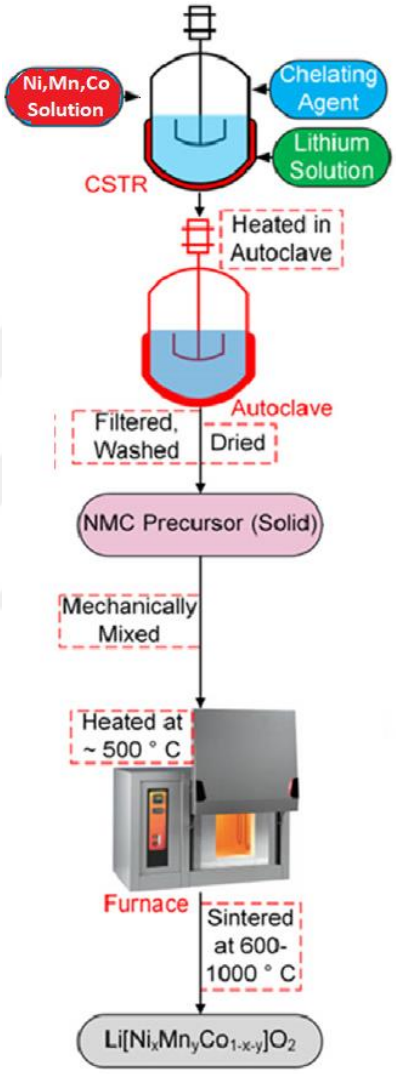


Figure 2.14. Schematic representation of the synthesis procedure of Ni-rich NMC cathode materials with the hydrothermal/solvothermal method[55].

The sol-gel method is widely applied for the preparation of lithium insertion materials. The adaptability of the sol-gel chemistry provides forming of a broad

range of distinct oxides with numerous cations and anions. The main benefit of this method is that it makes the combination of distinct precursors at the molecular level possible. This leads to a homogeneous composition in the gel.

The sol-gel method was studied by Hwang et al.[56], to synthesize $LiNi_{1/3}Co_{1/3}Mn_{1/3}O_2$ with citric acid. They started the procedure by dissolving stoichiometric quantities of lithium acetate ($Li(CH_3COO).2H_2O$), nickel acetate ($Ni(CH_3COO)_2.4H_2O$), cobalt nitrate ($Co(NO_3)_2.6H_2O$), and manganese acetate ($Mn(CH_3COO)_2.4H_2O$) in distilled water. Stirring with an aqueous solution of citric acid was the following step. Then, the obtained solution was stirred with a magnetic stirrer at 80-90 °C for 5-6 h for obtaining a clear viscous gel. After drying the gel in a vacuum oven at 140 °C for 24 hours, the obtained precursor was pre-calcined at 450 °C. Finally, the compound ($LiNi_{1/3}Co_{1/3}Mn_{1/3}O_2$) was ground and calcined at 800°C.

2.4 The Effect of Doping on NMC

To develop the structural stability and electrical conductivity of NMC materials, other elements can be doped in place of nickel, manganese, and cobalt. In order to achieve this, the doping elements in the study of Tianyu Li[57], were chosen according to the bond energy of M-O and the diameter of doping metal ions, where tradeoffs between structural stability and Li^+ movement must be taken into account. For instance, the doping metal ions strongly connected to oxygen can thrive the structural stability and decrease oxygen release, resulting in an adverse effect on Li+ movement because of the increase in the kinetic barriers.

When the distances between atomic layers in the lattice structure increase, the charge-discharge process would be easier. To increase this distance, doping metal ions with a larger diameter should be employed.

Additionally, doping elements can cause the expansion or contraction of NMC lattices and affect the movement of Li ions through bulk particles. Moreover, doping elements with valences from the substituted ions can influence the valences of nickel,

manganese, and cobalt, resulting in an increase or decrease in the capacity since the capacity is obtained by the change of the valence of these elements.

In the doping process, a small amount of another element is introduced into the material in order to alter its electrical or optical properties. Even though the doping elements generally lead to an increase in the material properties including the capacity conservation and electrical conductivity in lithium ion batteries, they decrease their capacities.

Rethwisch et al.[58] examined how doping the Al, Fe, and Sn to the $LiNi_{0.6}Mn_{0.2}Co_{0.2}O_2$ (NMC) cathode material affects the structure and electrochemical performance. Here, the effect of Sn doping on the material was reviewed as it provided the best result in the study. Tin is non-toxic and cheaper than cobalt, having a high bond dissociation energy of 548 kJ mol^{-1} (368 kJ mol^{-1} for Co-O). The results illustrated that the capacity of undoped NMC (170 mAh g^{-1}) was higher than the capacities of doped cathode materials, which was 160 mAh g^{-1} for Sn. Moreover, a 20% increase in the cycle life was observed in dopped NMCs. Higher metal-oxygen bond dissociation energies (such as in Sn-doped NMC) lead to lower lattice expansion during cycling, which has an impact on structural stability. In Figure 2.15, the effects of different dopants on the structure and lattice parameters are indicated.

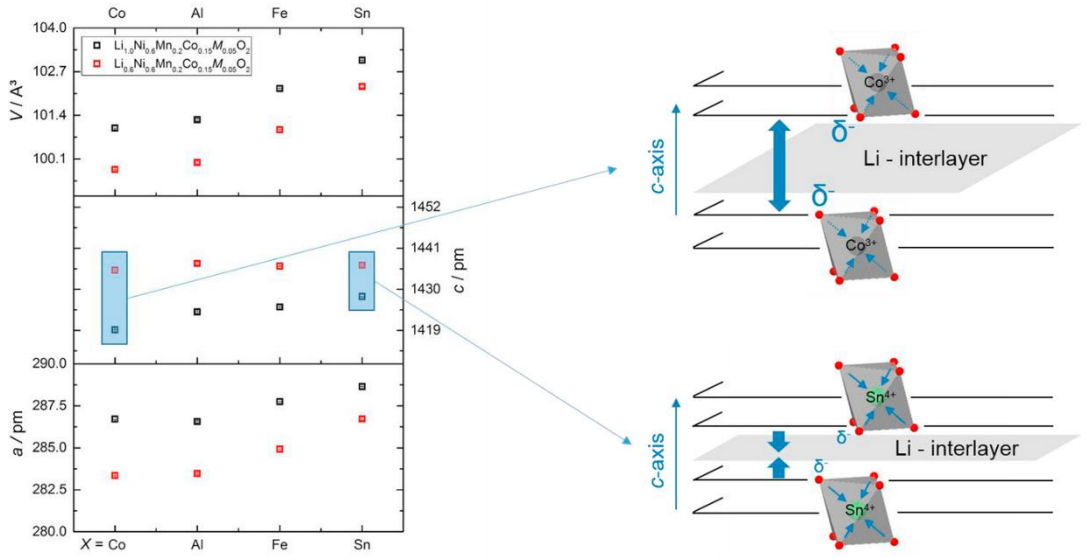


Figure 2.15. Lattice parameter trends of different doped NMC-622 cathode materials in the fully lithiated (black squares) and the 60% delithiated (red squares) state (left). Illustration of the Li-interlayer movement along the c-axis due to doping effects (right)[58].

Liu et al.[59] investigated how doping NMC with Zr and coating it with ZrO_2 affects its structural stability and electrochemical performance. The reduced discharge capacity is because of electrochemically inactive Zr, a typical metal oxide coatings and ion doping problem. Considering the impedance results, the charge transfer resistance of the undoped NMC (7.1Ω - 14.2Ω) doubled after 25 cycles, while the charge transfer resistance of the Zr doped NMC (6.2Ω - 6.8Ω) remained stable. The results showed a 98% increase in capacity retention after 50 cycles when Zr was doped to NMC.

K.J. Park et al.[60] doped boron to $Li[Ni_{0.90}Co_{0.05}Mn_{0.05}]O_2$ cathode. Based on their study, it was proved that doping $Li[Ni_{0.90}Co_{0.05}Mn_{0.05}]O_2$ cathode with 1% boron provides an increase in capacity and capacity retention. During cycling, boron strengthens transition metal-oxygen (TM-O) bonds and maintains the Li-TM-O host structure (B-O bond enthalpy: 809 kJ mol^{-1}). But the final H2 → H3 phase transition triggered an abrupt contraction of the unit cell confined in the c-direction, and a

mechanically strained state was applied to the cathode which later reduced its rechargeability. However, both B0.4 and B1.0 NCM90 cathodes successfully preserved their H2 → H3 peak intensities. These consequences are consistent with the improved cycling stability of the B-doped cathodes. Accordingly, 100 cycles later, its capacity has reached 237 mAh g-1 with a capacity retention of 91%. This is 15% higher than the pure cathode.

Aurbach and Srur-Lavi[61] doped 1 mole of Aluminum to $LiNi_{0.5}Co_{0.2}Mn_{0.3}O_2$ in their study. Al was doped instead of Ni^{2+}, Mn^{4+}, and Co^{3+} ions one by one in the minimum energy structure of undoped $LiNi_{0.5}Co_{0.2}Mn_{0.3}O_2$ using the Density Functional Theory (DFT) and their energy levels were calculated. The most stable form in the structure was observed when Aluminum replaced Ni^{2+}. As a result, it was deduced that Aluminum will replace Ni^{2+}, resulting in a decrease in the capacity. In the first cycle, the capacities of the undoped and doped materials in the capacity tests are 165 and 160 mAh/g, respectively. Considering the results of impedance tests, it was seen that the resistance of Al-doped NMC materials was less than that of the pure NMC material. Moreover, in the capacity retention tests carried out at 0.2 C, while the undoped NMC material lost 3.5% of its capacity after 50 cycles, this value was 1% for the Al-doped NMC.

According studies of Li and Xue[62,63], Mo doping reduces the Li/Ni degree of disorder and extends the lithium slab spacing, being useful to ease the Li ions' diffusion. When looking at the XRD results, it was observed that Li or Mo did not form any diffraction peaks that could be termed secondary phase. It was observed that the discharge capacity of the Mo-doped material was higher than that of the undoped material. Doped Mo atoms increased the number of electroactive Ni^{2+}, allowing Li ions to move more, which led to an increase in capacity. Moreover, in the impedance tests, the charge transfer resistance (R_{ct}) of the undoped and 0.7Mo-doped was 329 Ω and 195.9 Ω, respectively. This drop was because of the good electrical conductivity of Molybdenum.

The diffusion coefficient of Li-ions is vulnerable to the Li gap distance in the layered materials. Based on this, the Li gap was extended by Huang et al.[64] with the introduction of larger Na+ on the Li sites (the Na-doping to the material). This was thought to be useful for facilitating the diffusion of lithium ions. According to the capacity test results, the Na-doped material demonstrated 86.24% capacity retention after 100 cycles while the capacity retention of the undoped material was 83.25%.

The available studies demonstrated that Sm is an efficient element to improve the electrochemical performance of Li-Ion batteries including the initial discharge specific capacity, coulombic efficiency, the Li^+ diffusion channel, and the rate performance. These improvements are because of the high Sm-O bond energy (619 kJ mol^{-1}), large ionic diameter (1.92 Å), and good electrical conductivity[65]. In the study carried out by Kalaiselvi and Kalaignan[66], Sm was doped to the NMC111. The produced sample was found to have great cyclic performance as Sm^{3+} doping resulted in a considerable reduction in impedance and an increase in the Li^+ migration rate. Furthermore, in the capacity retention tests carried out at 1C, although the undoped NMC lost 43% of its capacity after 100 cycles, the Sm-doped NMC material conserved 90.44% of its capacity. Thus, it is inferred the stability of the crystal structure while cycling is maintained by strong Sm-O bonding at high current speeds (1 C).

Thanks to the stable nature of Ti, it is expected to increase the cyclic stability when dopped to NMC materials. In addition, the radius of Ti^{4+} (0.605Å) is smaller than Li^+ (0.74Å) and larger than Ni^{3+} (0.56 Å), Co^{3+} (0.545 Å) and Mn^{4+} (0.53 Å). When Titanium is doped to NMC materials, the lattice parameters will be extended, resulting in the positions of the transition metals being occupied by Ti ions. Du et. al.[67] doped Ti with different ratios to the NMC 811 in order to observe the above-mentioned issue. In the XRD analysis results of the samples, there was a rise in the lattice parameters (a and c) of the NMC 811 doped by 0.02 mole of Ti. XRD analysis after charging indicated a reduction in the crystal lattice volume of the undoped NMC 811 from 101.49 $Å^3$ to 96.95 $Å^3$. On the other hand, the crystal lattice volume of the NMC 811 doped by 0.02 mole of Ti decreased from 101.63 $Å^3$ to

97.59 $Å^3$. This means that while the volume change of the bare material was 4.47%, this value was 3.97% for the Ti-doped NMC material. Thus, it is inferred the deformed volume rate can be considerably reduced by the doping of Ti. Moreover, the capacity retention of the pure and doped materials was 63.5% and 86.9%, respectively in the capacity tests performed at 1 C after 200 cycles.

2.5 Nb Doping to NMC

Among the doping elements, niobium is one of the elements that has not been sufficiently investigated in the area of Ni-rich NMCs. There are few studies on the niobium doping to NMC materials[4–6].

$NMC(OH)_2$ production by Coprecipitation was first performed by Yang et. al.[4]. Afterward, it was mixed with $LiCO_3$ and Nb_2O_5 in a ball mill, and $Li(Ni_{0.5}Co_{0.2}Mn_{0.3})_{1-x}Nb_xO_2$ (x=0.005, 0.01, and 0.02) was produced accordingly. In the study, it was stated that the niobium doping to NMC reduces the Ni/Li cation mixing and simultaneously widens the Li gap and hence facilitating lithium input and output. The clear splitting of the (006)/(102) and (108)/(110) peaks demonstrated that the Nb doping would not have an effect on the highly ordered layered structure. As the Nb^{5+} radius is larger than that of Co^{3+} and Mn^{4+}, the characteristic (003) peak shifted to a lower degree with increasing doping content. Additionally, with respect to the reports, the bond dissociation energy of Nb-O (753 kJ mol^{-1}) is stronger than that of Ni-O (391.6 kJ mol^{-1}), Co-O (368 kJ mol^{-1}), and Mn-O (402 kJ mol^{-1}). For this reason, substituting NB^{5+} into the host structure will depress its degradation and thrive the final electrochemical performances. In the performed impedance tests, the surface film (R_{sf}) and charge-transfer (R_{ct}) resistances of the NMC material doped with 1 mole percent Nb and the pure material were 31.88 Ω to 18.96 Ω and 137.4 Ω to 101.6 Ω, respectively.

Liu et al.[5] produced $LiNMCO_2$ (NMC622) with the solid-state method by mixing $NMC(OH)_2$ and $LiCO_3$, which they bought commercially. They doped Nb^{5+} to the

Li cites on the surface and formed Li_3NbO_4 on the NMC particle surface. In the studies carried out at 55 °C with a 2% doped Nb^{5+} sample, 91% capacity retention was obtained at the end of 80 cycles. This means 6% more capacity retention than the undoped sample. Looking at the XRD analysis results of the samples, any shift in the peaks was not observed. While there was no peak of a foreign phase in the samples doped with 0.5 mole % and 1 mole % Nb, Li_3NbO_4 was observed in the candidate doped with 0.2 moles of Nb. In the HRTEM analyzes performed on all the produced samples, it was seen that a successful Li_3NbO_4 coating layer was formed on the surface. However, partially Nb^{5+} introduction to the structure, resulting in a capacity decrease was observed. Additionally, it was also seen an increase in the capacity reduction with increasing Nb.

Xin et. al.[6] doped 0.7, 1.4, 2.1, 2.8, and 3.5 mole % Nb to NMC 811. In their study, they presented two propositions; because of the Nb^{5+} ionic radius (0.64 Å), it will either displace Li^+ (0.76 Å) or displace TM ions. As the lattice expansion was observed in XRD analysis results on the samples, they concluded that Nb displaced TM ions. Additionally, in the related study, they observed that the Li_3NbO_4 peak value in the XRD graphs increased with the increasing Nb. Moreover, the neutron diffraction results demonstrated that one of the transition metals will be reduced (e.g., the reduction of Ni from Ni^{3+} to Ni^{2+}) to keep charge balance when Nb^{5+} displaces TM. This will increase the effect of cation mixing. In the capacity tests performed on the sample doped with 0.14 moles of Nb, it was seen that the doped NMC had 10% less capacity than that of the pure NMC. However, while the capacity retention of the bare material was 82% after 250 cycles, this value was 95% for the doped material.

Within the scope of the thesis, Nb doping to NMC with the sol-gel method was conducted for the first time. In addition, the effect of niobium on the material was examined as the nickel ratio increases in Ni-rich NMCs.

CHAPTER 3

EXPERIMENTAL PROCEDURE

The first experiment successfully performed within the scope of the thesis was the synthesis of Ni-rich NMC cathode active material by the citric acid assisted modified Pechini sol-gel method. The experimental procedure was identified by blending the studies of Lee et. el.[68] and Klein[69]. In accordance with Lee's study, the ratios of metal nitrates and corresponding citric acids were taken as 1:1 by mole. The amount of ethylene glycol that needs to be added was taken from Klein's study. The temperature (450 °C) and time (6 h) values required for precalcination were taken from Lee's study. The calcination temperatures, and calcination times were tried with NMC 622 in order to find the optimums. As a result, the experimental procedure was enhanced and standardized throughout the thesis. $LiNi_{0.6}Mn_{0.2}Co_{0.2}O_2$, $LiNi_{0.7}Mn_{0.1}Co_{0.2}O_2$, $LiNi_{0.7}Mn_{0.2}Co_{0.1}O_2$, and $LiNi_{0.8}Mn_{0.1}Co_{0.1}O_2$ as Ni-rich NMC cathode active materials in different ratios were chosen.

In the second part of the study, niobium was chosen as a doping element. Accordingly, $Li(NMC)_{1-x}Nb_xO_2$ was synthesized, where x was equal to 0.02, 0.04, and 0.08, respectively.

3.1 Sol-Gel Synthesis

$LiNi_{0.6}Mn_{0.2}Co_{0.2}O_2$, $LiNi_{0.7}Mn_{0.1}Co_{0.2}O_2$, $LiNi_{0.7}Mn_{0.2}Co_{0.1}O_2$, and $LiNi_{0.8}Mn_{0.1}Co_{0.1}O_2$ were prepared employing the citric acid assisted modified Pechini sol-gel method as follows. Citric acid (Sigma Aldrich, 99%) is employed as a chelating agent. On the other hand, ethylene glycol (Alfa Aesar, 99%) is used as a polymerization agent.

Firstly, the amount of citric acid was calculated as a 1:1 molar ratio for each metal ion. In Table 3.1, metal nitrates (Lithium nitrate [Sigma Aldrich, 99%], nickel (II) nitrate hexahydrate [Sigma Aldrich, 99%], manganese (II) nitrate tetrahydrate [Sigma Aldrich, 99%], and cobalt (II) nitrate hexahydrate [Sigma Aldrich, 99%]) and the corresponding citric acid (CA) amounts in grams are presented. 11.43 ml of ethylene glycol was added per 0.1 mole of material in all samples.

Table 3.1. The amounts of metal nitrate and corresponding citric acid required to produce 0.1 mol of $LiN_xM_yC_zO_2$ with sol-gel method.

NMC Ratio	**Mole**	**Lithium**		**Nickel**		**Manganese**		**Cobalt**	
		Nitrate (g)	**CA (g)**	**Nitrate (g)**	**CA (g)**	**Nitrate (g)**	**CA (g)**	**Nitrate (g)**	**CA (g)**
622	0.1	7.24	22.06	17.45	12.61	5.02	4.20	5.82	4.20
712	0.1	7.24	22.06	20.36	14.71	2.51	2.10	5.82	4.20
721	0.1	7.24	22.06	20.36	14.71	5.02	4.20	2.91	2.10
811	0.1	7.24	22.06	23.26	16.81	2.51	2.10	2.91	2.10

Secondly, citric acid was added to four separate beakers and dissolved in hot distilled water. The stoichiometric amounts of metal ions (Lithium nitrate, nickel nitrate, cobalt nitrate, and manganese nitrate) were added to the aqueous citric acid solutions in beakers. Lithium nitrate was always put in excess of 5%. Figure 3.1-a represents the dissolved citric acid and metal ions in beakers.

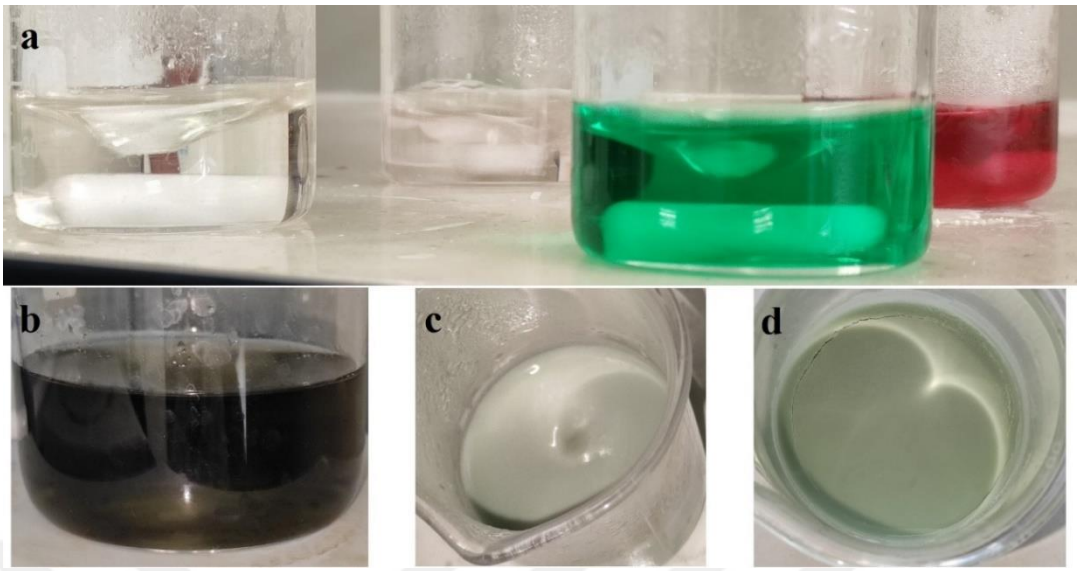


Figure 3.1. Photographs of a) dissolved lithium, manganese, nickel, and cobalt nitrates in citric acid-water solution, b) mixing of all solutions with ethylene glycol and ammonium hydroxide, c) the gelation stage, and d) the gel after drying.

Then, the metallic citrates in the beakers were mixed in one beaker, and the same mole of ethylene glycol with metal ions was added to the beaker as indicated in Figure 3.1-b. The pH of the solution was increased to 7.5 - 8 by adding 25% ammonium hydroxide (Merck, 99%) dropwise. The solution was then mixed at 95 °C until a viscous gel was obtained. The aim was to allow time for gelation while evaporating the water in the solution. The expected mechanism in this process is metal ions chelating by citric acid and ethylene glycol, forming an ester bond between them. The chemical representation of this mechanism is provided in Figure 3.2.

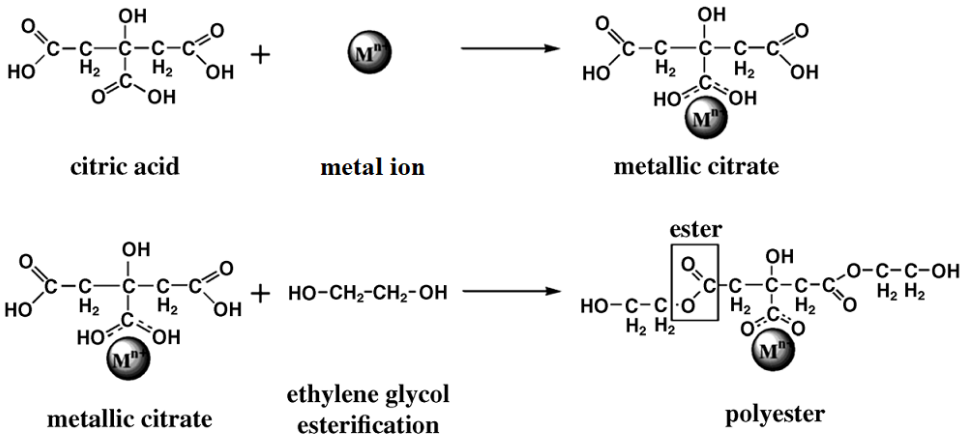


Figure 3.2. A chemical representation of Pechini modified sol-gel mechanism[69].

The resulting gel shown in Figure 3.1-c was dried at 80 °C overnight. After the drying process, it was pre-calcined at 450 °C for 6 h to decompose and eliminate nitrate and citric acid as carbon dioxide, water vapor, and nitric oxide.

The calcination (recrystallization) process followed pre-calcination. Accordingly, the calcination temperature and time were studied with NMC 622. The process was carried out by heating it at 10 °C/min and leaving it to cool on its own. To find the optimum temperature, the sample was calcined at 800, 810, 820, 830, 840, and 850 °C, respectively at a constant calcination time of 12 hours. Then the sample was calcined for 9, 12, 15, 18, 21, and 24 hours, respectively at the optimum temperature in order to determine the optimum time. Accordingly, the optimum temperature and time were identified as 820 °C and 12 hours. In line with this result, all experiments were calcined at 820 °C for 12 hours.

3.2 Niobium Doping to NMC

Before niobium doping to NMC, Ni-rich NMCs in different ratios (622, 721, 712, 811) were produced by the same method outlined in part 3.1 until the calcination step. Only nickel, manganese, cobalt nitrates and their corresponding citric acid amounts were calculated by subtracting the number of moles of niobium to be added. The nitrate and citric acid values for Nb to be added 2% were multiplied by 0.98,

0.96 for 4%, 0.92 for 8%. $Li(NMC)_{1-x}Nb_xO_2$, and Nb_2O_5 amounts in grams are presented in Table 3.2.

Table 3.2. Mass values for Nb doping process.

TM Molar Ratio	Average Molar Mass of $LiNMCO_2$	Amount of $LiNMCO_2$ (gr)	Amount of Nb_2O_5 (gr)
98%	95.866	2	0.028
96%	94.542	2	0.056
94%	91.895	2	0.116

Nb_2O_5 was added to the precalcined Ni-rich NMC and mixed. The steps followed in the procedure are as follows:

- Firstly, Nb_2O_5 was used as the niobium source.
- Secondly, two grams of NMC, the required amount of Nb_2O_5, and ten stainless steel balls with a diameter of 10 mm were put into a 25 ml stainless steel grinding jar.
- Thirdly, the sample was mixed in a Retsch brand PM 100 device at 150 rpm for 1 hour.
- Finally, the mixture was put into the alumina crucible, and the calcination process was continued.

The steps of the experimental procedures followed in parts 3.1 and 3.2 are schematically represented in Figure 3.3.

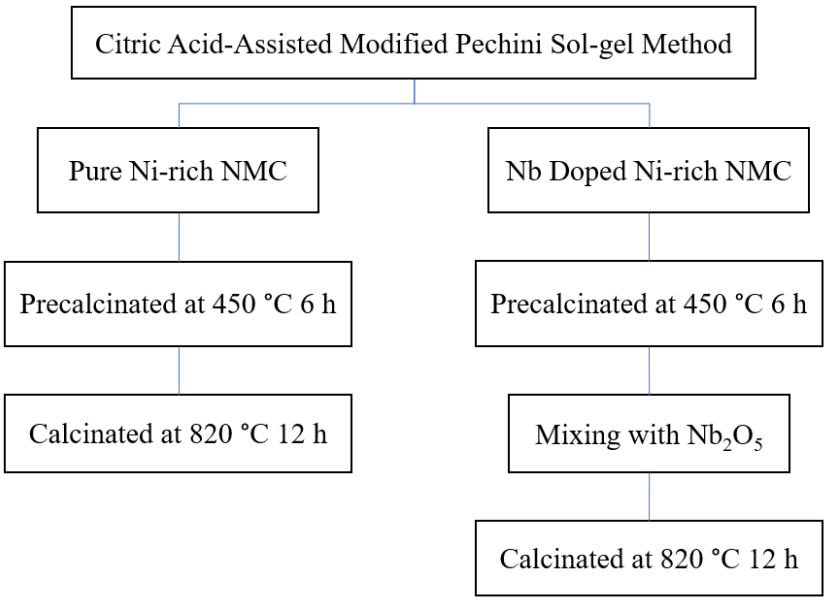


Figure 3.3. Schematic representation of the experimental routes.

Afterward, the calcination process was carried out at the optimum temperature and time (12 hours at 820 °C). Accordingly, $Li(NMC)_{1-v}Nb_vO_2$ was synthesized, where v was equal to 0.02, 0.04, and 0.08.

3.3 Characterization of The Samples

After the preparation of the samples according to the procedures in 3.1 and 3.2 parts, they were characterized with the help of XRD, Scanning Electron Microscope (SEM), ICP, and Energy Dispersive X-Ray Spectroscopy (EDS) (Department of Metallurgical and Materials Engineering, METU).

XRD analysis was performed by using the Bruker D8 Advance device and XRD data were collected between 10 - 80 degrees at a 2 °/min rate. The Match program was employed to observe whether the desired crystal structure was obtained and to understand if another phase was formed in the doped material. In addition to that, the collected XRD data was used in the Rietveld Refinement method, which allows obtaining information about the crystal structure of the samples. Additionally, their oxygen parameters, lattice parameters, and Li-gap values were obtained with the

Rietveld Refinement method. It was carried out by MAUD software[70]. The schematic representation of Li-Gap is shown in Figure 3.4. Equation 3.1 is used to calculate the Li-gap[71,72]. In the equation z represent the oxygen parameter and c represent the lattice parameter of the structure.

$$\mathrm{Li}-\mathrm{Gap}=\left(\frac{2}{3}-(2*\mathrm{z})\right)*\mathrm{c} \tag{3.1}$$

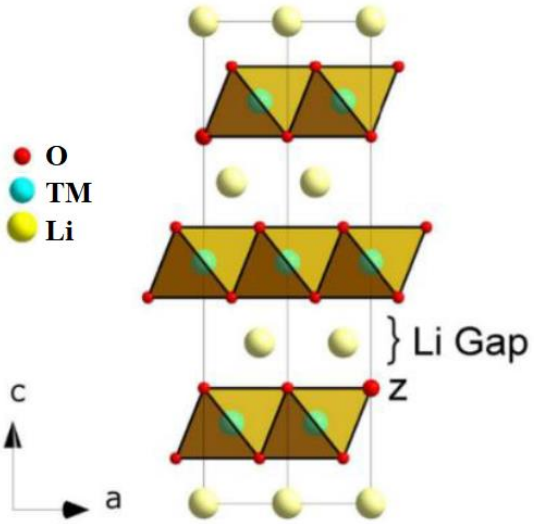


Figure 3.4. Schematic representation of Li-Gap in $LiTMO_2$ structure[72].

The Scanning Electron Microscope (SEM) (Nova NanoSEM 430, FESEM) was employed for examining the morphology and crystallite size of the synthesized powders at different magnifications. The SEM was also employed to determine their chemical composition using the EDS technique. The Inductively Coupled Plasma Optical Emission Spectroscopy (ICP-OES) method was applied for the same purpose using the help of the Agilent 5900 SVDV device for the same purpose. Also, the Inductively Coupled Plasma Mass Spectroscopy (ICP-MS) method was applied for the same purpose using the help of the Perkin Elmer Nexion 350x device for the same purpose.

3.4 Cell Preparation and Electrochemical Tests

The preparation of the working electrodes was carried out based on the following steps:

- First of all, 80 % weight (wt. %) of the synthesized powders/samples mixed with 10 % wt. of carbon black(Sigma Aldrich, 99%) and 10 (wt. %) of polyvinylidene fluoride (PVDF; Sigma Aldrich, 99%) dissolved in N-methyl pyrrolidone (NMP; Sigma Aldrich, 99%). Here, Carbon Black is used as a conducting agent, and PVDF dissolved in NMP is employed as a binder. The ratio of PVDF to NMP in the binder is 5:95.
- The obtained samples were placed in a 50 ml stainless steel jar with ten stainless steel 7 mm balls and mixed for 15 minutes at 20 hertz in a Retsch brand MM 400 device.
- The obtained slurry was coated on aluminum foil with a thickness of 200 microns using Doctor Blade®.
- The foil was dried under a vacuum oven at 120 °C for 2 hours to vaporize the NMP and cut into 18 mm diameter discs.
- The cut discs were dried overnight in an oven at 120 °C under vacuum.
- Lastly, the cathode discs were then placed in the glove box and assembled in a cell.

Lithium metal having an 18 mm diameter was used as an anode, and a glass microfiber separator having an 18 mm diameter was employed for separating the anode and the cathode. 1.0 M LiPF6 dissolved in a 1:1 mixture of EC/PC was used as an electrolyte.

The electrochemical tests were performed using a Biologic MPG-2 potentiostat. The capacity tests were carried out at room temperature between 2.7 - 4.2 volts. The charge-discharge capacity value taken between 2.7 - 4.2 volts for all samples was 1C = 160 mAh/gram. The first charge-discharge capacity tests were performed at a C/10 (0.1 C) rate of 20 cycles. The second test carried out 2 cycles at 0.1 C, then continued

15 cycles at 0.3 C, for 15 cycles at 1 C, and for 2 cycles at 0.1 C. Moreover, all samples were examined before and after 20 cycles at 0.1 C using the Electrochemical Impedance Spectroscopy (EIS) method, and EIS plots were booked. The measurements were performed in the frequency range was adjust 20 kHz - 2 mHz with a 10 mV amplitude.

CHAPTER 4

RESULTS AND DISCUSSION

There are two main parameters in the literature that attract attention during the synthesis of nickel rich NMC Li-ion cathode materials. These are calcination time and calcination temperature.

To minimize the effects caused by these parameters and highlight the production with the sol-gel method, $LiNi_{0.6}Mn_{0.2}Co_{0.2}O_2$ was calcined at different calcination times and calcination temperatures after its pre-calcination at 450 °C for 6 hours. To carry out the study, one of the parameters must be kept constant. At this point, the study of Longwei[54] was examined, and it was observed that the optimum time was 12 hours.

Accordingly, six calcination experiments were carried out at 800, 810, 820, 830, 840, and 850 °C, respectively, taking the optimum time of 12 hours. XRD analysis was performed on the obtained $LiNi_{0.6}Mn_{0.2}Co_{0.2}O_2$ samples.

It can be seen from Figure 4.1 that the NMC structures were obtained successfully. In all samples calcined at different temperatures, the layered structure can be seen in the splitting of the (018) and (110) peaks as well as the (006) and (012) peaks.

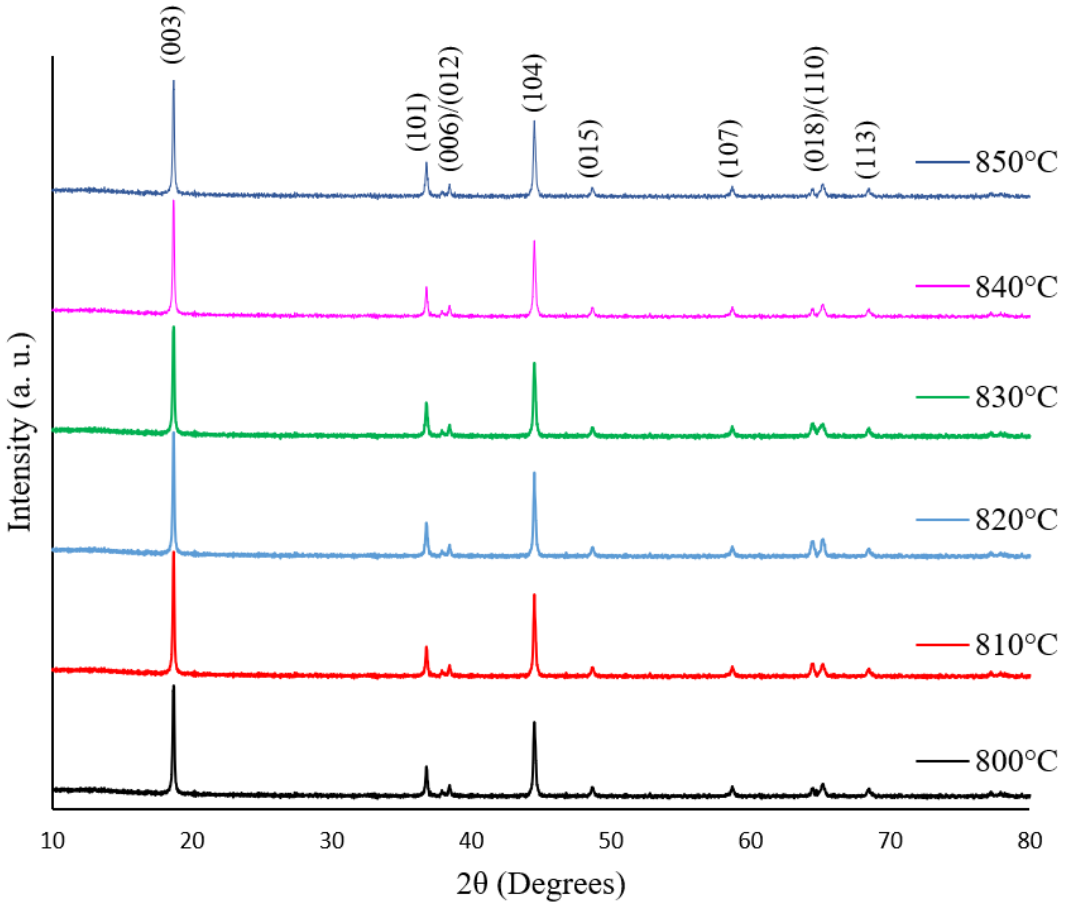


Figure 4.1. XRD patterns of temperature-dependent calcinations of pure NMC 622.

The $I_{(003)}/I_{(104)}$ ratios obtained from XRD graphs of the samples are provided in Table 4.1. According to the table, the highest $I_{(003)}/I_{(104)}$ ratio (1.84) belongs to the sample calcined at 820 °C for 12 hours.

Table 4.1. $I_{(003)}/I_{(104)}$ ratio of samples calcined at different temperatures.

Temperature	800 °C	810 °C	820 °C	830 °C	840 °C	850 °C
$I_{(003)}/I_{(104)}$	1.420	1.448	1.463	1.408	1.414	1.418

The lattice parameters (a and c) of the $LiNi_{0.6}Mn_{0.2}Co_{0.2}O_2$ samples produced with different calcination temperatures in Table 4.2 were obtained from the Rietveld analysis performed on the XRD results in Table 4.1. Additionally, a weighted profile

residual (R_{wp}%) is given in the table. Before reviewing the data, a weighted profile residual should be checked. It should be lower than 20%. Otherwise, it means it is not a successful analysis. Additionally, the ratio c/a higher than 4.899 is an indication of high cation order[73]. As the R_{wp}% of the samples is lower than 20% (Table 4.2), it makes sense to review the results. According to the c/a values presented in the table below, all samples have high cation order.

Table 4.2 The lattice parameters of samples calcined at different temperatures.

Temperature	**a(Å)**	**c(Å)**	**c/a**	**R_{wp}%**
800 °C	2.864	14.243	4.973	8.97
810 °C	2.864	14.245	4.973	8.96
820 °C	2.864	14.245	4.974	8.73
830 °C	2.865	14.239	4.970	8.37
840 °C	2.864	14.245	4.974	9.03
850 °C	2.864	14.246	4.974	9.72

Based on the results, the experiment was carried out at different calcination times, 9, 15, 18, 21, and 24 hours, respectively, keeping the temperature constant at 820 °C. As the calcination at 820 °C for 12 hours was carried out, it was not repeated. XRD analysis was performed on the obtained samples.

In Figure 4.2, it can be seen that the NMC structures were obtained successfully. In all samples calcined at different times, the layered structure can be seen in the splitting of (110)/(018) and (006)/(012) peaks.

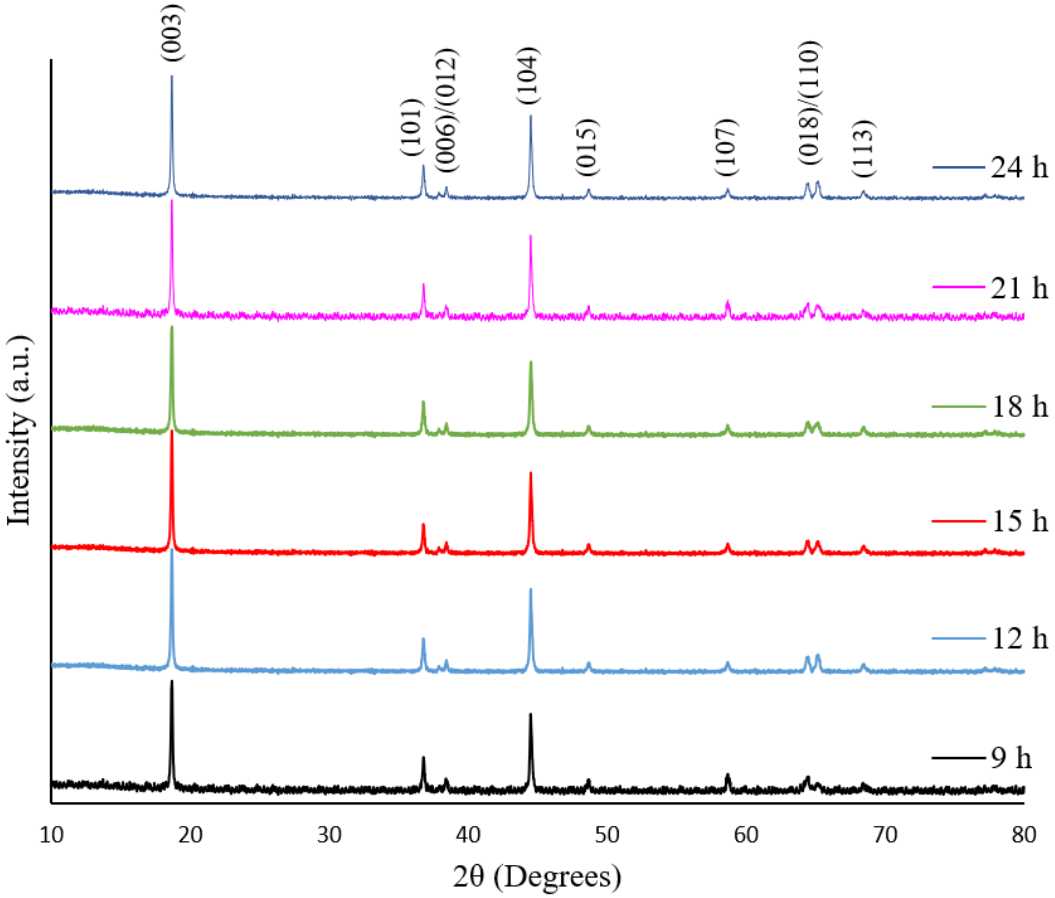


Figure 4.2. XRD patterns of time-dependent calcinations of pure NMC 622.

The $I_{(003)}/I_{(104)}$ ratios obtained from XRD graphs of the samples are provided in Table 4.3. According to the table, the highest $I_{(003)}/I_{(104)}$ ratio (1.463) belongs to the sample calcined at 820 °C for 12 hours. Similarly, the R_{wp}% of the samples provided in Table 4.4 proves the success of the experiment. In addition, all samples have high cation order according to the c/a values presented in the table below.

Table 4.3. $I_{(003)}/I_{(104)}$ ratio of samples calcined at different times.

Time	9 h	12 h	15 h	18 h	21 h	24 h
$I_{(003)}/I_{(104)}$	1.372	1.463	1.452	1.411	1.374	1.405

Table 4.4. The lattice parameters of samples calcined at different times.

Time	a (Å)	c (Å)	c/a	R_{wp}%
9 h	2.864	14.251	4.975	14.72
12 h	2.864	14.245	4.974	8.73
15 h	2.864	14.244	4.973	8.96
18 h	2.864	14.239	4.972	8.35
21 h	2.865	14.254	4.976	15.18
24 h	2.864	14.246	4.974	9.77

When looking at the $I_{(003)}/I_{(104)}$ ratios in Tables 4.1 and 4.3 obtained from XRD graphs of the samples, the optimum calcination temperature and time are 820 °C and 12 hours, respectively. This means the effect of cation mixing will be low when the sample is calcined at 820 °C for 12 hours. The maximum capacity will be obtained as Li ions will occupy their own sites.

4.1 Characterization of Powders

Four distinct materials with Ni, Mn, and Co ratios of 60%/20%/20%, 70%/20%/10%, 70%/10%/20%, and 80%/10%/10%, respectively were produced within the scope of the examination of Ni-rich NMC Li-ion cathode materials produced by the citric acid assisted Pechini modified sol-gel method.

In Table 4.5, the calculated and obtained product amounts in grams are indicated. Despite the losses that may occur during the experiment, the obtained quantities are higher than 90% of the calculated quantities.

Table 4.5 Calculated and obtained weights for sol-gel method.

Compositions	Calculated (g)	Obtained (g)
$LiNi_{0.6}Mn_{0.2}Co_{0.2}O_2$	9.735	9.32
$LiNi_{0.7}Mn_{0.2}Co_{0.1}O_2$	9.733	9.12
$LiNi_{0.7}Mn_{0.1}Co_{0.2}O_2$	9.772	9.24
$LiNi_{0.8}Mn_{0.1}Co_{0.1}O_2$	9.770	9.15

In order to characterize the produced materials, the samples were collected after precalcination and calcination steps. Following precalcination, the samples were characterized with SEM and EDS techniques.

4.1.1 ICP Results of Powders

The results of the ICP OES chemical analysis of the pure samples in mg/kg and the molar ratios of nickel, manganese, and cobalt calculated based on the equation 4.1 and 4.2 provided below are indicated in Table 4.6. Where M_w means Molecular Weight.

$$Total\ M_w\ of\ LiNi_xMn_yCo_zO_2 = M_wLi * 1 + M_wNi * x + M_wMn * y + M_wCo * z + M_wO * 2 \quad (4.1)$$

$$Element\% = \frac{ICP\ Value\ of\ Element(ppm) * Total\ M_w}{M_w\ of\ Element * 10000} \quad (4.2)$$

It can be seen from Table 4.6 that the pure samples were successfully obtained stoichiometrically in the desired amount. According to the ICP results indicated in the table, it is satisfied in NMC 622, 712, and 721. Furthermore, the mole of lithium is barely below 1 in the NMC 811 sample (0.9952). However, this is a negligible

difference. As the molar ratios of manganese in the samples provided in Table 4.6 are close to the desired molar ratio of manganese (10% or 20%), the difference is negligible. In future studies where the sol-gel method is used, the manganese source can be added in the 1% or 2% excess.

Table 4.6. ICP results and corresponding mole ratios of pure NMC samples.

Sample	**Li ppm (mg/kg)**	**Ni ppm (mg/kg)**	**Mn ppm (mg/kg)**	**Co ppm (mg/kg)**	**Li%**	**Ni%**	**Mn%**	**Co%**
Pure 622	72855	365225	110612	123479	100.96%	60.35%	19.51%	20.30%
Pure 721	74830	423143	111712	60934	100.78%	69.91%	19.70%	10.02%
Pure 712	73986	428065	54712	122783	102.52%	70.74%	9.65%	20.19%
Pure 811	71815	488065	55324	61531	99.52%	80.65%	9.76%	10.12%

Before Nb doping, $Li(NMC)_{1-x}O_2$ samples (x = 0.02, 0.04, 0.08) in 4 different compositions (NMC 622, 721, 712, and 811) were produced with the sol-gel method and then pre-calcined at 450 °C for 6 hours as mention in part 3.1. ICP results of the relevant samples are provided in Table 4.7. Accordingly, it is seen from the table that the requested stoichiometric results of the samples are obtained based on the calculated with equations 4.1 and 4.2.

Table 4.7. ICP results and corresponding mole ratios of pre-pure NMC samples.

Sample	Li ppm (mg/kg)	Ni ppm (mg/kg)	Mn ppm (mg/kg)	Co ppm (mg/kg)	Li%	Ni%	Mn%	Co%
2% pre-622	73431	378350	116185	124845	101.75%	62.52%	20.49%	20.53%
2% pre-721	73912	419323	112421	62031	99.52%	80.65%	9.76%	10.12%
2% pre-712	73627	427835	54118	123072	102.03%	70.70%	9.54%	20.23%
2% pre-811	76123	485182	50994	62412	102.42%	69.29%	19.83%	10.20%
4% pre-622	74762	362520	113432	124723	103.60%	59.91%	20.01%	20.51%
4% pre-721	75892	423727	119025	61326	105.16%	70.20%	20.99%	10.08%
4% pre-712	74351	430216	55324	121522	103.03%	71.09%	9.76%	19.98%
4% pre-811	77730	491644	52267	61154	107.71%	81.24%	9.22%	10.05%
8% pre-622	78534	370128	108232	122332	108.83%	61.16%	19.09%	20.11%
8% pre-721	77035	427835	106185	60484	106.75%	70.70%	18.73%	9.94%
8% pre-712	76762	422565	53848	121783	106.37%	69.83%	9.50%	20.02%
8% pre-811	78172	480232	55233	60622	108.32%	79.36%	9.74%	9.97%

After doping Nb to the samples and calcining them at 820 °C for 12 hours, the ICP MS was employed for analyzing the candidates. ICP results of the relevant samples are provided in Table 4.8. Accordingly, it is seen from the table that the requested stoichiometric results of the samples are obtained.

Table 4.8. ICP results and corresponding mole ratios of Nb containing NMC samples.

Sample	Li ppm (mg/kg)	Ni ppm (mg/kg)	Mn ppm (mg/kg)	Co ppm (mg/kg)	Nb ppm (mg/kg)	Li%	Ni%	Mn%	Co%	Nb%
2% 622	72431	354304	111081	118238	1859	101.3%	59.1%	19.8%	19.6%	2.05%
2% 721	73114	413273	110131	59243	1799	102.2%	68.9%	19.6%	9.8%	1.98%
2% 712	72972	415293	52115	117632	1812	102.0%	69.2%	9.3%	19.5%	1.99%
2% 811	75297	472564	51203	57854	1834	105.3%	788%	9.1%	9.6%	2.02%
4% 622	72536	351231	107199	116153	3654	101.4%	58.6%	19.1%	19.3%	3.99%
4% 721	72862	409167	108922	55532	3712	101.9%	68.2%	19.4%	9.21%	4.06%
4% 712	73292	406938	49407	117023	3548	102.5%	67.8%	8.8%	19.4%	3.88%
4% 811	73728	474239	47274	54207	3675	103.1%	79.1%	8.4%	8.9%	4.02%
8% 622	72514	338232	101112	109332	7194	101.4%	56.4%	17.9%	18.1%	7.75%
8% 721	71318	405275	100073	47316	7388	99.7%	67.6%	17.8%	7.9%	7.96%
8% 712	72005	408225	42848	104783	7512	100.7%	68.1%	7.6%	17.4%	8.09%
8% 811	72144	468427	47686	48012	7444	100.9%	78.1%	8.5%	7.9%	8.02%

4.1.2 XRD Results of Powders

XRD data in Figure 4.3 shows that NMC 622, 712, 721, and 811 were produced successfully. The second phase formation was not observed in the samples. Moreover, the layered structure can be seen in the splitting of the (110) and (018) peaks as well as the (006) and (012) peaks.

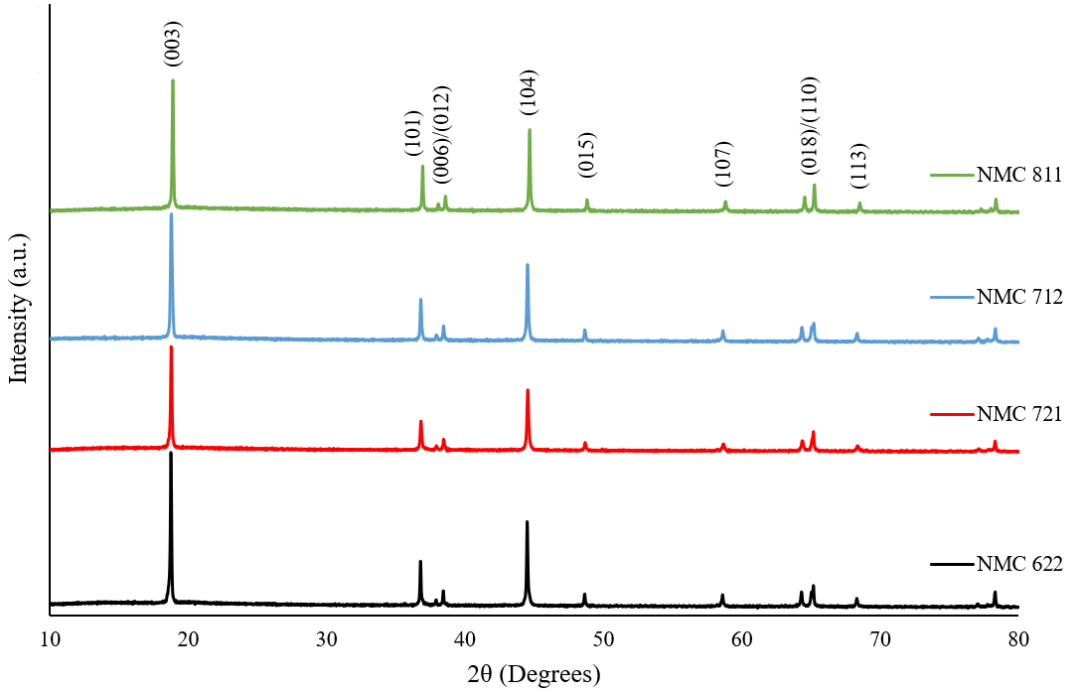


Figure 4.3. Pure nickel rich NMCs XRD graph.

The lattice parameters (a and c), oxygen parameter (z) of the NMC 622, 712, 721, and 811 in Table 4.7 are obtained from Rietveld analysis performed on the XRD results of the relevant NMC materials. Additionally, the calculated Li-gap based on the experimental procedure in part 3.3 and a weighted profile residual (R_{wp}%) are given in the table.

As mentioned earlier, a weighted profile residual should be checked according to the c/a values presented in the table. Based on the R_{wp}% value of the samples in Table 4.7, it can be concluded that the analysis was successful.

According to the results presented in the table, all samples have high cation order because their ratio c/a is higher than 4.899. The value of both a and c gets smaller from NMC 622 (2.8727 Å and 14.2875 Å) to NMC 811 (2.8696 Å and 14.2649 Å). This is the result of increasing Ni content in the material. Moreover, the Li-gap tightens from NMC 622 (2.63585 Å) to NMC 811 (2.63225 Å) as it is directly related to the lattice parameter c and oxygen parameter z.

Moreover, it is seen that the a and c of NMC 712 (2.8716 Å and 14.2772 Å) are smaller than those of NMC 721 (2.8749 Å and 14.2845 Å), comparing the lattice parameters of NMC 721 and NMC 712. The obtained results are supportive of the study of Zheng Li, which mentioned cobalt shortens the lattice parameters more than manganese[29].

When looking at the table, the $I_{(003)}/I_{(004)}$ gets smaller from NMC 622 to NMC 811. It is inferred that nickel ions occupy lithium sites with rising Ni content in the material. This means the effect of cation mixing raises as a result of increasing Ni content.

Table 4.9. The lattice parameters of pure samples.

Sample	**$I_{(003)}/I_{(104)}$**	**a (Å)**	**c (Å)**	**c/a**	**Oxygen Parameter (z)**	**Li-Gap**	**R_{wp} %**
P622	1.743	2.875	14.288	4.970	0.24109	2.63585	11.96
P721	1.628	2.875	14.285	4.969	0.24108	2.63559	11.57
P712	1.591	2.872	14.277	4.972	0.24109	2.63395	10.39
P811	1.540	2.870	14.265	4.971	0.24107	2.63225	12.19

Figure 4.4 shows the successful synthesis of $Li(NMC)_{0.98}Nb_{0.02}O_2$ materials in all compositions. The characteristic (211) and (440) peaks of Li_3NbO_4 formation are faintly visible, which indicates that not all of the 2% Nb-doped is incorporated into the $LiNMCO_2$ structure and some of it forms Li_3NbO_4.

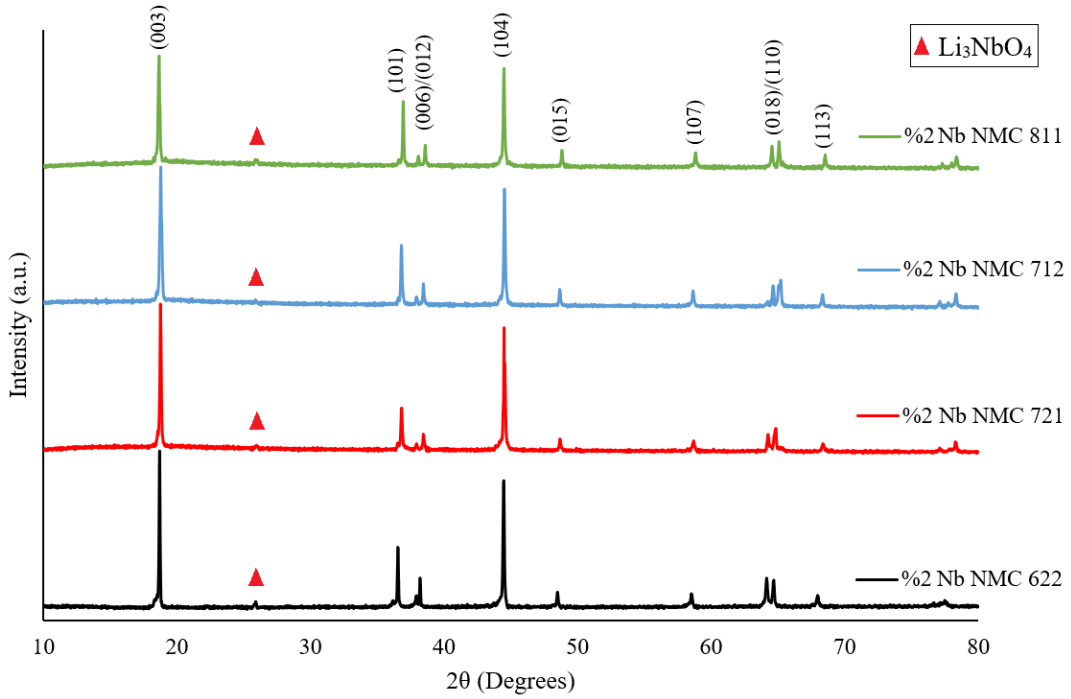


Figure 4.4. 2% Nb contained nickel rich NMCs XRD graph.

The results of the Rietveld refinement analysis performed by employing $LiNMCO_2$ and Li_3NbO_4 CIF (Crystallographic Information File) are provided in Table 4.10 and Table 4.11.

Table 4.10. The lattice parameters of 2% Nb containing samples.

Sample	$I_{(003)}/I_{(104)}$	a (Å)	c (Å)	c/a	Oxygen Parameter (z)	Li-Gap	R_{wp} %
2% 622	1.226	2.873	14.287	4.973	0.24106	2.63667	11.88
2% 721	1.176	2.873	14.297	4.977	0.24107	2.63816	11.39
2% 712	1.169	2.872	14.290	4.975	0.24111	2.63561	10.99
2% 811	1.112	2.871	14.280	4.975	0.24092	2.63927	11.74

Table 4.11. Phase ratio according to Rietveld analysis.

Sample	$LiNMCNbO_2$ wt.%	Li_3NbO_4 wt.%
2% 622	99.12%	0.88%
2% 721	99.31%	0.69%
2% 712	99.27%	0.73%
2% 811	99.43%	0.57%

Moreover, the % weight of two different structures ($Li(NMCNb)O_2$ and L_3NbO_4) formed is provided in the same table. An excess of the 2% Nb-doped to each NMC composition formed a new phase, Li_3NbO_4.

When the molar ratios of $Li(NMCNb)O_2$ and L_3NbO_4 were calculated based on their molar weights (97 g/mol, and 178 g/mol, respectively), it was seen that around more than 3/4 of niobium doped to NMC 622 contributed to the structure and the remaining less than 1/4 formed the Li_3NbO_4 phase. The niobium amount incorporated into the structure increases with increasing nickel content.

When looking at Table 4.10, it can be observed that the lattice parameter (a) of NMC samples doped with 2% Nb gets smaller from NMC 622 (2.873 Å) to NMC 811 (2.871 Å). When compared to the lattice parameter (a) of pure and doped samples in Tables 4.9 and 4.10, it is seen that a is higher in pure NMC 622 than that of doped-NMC 622. On the other hand, the lattice parameter (a) of pure NMC 811 is lower than that of doped-NMC811 because the niobium amount incorporated into the structure increases with increasing nickel content.

When the lattice parameter (c) of the pure materials and corresponding doped materials with 2% Nb is compared, it is seen that the lattice parameter (c) of all doped materials is higher than that of pure ones.

Looking at the Li-Gap values of the NMC materials, the largest value belongs to the NMC 811. There is no specific relationship among other compositions.

The $I_{(003)}/I_{(004)}$ ratio demonstrating the effect of cation mixing is above 1.2 (acceptable) for NMC 622 while it remains below 1.2 for NMC 721, 712, and 811 compositions.

The XRD results of all compositions doped with the 4% Nb are provided in Figure 4.5. As understood from the (211) and (440) peaks, the Li_3NbO_4 phase clearly manifests itself as a second phase.

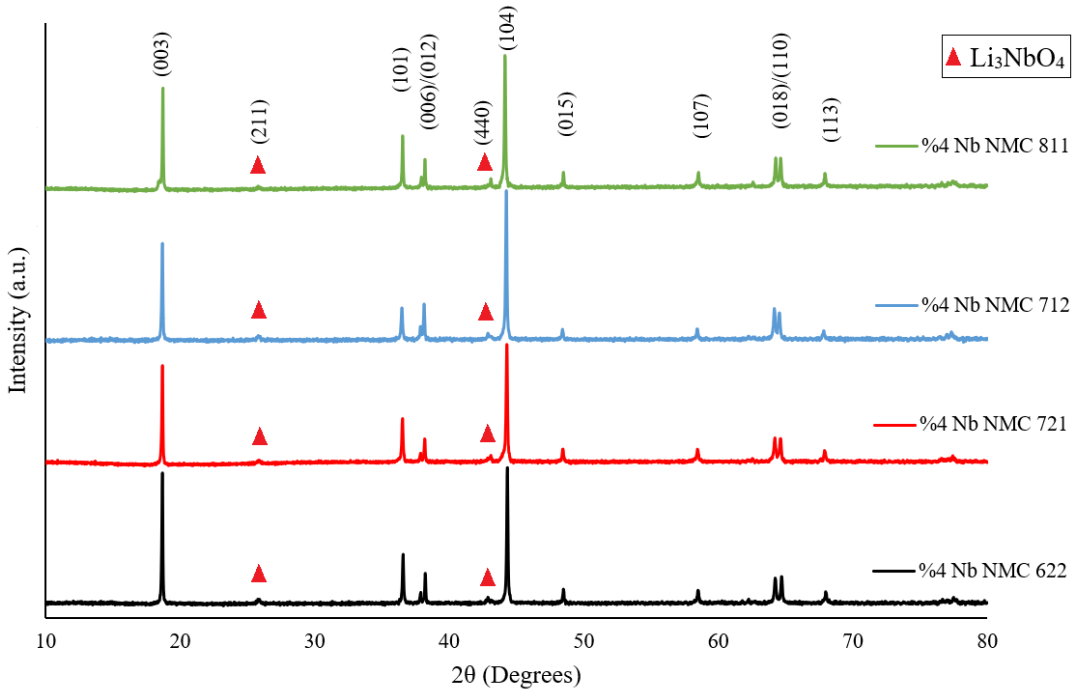


Figure 4.5. 4% Nb containing nickel rich NMCs XRD graph.

The results of the Rietveld Refinement analysis performed on all samples doped with 4% Nb using $LiNMCO_2$, and Li_3NbO_4 CIF (Crystallographic Information File) are provided in Table 4.12 and 4.13.

Table 4.12. The lattice parameters of 4% Nb containing samples.

Sample	$I_{(003)}/I_{(104)}$	a (Å)	c (Å)	c/a	Oxygen Parameter (z)	Li-Gap	R_{wp} %
4% 622	0.965	2.857	14.327	5.014	0.24108	2.64348	14.73
4% 721	0.838	2.718	14.297	5.260	0.24112	2.63673	17.03
4% 712	0.684	2.691	14.214	5.281	0.24404	2.53850	14.76
4% 811	0.776	2.869	14.173	4.941	0.24123	2.61078	12.03

Table 4.13. Phase ratio according to Rietveld analysis.

Sample	$LiNMCNbO_2$ wt.%	Li_3NbO_4 wt.%
4% 622	97.07%	2.93%
4% 721	97.76%	2.24%
4% 712	97.67%	2.33%
4% 811	98.17%	1.83%

Increase in the Nb content (from 2% to 4%) leads to the increase in the Li_3NbO_4 phase formation as seen clearly in Table 4.13. Furthermore, it is observed that Ni^{2+} occupy Li cites based on looking at the $I_{(003)}/I_{(004)}$ values from Table 4.12. These values (0.965, 0.838, 0.684, and 0.776) are so below the acceptable limits (1.2) of a NMC cathode material. It is also seen from the same table that the lattice parameters, i.e., a and c shorten and lengthen, respectively. This leads to the c/a values to be well above the usual values (4.899).

The XRD results of all compositions containing 8% Nb are provided in Figure 4.6. It is observed that the characteristic splitting peaks of $LiNMCO_2$ materials (006)/(012) and (018)/(110) have disappeared. On the other hand, the (211) and (440) peaks belonging to Li_3NbO_4 manifest themselves clearly. As understood from the (211) and (440) peaks, the Li_3NbO_4 phase clearly manifests itself as a second phase.

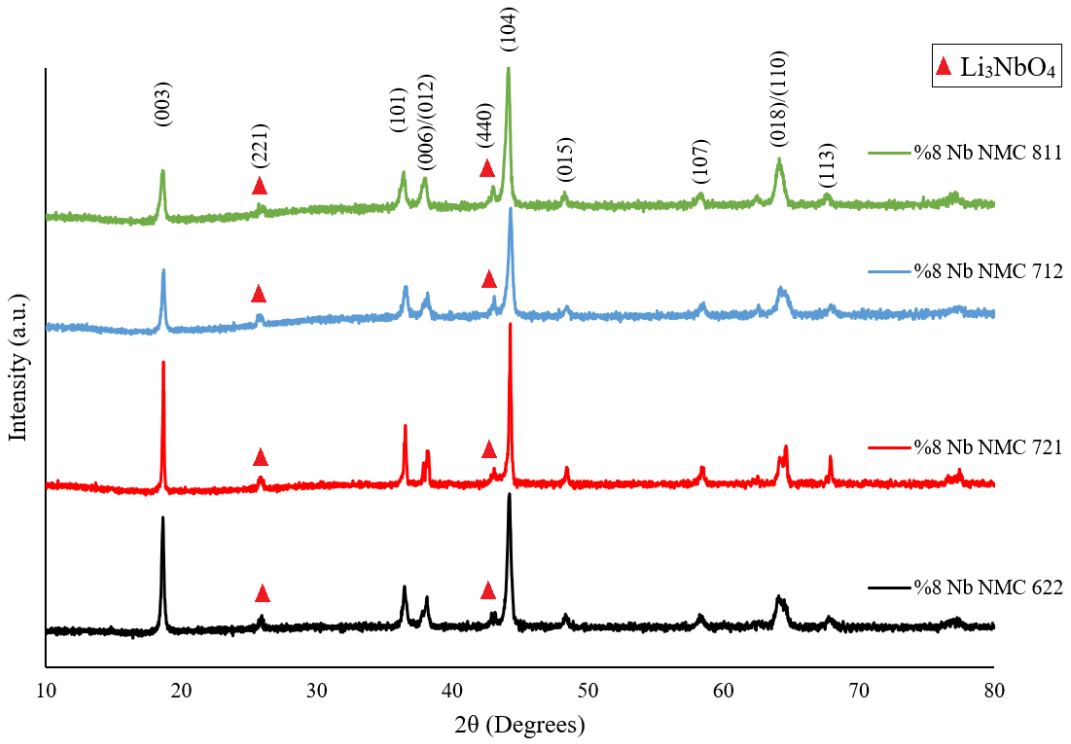


Figure 4.6. 8% Nb containing nickel rich NMCs XRD graph.

In Table 4.14, it is seen that the $I_{(003)}/I_{(004)}$ of all compositions is much below the requested value. Therefore, it is understood that the doped Nb disturbs the structure of $LiNMCO_2$ in addition to resulting in the formation of the second phase (Li_3NbO_4).

Considering the $I_{(003)}/I_{(004)}$ far below the requested value (1.2), the disappearance of (006)/(012) and (018)/(110) splitting peaks, demonstrating that $LiNMCO_2$ has a layered structure, and excess of the formed unwanted secondary phase (Li_3NbO_4 structure) the doping studies with 0.04 and 0.08 moles of Nb was not carried out.

Hereinafter, pure nickel rich NMC samples are named as their composition with “P” prefixed (P622, P721, P712, P811). Nickel rich NMC samples containing 2% Nb will be named as their composition with the prefix “D” (D622, D721, D712, D811).

Table 4.14. The lattice parameters of 8% Nb containing samples.

Sample	$I_{(003)}/I_{(104)}$	a (Å)	c (Å)	c/a	Oxygen Parameter (z)	Li-Gap	R_{wp} %
8% 622	0.863	2.883	14.122	4.899	0.24606	2.46497	13.18
8% 721	0.803	2.840	14.335	5.047	0.24087	2.65085	12.37
8% 712	0.587	2.891	14.412	4.985	0.24063	2.67214	17.62
8% 811	0.426	2.866	14.082	4.914	0.24191	2.57479	15.47

Table 4.15. Phase ratio according to Rietveld analysis.

Sample	$LiNMCNbO_2$ wt.%	Li_3NbO_4 wt.%
8% 622	92.88%	7.12%
8% 721	93.21%	6.79%
8% 712	93.17%	6.83%
8% 811	93.48%	6.52%

4.1.3 SEM Application of Powders

4.1.3.1 SEM Analyses After Precalcination

The SEM photographs of the NMC materials (NMC 622, 721, 712, and 811) produced with the citric acid assisted Pechini sol-gel method, pre-calcined at 450 °C for 6 hours, is provided in Figure 4.11. As mentioned in part 3.1, pre-calcination was done to eliminate water, nitrate, and citric acid as carbon dioxide, water vapor, and nitric oxide in the mixture formed after the sol gel. As can be seen in the figure, a sponge shape has appeared for all samples due to gas outlets.

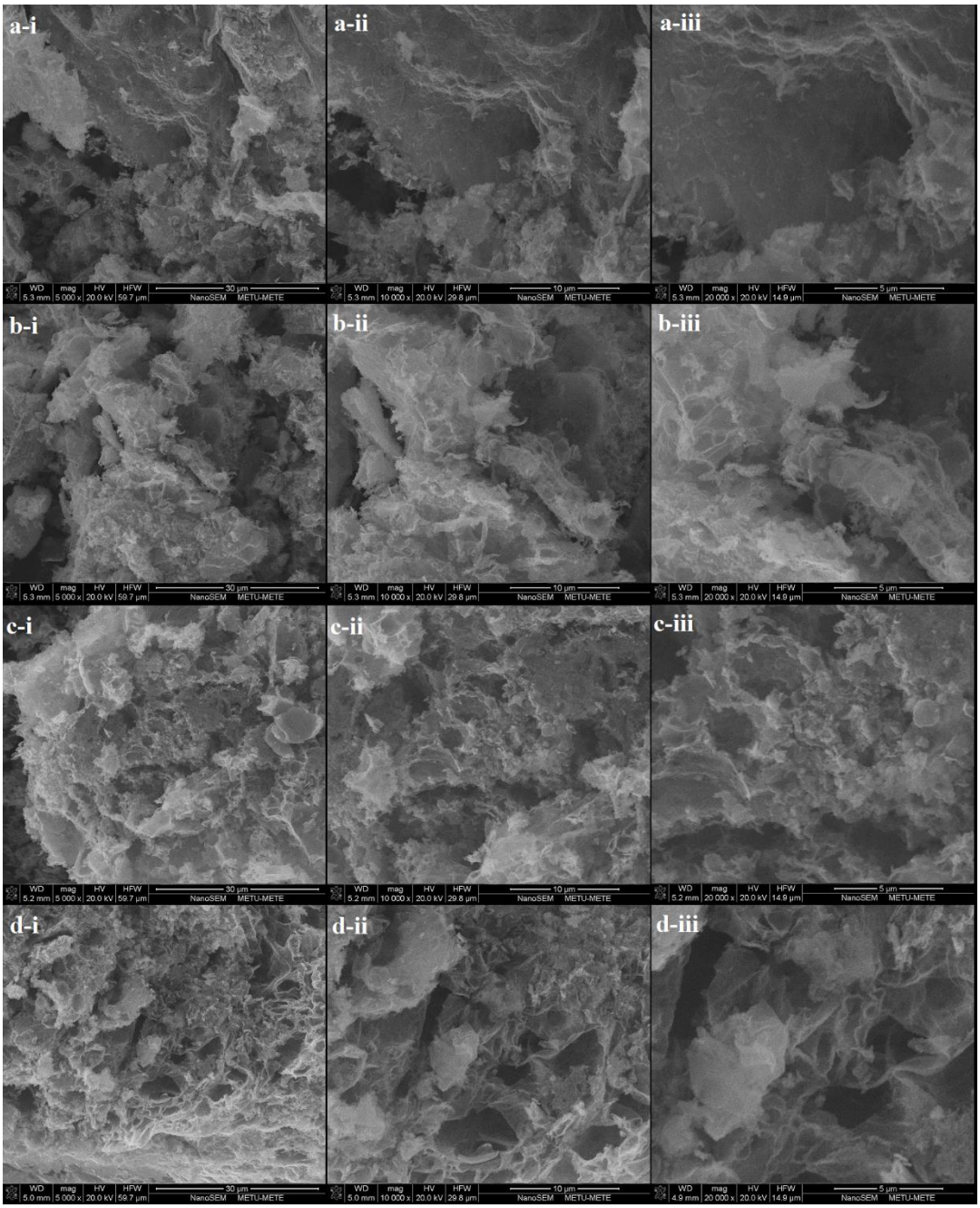


Figure 4.7. SEM images of pre-pure a) $LiNi_{0.6}Mn_{0.2}Co_{0.2}O_2$, b) $LiNi_{0.7}Mn_{0.2}Co_{0.1}O_2$, c) $LiNi_{0.7}Mn_{0.1}Co_{0.2}O_2$, d) $LiNi_{0.8}Mn_{0.1}Co_{0.1}O_2$ ([i] 5000, [ii] 10000, and [iii] 20000 magnification for every type of powder).

The chemical analysis was taken from a few different parts of the four distinct samples using Energy Dispersive Spectroscopy (EDS). The average EDS values for

each sample are provided in Table 4.16. When the EDS results are examined, it is seen that the desired compositions are achieved.

Table 4.16. EDS results of pre - pure NMCs.

Sample	Ni%	Mn%	Co%
Pre - Pure 622	60.03%	19.87%	20.10%
Pre - Pure 721	69.92%	20.04%	10.04%
Pre - Pure 712	70.13%	9.73%	20.14%
Pre - Pure 811	79.82%	9.96%	10.22%

4.1.3.2 SEM Application After Calcination

The SEM photograph of the NMC materials (NMC 622, 721, 712, and 811) after calcined at 820 °C for 12 hours is provided in Figure 4.8. Looking at the figure, it is seen that the crystalline particles are formed. The diameter of the primary particles formed because of the calcination of NMC 622 and NMC 721 is between 0.8 and 1.1 micrometers. While the primary particle sizes of NMC 712 range from 0.5 to 0.8 micrometers, the diameter of the primary particles formed due to the calcination of NMC 811 varies between 0.3 micrometers and 0.6 micrometers. The particle sizes of the samples obtained decrease with the increase in the nickel amount, similar to the findings in the study of Hyung-Joo Noh mentioned in part 2.2[33].

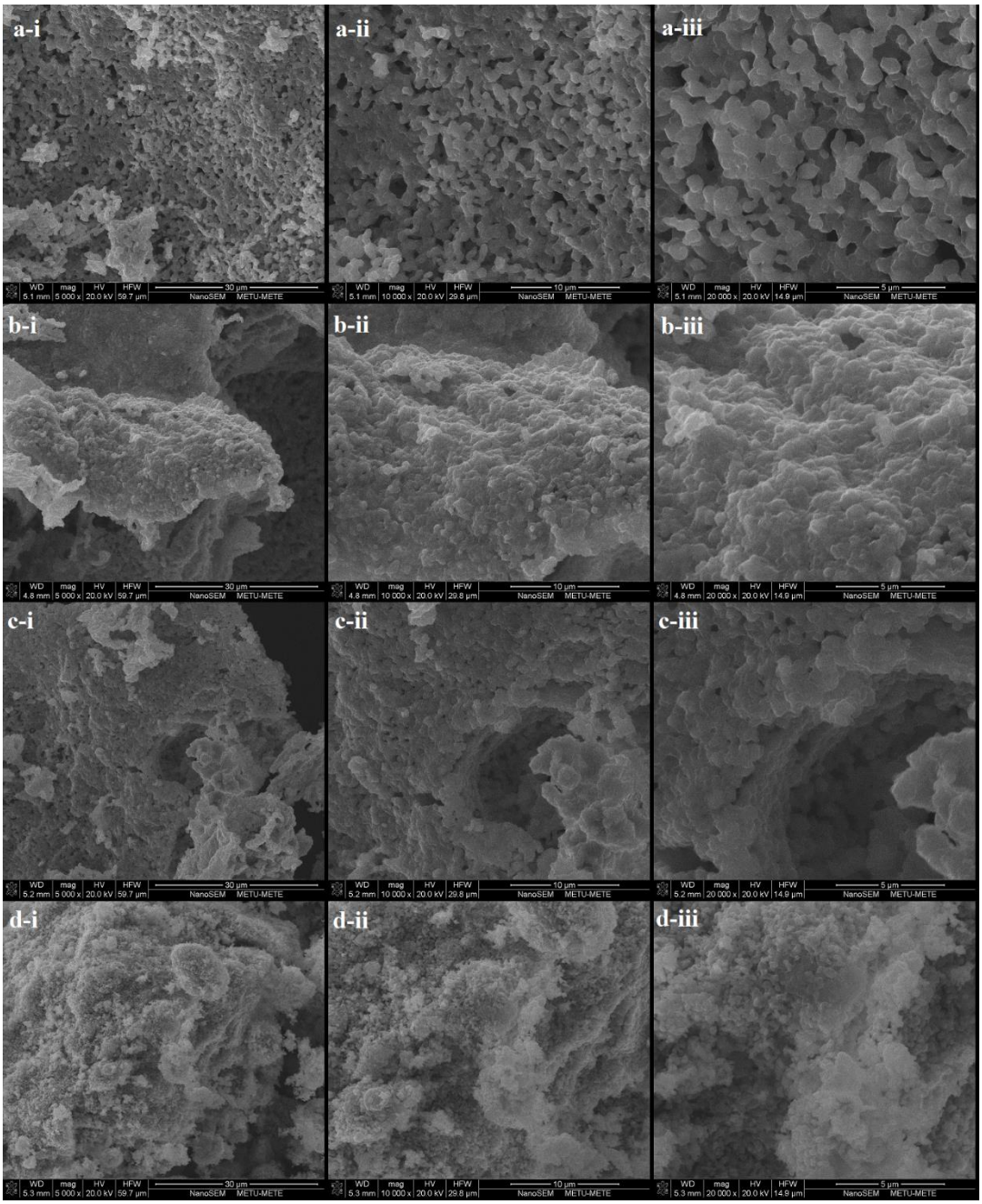


Figure 4.8. SEM images of pure a) $LiNi_{0.6}Mn_{0.2}Co_{0.2}O_2$, b) $LiNi_{0.7}Mn_{0.2}Co_{0.1}O_2$, c) $LiNi_{0.7}Mn_{0.1}Co_{0.2}O_2$, d) $LiNi_{0.8}Mn_{0.1}Co_{0.1}O_2$ ([i] 5000, [ii] 10000, and [iii] 20000 magnification for every type of powder).

It was observed that the particles formed in the materials synthesized by the sol-gel method were agglomerated (Figure 4.8). This is important as the spherical and

homogenous particles with the diameter of 10 μm directly affect the capacity and capacity retention of the samples as mentioned in the study of Longwei Liang in part 2.4. Therefore, the capacities and capacity retention values of the materials produced with sol-gel method were expected to be low according to materials produced with co-precipitation method.

The sol-gel method is a successful method to reduce the effect of cation mixing based on SEM photographs and XRD analysis. However, it is seen that the relevant method is not suitable for obtaining the desired particle morphology in the literature.

The samples obtained after the calcination of the same samples were characterized with ICP, SEM, EDS, and XRD methods. The chemical analysis of the obtained samples was carried out using ICP-OES and Energy Dispersive Spectroscopy (EDS). The EDS results of the candidates in terms of percent atomic ratio are provided in Table 4.17.

Table 4.17. EDS results of pure NMCs.

Sample	Ni%	Mn%	Co%
P622	60.08%	19.83%	20.09%
P721	70.04%	19.98%	9.98%
P712	70.10%	9.76%	20.14%
P811	79.91%	9.94%	10.15%

The results of the ICP are more precise than the EDS results. Looking at the results of the EDS and ICP provided in Tables 4.17 and 4.6, it is observed the molar ratios of nickel, manganese, and cobalt are close to each other. The ICP method is employed to determine trace amounts and main concentrations of all elements in the sample. On the other hand, the chemical composition of the particles seen at SEM in micro and nano sizes are identified with the EDS method.

Based on the close results, it would be appropriate to make an evaluation through the EDS results. In order to satisfy 1 mole of lithium in the samples (NMC 622, 712,

721, and 811), the experiment was carried out in the 5 % excess of lithium. As a result, the desired chemical compositions of the Ni-rich NMC materials were produced when looking at the results of the EDS and ICP.

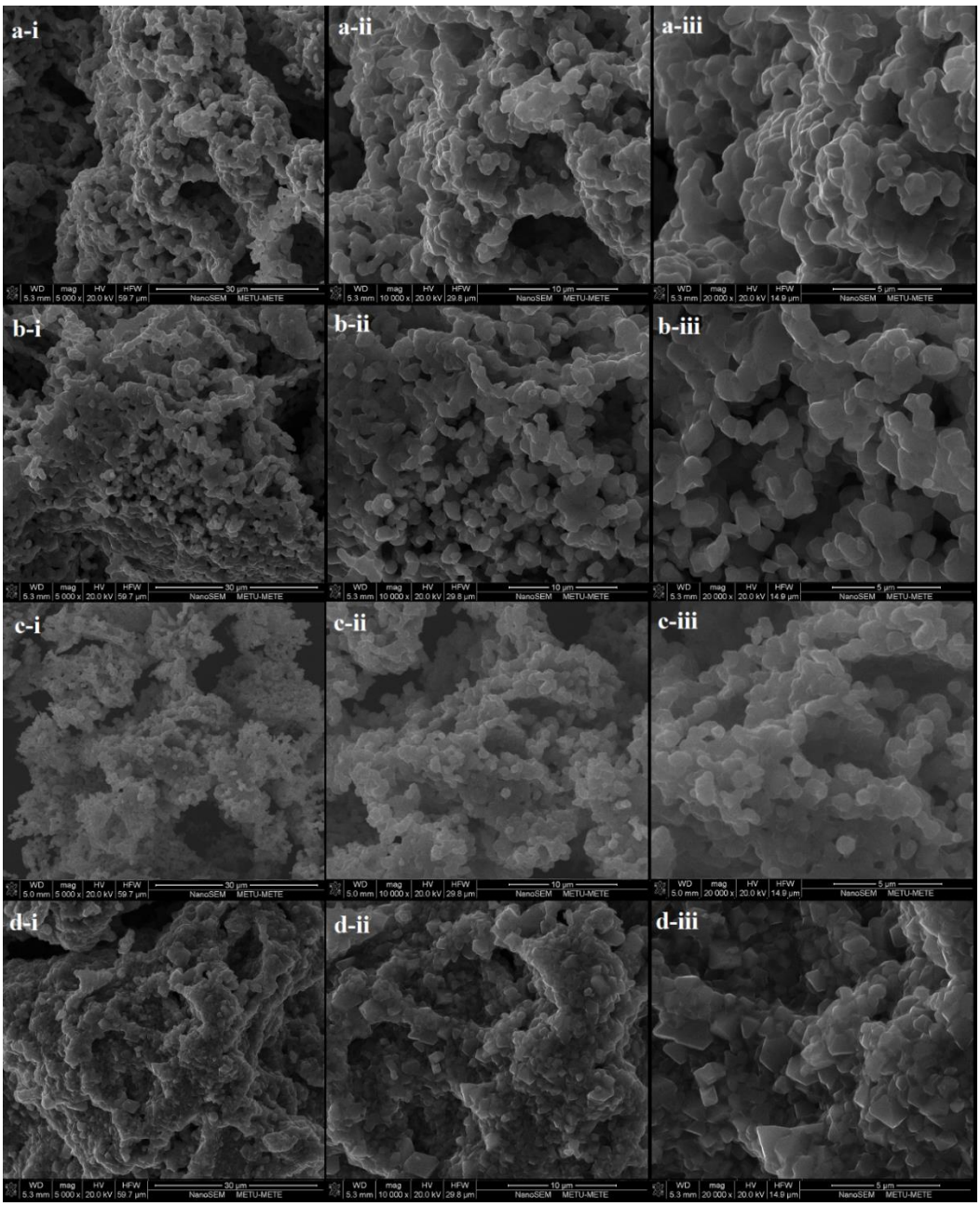


Figure 4.9. SEM images of 2% Nb containing a) $LiNi_{0.6}Mn_{0.2}Co_{0.2}O_2$, b) $LiNi_{0.7}Mn_{0.2}Co_{0.1}O_2$, c) $LiNi_{0.7}Mn_{0.1}Co_{0.2}O_2$, d) $LiNi_{0.8}Mn_{0.1}Co_{0.1}O_2$ ([i] 5000, [ii] 10000, and [iii] 20000 magnification for every type of powder).

The SEM images of the NMC materials (NMC 622, 721, 712, and 811) doped with 0.02 moles of niobium are provided in Figure 4.9. In the relevant images, any second phase formation is not observed. When Rietveld analyses performed on XRD results and SEM images are considered together, the Li_3NbO_4 phase seen in the XRD results might coat the NMC particles like in the literature instead of creating a separate phase.

Looking at the structure of the particles, instead of coming together to form spherical particles, it is seen that they agglomerate. The same was observed in pure-NMCs. Furthermore, the rough diagonals in the shape of the primary particles take attention. Although the particle sizes of the pure NMCs shortened with increasing Ni content, the particle size of the 2% Nb-doped NMCs did not change with the nickel ratio.

Table 4.18. EDS results of 2% Nb containing NMCs.

Sample	**Ni%**	**Mn%**	**Co%**	**Nb%**
D622	58.88%	19.83%	19.42%	1.87%
D721	68.64%	19.59%	9.69%	2.08%
D712	68.69%	9.81%	19.29%	2.21%
D811	78.31%	9.54%	9.97%	2.18%

EDS measurements were conducted at different points of the 2% Nb containing nickel rich NMC materials. Accordingly, it is seen that the mole of Nb is 2% at all the points. Additionally, the average of the related EDS measurements of the materials are provided in Table 4.18.

In Figure 4.10, the SEM images of the NMC622 samples a) in the pure form b) with 2% Nb doped c) with 4% Nb doped and d) with 8% Nb doped are provided. In the XRD results, it was observed that all the samples (NMC 622, 721, 712, and 811) doped with 4% and 8% Nb were not suitable for use. However, only SEM and EDS analyses of the NMC 622 samples doped with 4% and 8% Nb were carried out in order to make comparisons.

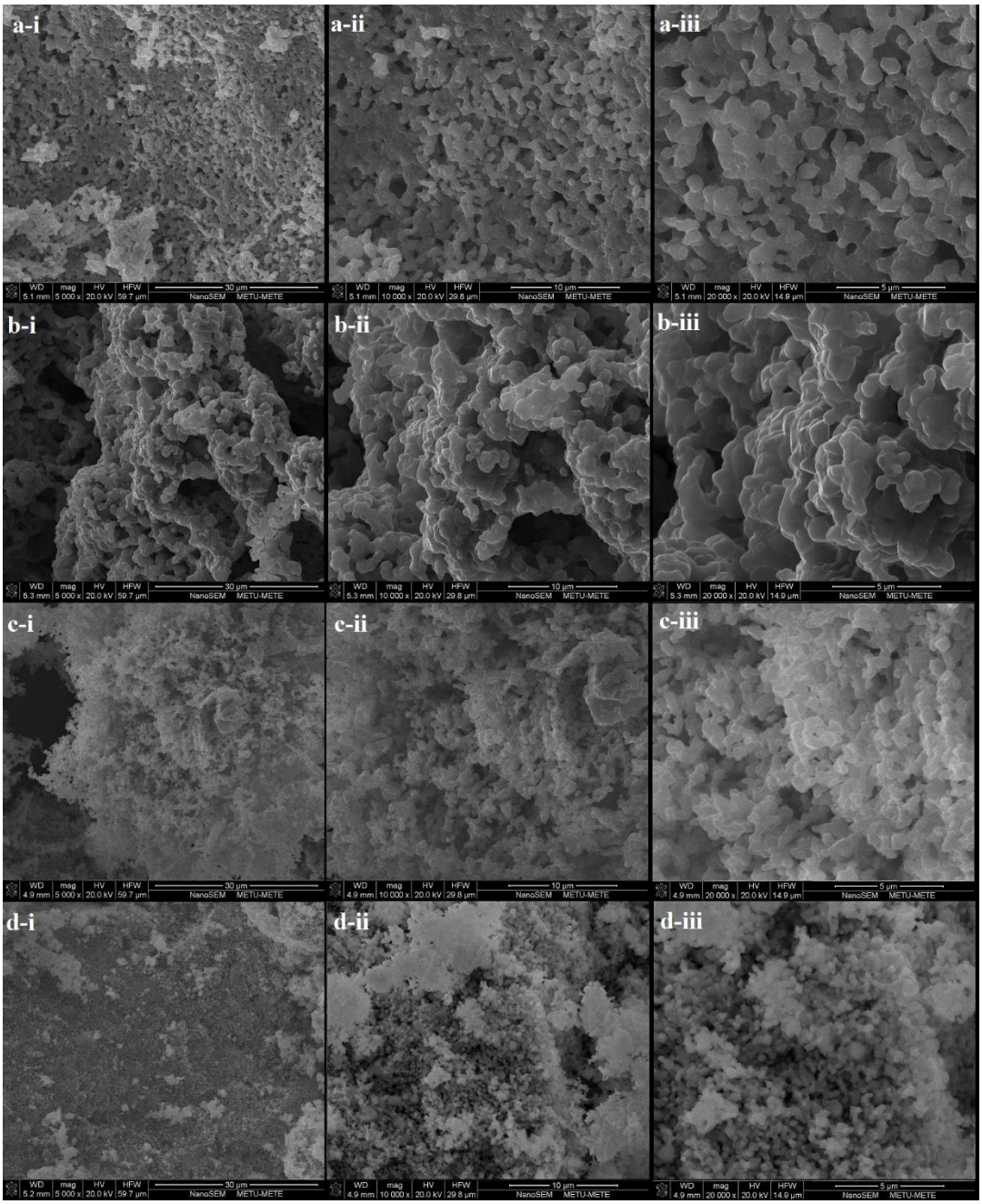


Figure 4.10. SEM images of the NMC622 samples a) in the pure form b) with 2% Nb containing c) with 4% Nb containing and d) with 8% Nb containing ([i] 5000, [ii] 10000, and [iii] 20000 magnification for every type of powder).

All the particle sizes of the NMC 622 candidates are similar. Additionally, the agglomeration due to the production with the sol-gel method is observed. There is

no second phase formation in the SEM images of the sample with 4% Nb doped as that of the 2% Nb-doped sample. As expected, the mole of Nb is 4% at all the locations according to the EDS measurements taken from the different particles. Although the second phase formation is not observed in the SEM results, it is known that 4% Nb doping increases the effect of cation-mixing as clearly seen from Table 4.12. On the other hand, there is a second phase formation in the sample doped with 8% Nb. The mole of Nb is 8% at some points and 20% at others according to the EDS measurements taken from the different points shown in Figure 4.11 are given in Table 4.19. When examining the XRD results in Table 4.14, it is seen that the structure of the NMC sample doped with 8% Nb is decomposed. EDS results prove this.

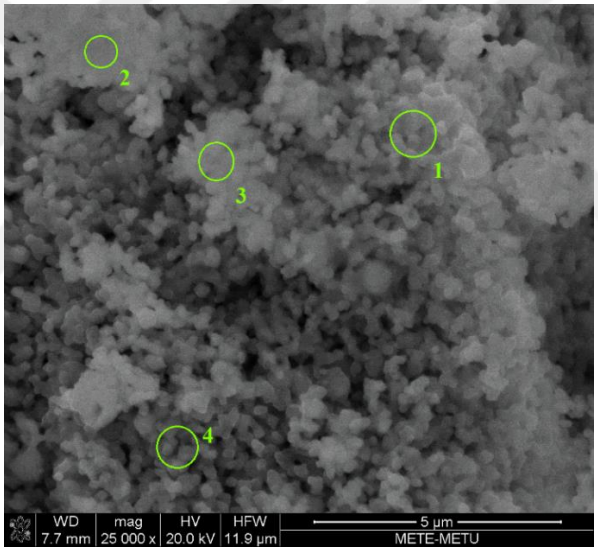


Figure 4.11. SEM images of 8% Nb containing NMC 622 from different points. The circles represent the points where the EDS data was collected.

Table 4.19. EDS results of 8% Nb containing NMC 622 from different points.

Point	Ni%	Mn%	Co%	Nb%
1	54.86%	17.73%	18.54%	8.87%
2	50.14%	14.84%	14.94%	20.08%
3	51.69%	15.41%	15.69%	17.21%
4	56.31%	18.54%	18.81%	6.34%

4.2 Electrochemical Tests

4.2.1 Capacity Test of Materials

The initial discharge curves of P622, P721, P712, and P811 are provided in Figure 4.12. It is seen clearly from the figure that the voltage plot of P811 is higher than the other samples. On the other hand, the voltage plots of P622, P721, and P712 are quite close to each other.

As it can be observed from Table 4.2, the discharge capacity of P712 is higher than that of P721, which is higher than that of P622.

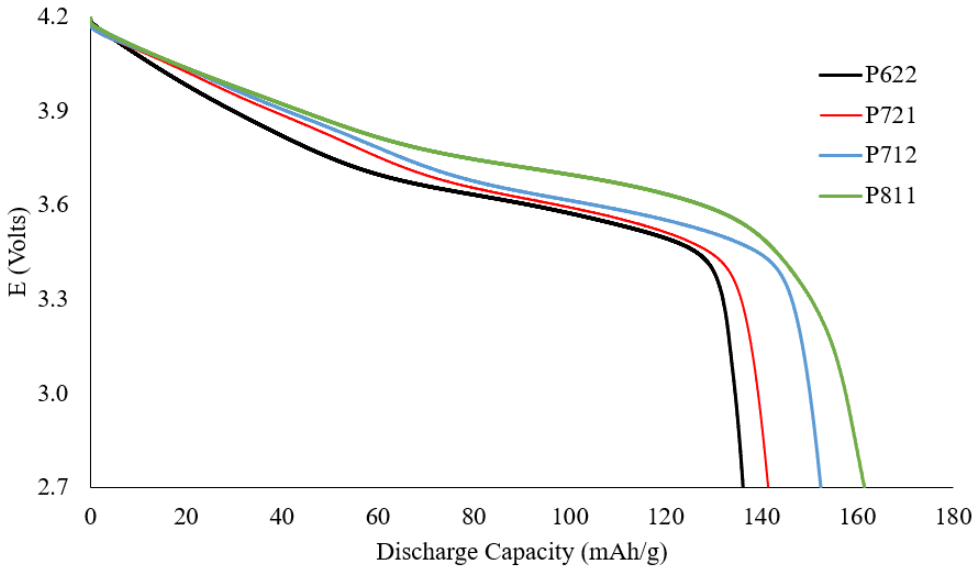


Figure 4.12. The initial discharge curves of P622, P721, P712, and P811 between 2.7 V - 4.2 V at 0.1 C.

In Figure 4.13, the discharge capacities of the P622, P712, P721, and P811 during 20 cycles at 0.1 C between 2.7 V and 4.2 V are indicated. In Table 4.9, the discharge capacities at the 1st and 20th cycle and capacity retention at the 20th cycle of the

relevant samples are provided. As expected, the first discharge capacity increases with the increasing nickel content. Although the nickel content of the P721 and P712 is the same, the discharge capacity of the P712 is higher than P721. Cobalt changes its valence state between 2.7 and 4.2 V, causing the capacity of P712 being higher because of its higher cobalt content. Moreover, manganese content does not affect the capacity because its valence state does not vary between 2.7 and 4.2 V.

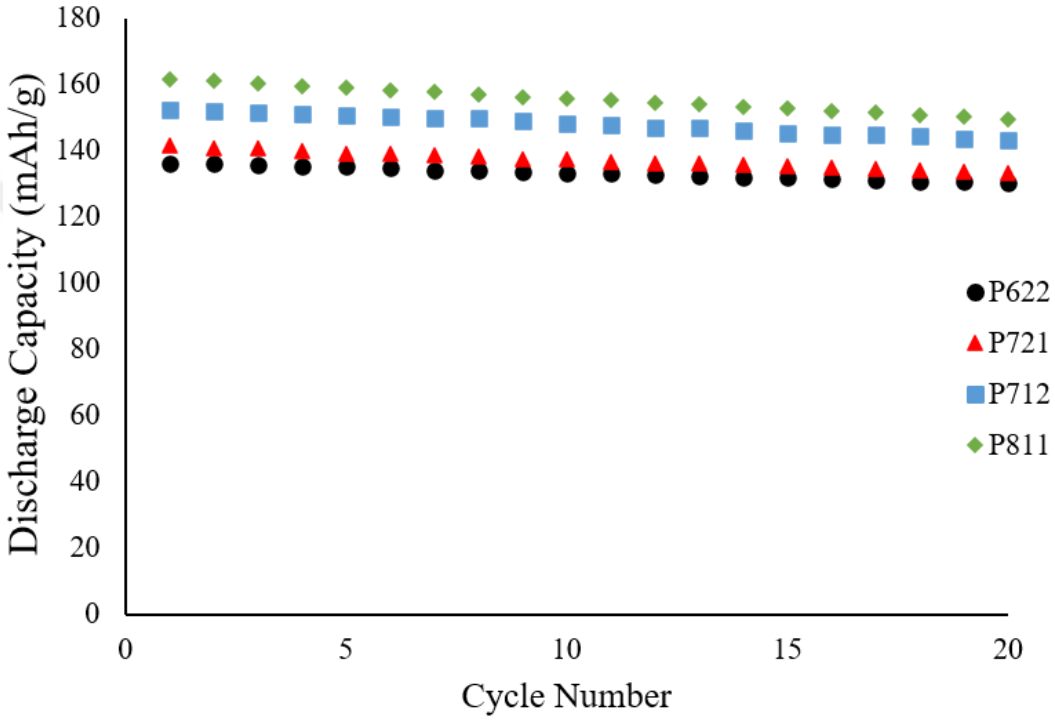


Figure 4.13. The discharge capacities of the P622, P721, P712, and P811 between 2.7 V - 4.2 V at 0.1 C.

When looking at Table 4.20, it is seen that the capacity retention reduces with the rising nickel amount. Although the nickel content of the P721 and P712 is the same, the P721 is more stable due to its higher manganese content.

Assuming that the discharge capacities of the P622, P721, P712, and P811 provided in Figure 4.12 continue to decrease linearly, the discharge capacity of P622 with the lowest initial discharge capacity will reach that of P811 with the highest one at the following cycles.

Table 4.20. First discharge, 20th discharge and capacity retention at 0.1 C of pure samples.

	P622	**P721**	**P712**	**P811**
First Discharge Capacity (mAh/g)	136.14	141.36	152.34	161.44
20. Discharge Capacity (mAh/g)	130.37	133.26	143.26	149.63
Capacity Retention	95.76%	94.26%	94.04%	92.69%

The specific discharge energies of P622, P721, P712, and P811 are given in Figure 4.14. While the specific discharge energies of P622, P721, and P712 are parallel to their discharge capacities, that of P811 is higher than the others as its voltage plot is high. Increasing nickel content in NMC samples results in a further increase in energy as well as an increase in capacity.

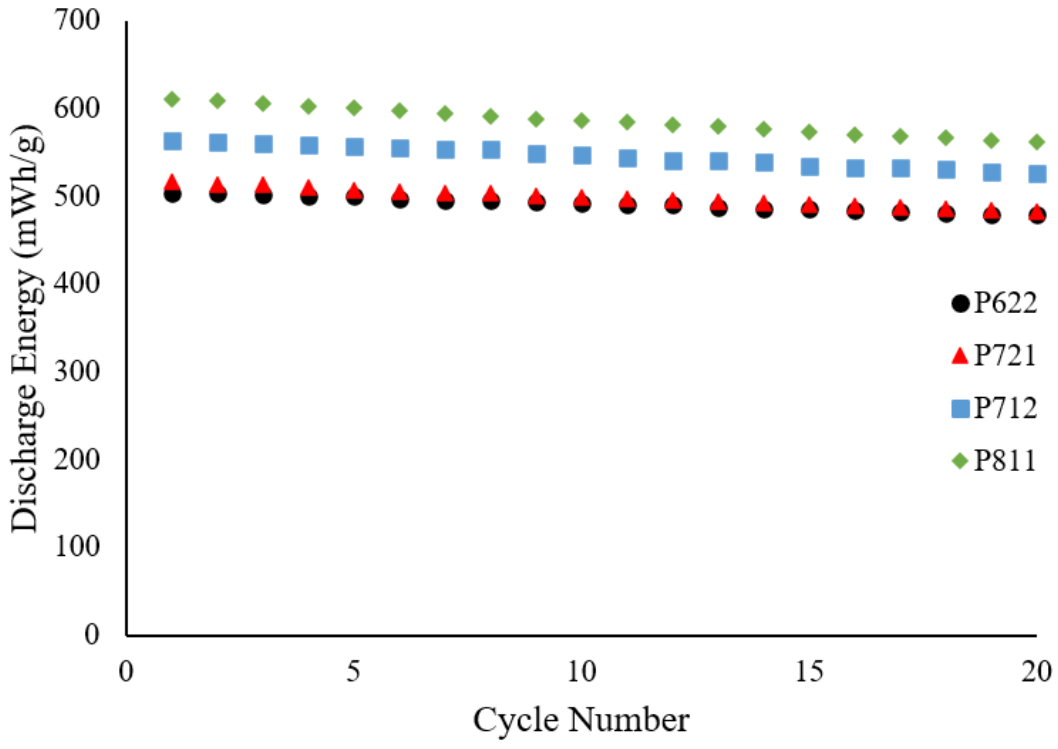


Figure 4.14. The discharge energies of the P622, P721, P712, and P811 between 2.7 V - 4.2 V at 0.1 C.

Looking at the initial discharge curves of D622, D721, D712, and D811, their voltage plots are quite close to each other, unlike the pure materials. In Figure 4.16, the initial discharge curves of doped materials are compared to that of their corresponding pure materials. Since their nickel, manganese, and cobalt ratios are the same, the discharge plots of the doped samples are similar to those of the corresponding pure materials. In the relevant figure, the capacity that cannot be used due to the niobium doping manifests itself clearly. Unlike the other samples, the voltage plot of D811 is below that of P811. The reason for this may be because of niobium as well as properties such as particle size and material resistance.

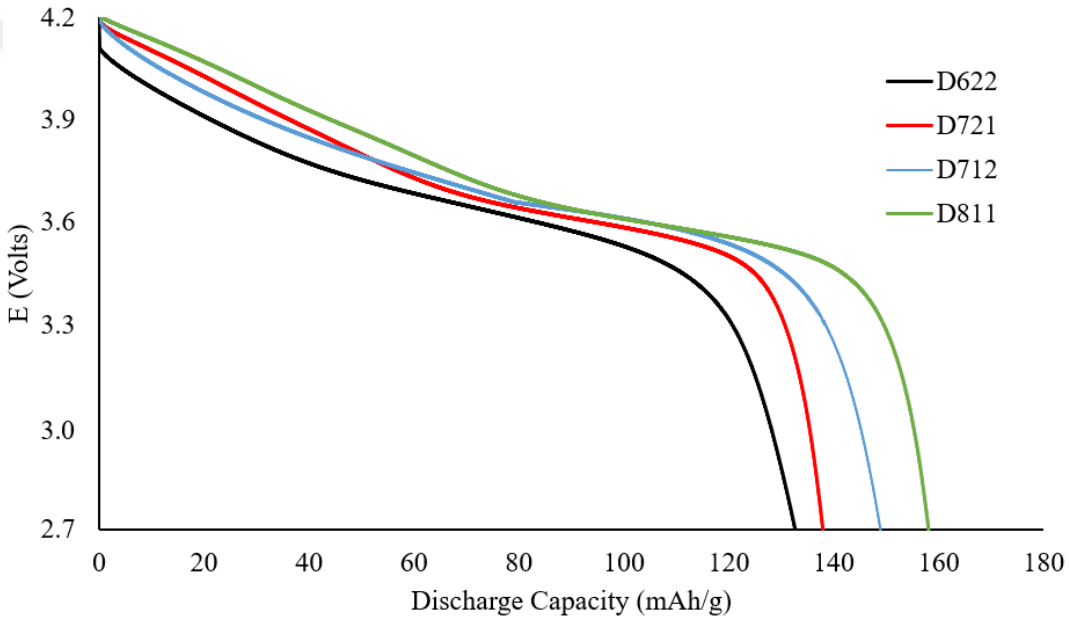


Figure 4.15. The initial discharge curves of D622, D721, D712, and D811 between 2.7 V - 4.2 V at 0.1 C.

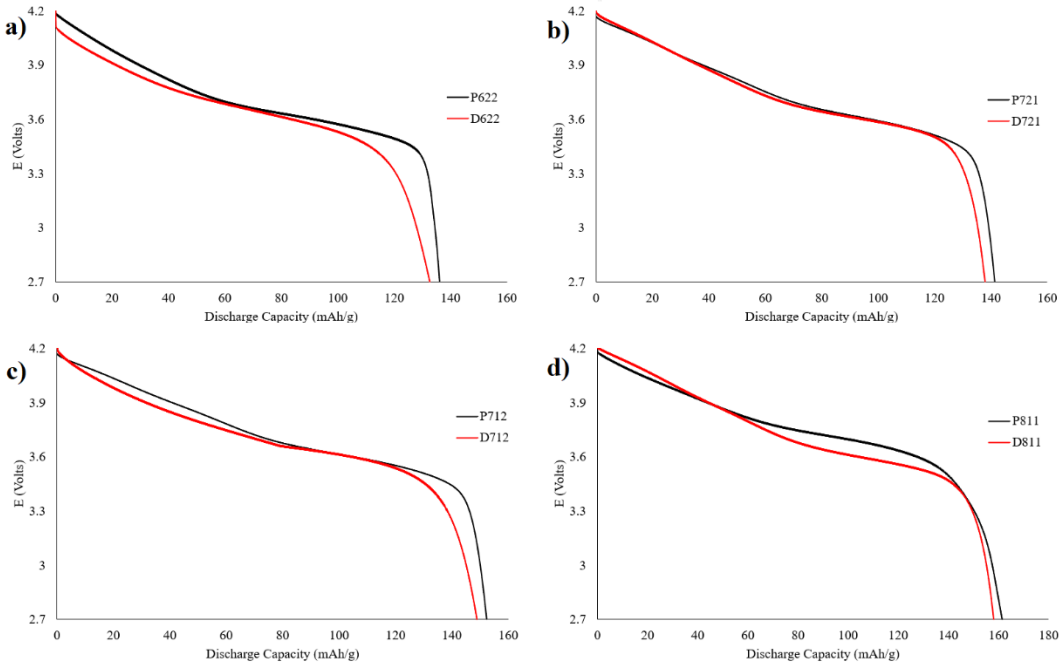


Figure 4.16. The initial discharge voltage curves of a) P622 and D622, b) P721 and D721, c) P712 and D712, and d) P811 and D811 at 0.1C.

In Table 4.21, the discharge capacities at the 1st and 20th cycle and capacity retention at the 20th cycle of the samples containing 2% Nb are provided. As expected, the initial discharge capacity is directly proportional to the nickel ratio. Compared to Table 4.20, the initial capacity values of all doped samples are lower than pure samples. The reason for this is that niobium does not contribute to the capacity by not changing valency during charge and discharge. Furthermore, as expected, capacity retentions of all doped samples are decreasing with increasing nickel ratio. When the capacity retentions are compared between Table 4.20 and Table 4.21, it is seen that the capacity retention of doped materials is higher for each composition.

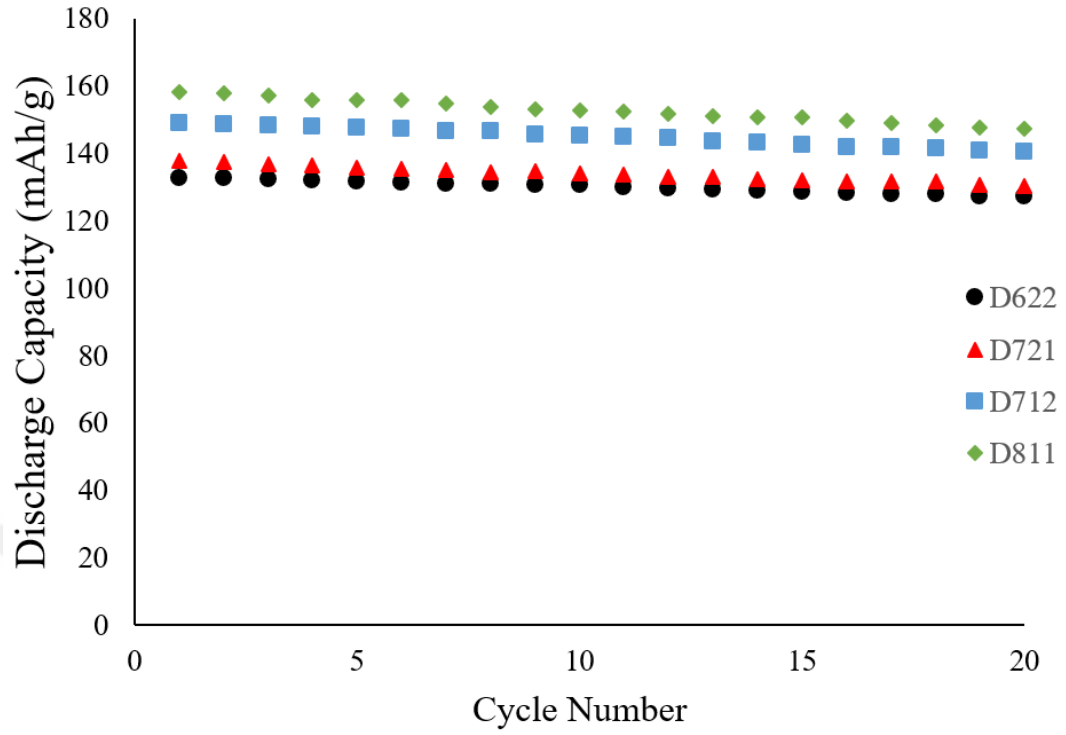


Figure 4.17. The discharge capacities of the D622, D721, D712, and D811 between 2.7 V - 4.2 V at 0.1 C.

Although the amount of niobium doped to the materials is the same, it was observed from Table 4.11 in Part 4.1.2 that more niobium ions were incorporated into the structure with the increasing nickel content in the materials. When comparing the capacity retention of pure and doped samples in Tables 4.20 and 4.21, it was seen that the capacity retention increased more with increasing nickel content. In other words, as the niobium in the structure increased, the capacity retention increased more.

Table 4.21. First discharge, 20th discharge and capacity retention at 0.1 C of 2% Nb containing samples.

	D622	**D721**	**D712**	**D811**
First Discharge Capacity (mAh/g)	132.67	137.92	148.92	158.07
20. Discharge Capacity (mAh/g)	127.32	130.38	140.42	147.20
Capacity Retention	95.97%	94.53%	94.29%	93.13%

In Figure 4.18, the discharge capacities of D622, D721, D712, D811 and that of corresponding pure samples are compared with respect to cycle number. If the discharge capacities of D622, D721, D712, D811 and that of corresponding pure samples continue to decrease linearly, the discharge capacity of doped samples with the lower initial discharge capacity will reach that of corresponding pure samples with the higher one at the following cycles.

As can be seen in Figure 4.20, when the discharge energies of pure materials are compared with the discharge energies of Nb-doped materials, it has been observed that pure materials have higher discharge energy. Although Nb doping increases the capacity retention, it does not contribute to the discharge energy.

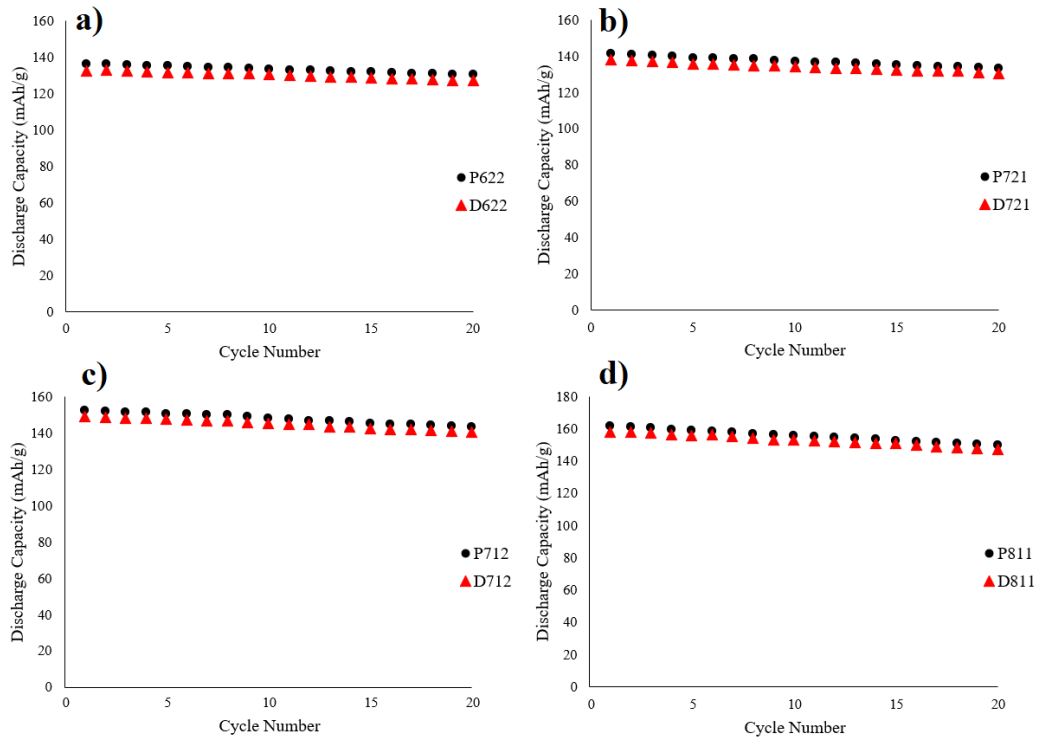


Figure 4.18. The discharge capacities of a) P622 and D622, b) P721 and D721, c) P712 and D712, and d) P811 and D811 between 2.7 V – 4.2 V at 0.1 C.

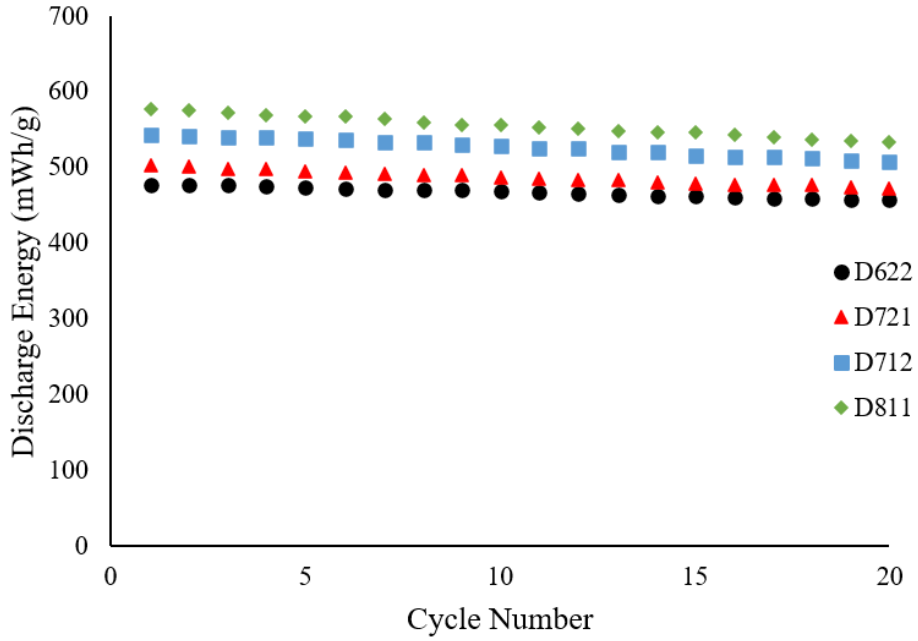


Figure 4.19. The discharge energies of the D622, D721, D712, and D811 between 2.7 V - 4.2 V at 0.1 C.

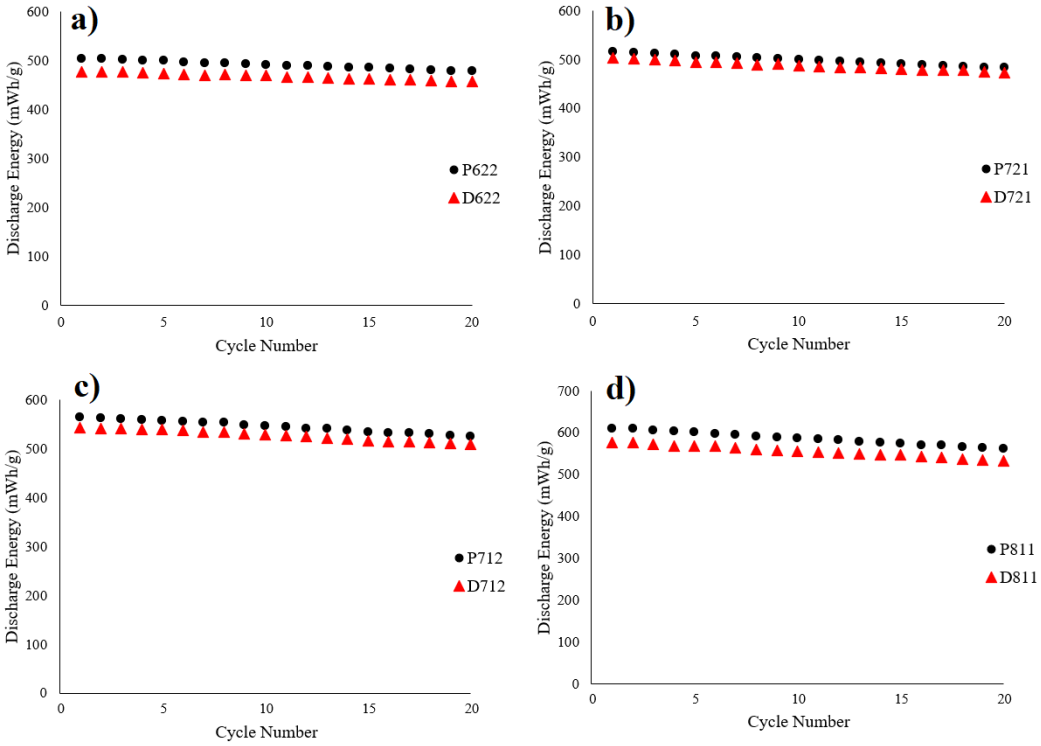


Figure 4.20. The discharge energies of a) P622 and D622, b) P721 and D721, c) P712 and D712, and d) P811 and D811 between 2.7 V – 4.2 V at 0.1 C.

4.2.2 Impedance Test of Samples

To understand the effects of charging-discharging between 2.7 V and 4.2 V at 0.1 C for 20 cycles on the P622, P721, P712, and P811 samples, the impedance analysis was performed before and after 20 cycles. The impedance analysis results a) before and b) after 20 cycles are shown in Figure 4.21. The electrolyte resistances (R_{el}), surface film resistances (R_f), and charge transfer resistances (R_{ct}) of all the samples are provided in Table 4.22.

As it can be seen, the electrolyte resistances (R_{el}) of all the samples are between 1.2 Ω and 2.6 Ω. The lowest surface film resistance (R_f) before charging-discharging belongs to P811. After charging-discharging, the surface film resistances of all the samples except for P721 increase. When compared to the surface film resistances of the samples before and after charging-discharging, it is seen that the highest increase

in the surface film resistance belongs to P811 with the highest Ni content. P811 with high nickel content has low-capacity retention rate as it loses Lithium ions in its structure during charge-discharge.

Looking the charge transfer resistances (R_{ct}) of the samples before the charge-discharge, they are quite close to each other except for that of P721. The charge transfer resistances (R_{ct}) of P622 and P811 after charge-discharge are quite close to each other, while that of P712 is 10% higher than them. Moreover, the R_{ct} of P721 is considerably higher than that of P622, P712, and P811. The charge transfer resistance of P811 increases less than that of P622. The separation of more Lithium-ions from the structure of P811 causes the structure resistance to increase less.

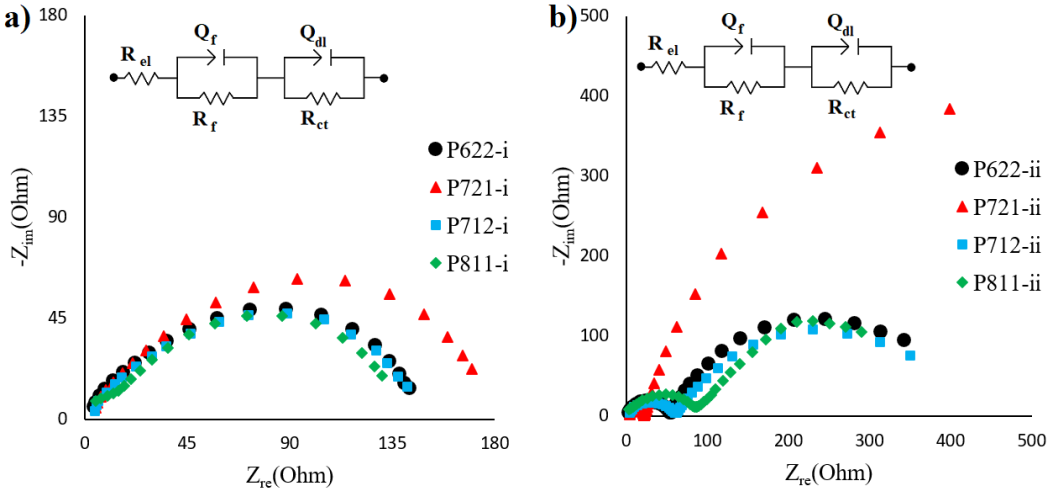


Figure 4.21. Nyquist plots of P622, P721, P712, and P811 samples a) before and b) after 20 cycles at 0.1C.

As indicated by the results in Table 4.20, the capacity retention reduces with the increase in the Ni amount. The rising nickel content also gives rise to increase in the surface film resistance (R_f). It can be concluded that as the nickel ratio increases, the increase in R_f on the surface contributes to the decrease in capacity retention.

Table 4.22. Resistance values of P622, P721, P712, and P811 samples i) before and ii) after 0.1 C at 20 cycle.

	i			ii		
	R_{el} (Ω)	**R_f (Ω)**	**R_{ct} (Ω)**	**R_{el} (Ω)**	**R_f (Ω)**	**R_{ct} (Ω)**
P622	1.43	29.1	153.1	1.45	53.4	370.1
P721	1.75	32.0	190.9	1.74	21.6	965.4
P712	1.21	36.7	154.2	2.53	61.6	410.3
P811	1.74	11.7	152.9	1.53	92.3	362.1

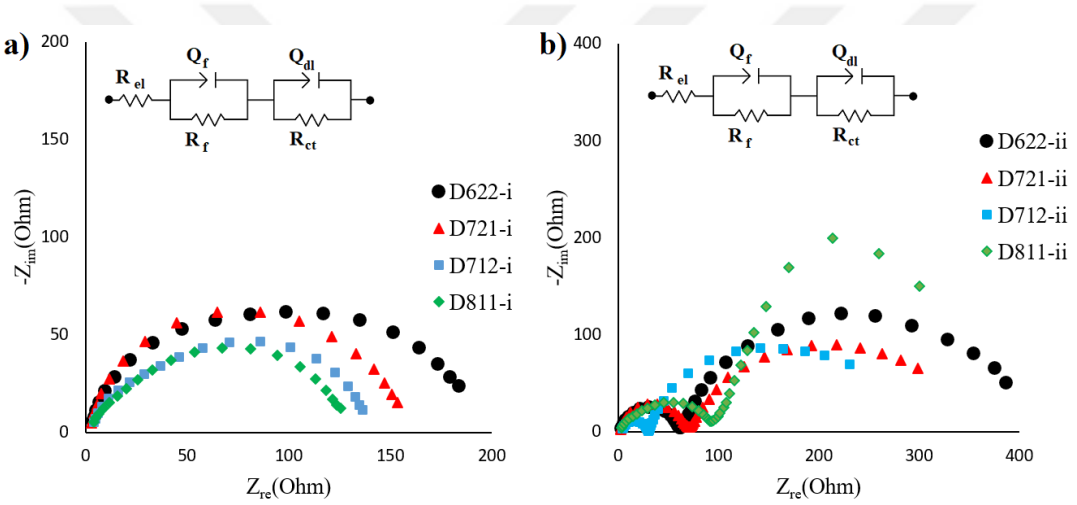


Figure 4.22. Nyquist plots of D622, D721, D712, and D811 samples a) before and b) after 0.1 C at 20 cycle.

The electrolyte resistances (R_{el}), surface film resistances (R_f), and charge transfer resistances (R_{ct}) of D622, D721, D712, and D811 samples are provided in Table 4.23. When looking at Table 4.23, it is observed that the surface film resistances (R_f) of all the candidates except for D712 increase. The highest increase in the surface film resistance belongs to D811 like in the undoped material. The charge transfer resistances (R_{ct}) of the samples before charge-discharge reduces with the increasing nickel content. Looking at the charge transfer resistances (R_{ct}) of the samples at the end of the 20 cycles, it is seen that D622 has the highest and D811 has the lowest

values. Compared to the values in Table 2.24, the charge transfer resistances (R_{ct}) of the Nb-doped samples are lower than the corresponding compositions in pure materials. This explains the slight improvement in capacity retention.

Table 4.23. Resistance values of D622, D721, D712, and D811 samples i) before and ii) after 0.1 C at 20 cycle.

	i			ii		
	R_{el} (Ω)	**R_f (Ω)**	**R_{ct} (Ω)**	**R_{el} (Ω)**	**R_f (Ω)**	**R_{ct} (Ω)**
D622	1.04	29.3	189.4	1.67	60.2	360.1
D721	1.73	10.4	155.3	2.41	64.4	312.8
D712	2.13	43.3	144.7	1.41	32.2	311.1
D811	1.82	46.1	129.7	1.30	97.1	306.5

4.2.3 Rate Capability Test of Samples

The discharge capacities of the P622, P721, P712, and P811 samples as a result of sequential charge-discharge for 2 cycles at 0.1 C, for 15 cycles at 0.3 C, for 15 cycles at 1 C, and for 2 cycles at 0.1 C between 2.7 and 4.2 Volts are provided in Figure 4.24. The samples are charged-discharged 2 times at 0.1 C before charging-discharging at the high currents. After charging-discharging at the high currents, the samples are charged-discharged 2 times at 0.1 C again in order to observe their capacity performances.

Figure 4.23 shows the initial discharge voltage curves of P622, P721, P712, and P811 at 0.3 C and at 1 C after 15 cycles at 0.3 C. From the pertaining figure, it is seen that the initial discharge voltage curves of P622, P721, P712, and P811 at 0.3 C are similar. On the other hand, those of P622, P721, P712, and P811 at 1 C are not alike. Also, the initial discharge of all samples starts well below 4.2 V. Although the voltage plot of P721 is above that of P622, it gives the same capacity with P622. This

is because P721 is more affected than P622 by 15 cycles at 0.3 C. P721 shows a voltage plot similar to that of P712, while the highest voltage pilot belongs to P811.

It was observed that the initial discharge voltage curves of the samples at 1 C were below that of the initial discharge voltage curves at 0.1 C and 0.3 C. Also, the initial discharge capacities of the samples at 1 C were lower than the initial discharge capacities at 0.1 C and 0.3 C. These were due to the transport losses in the solid and electrolyte phases of the electrode at high discharge current rates.

As mentioned above, the samples were charged-discharged at 0.3 C for 15 cycles before charging-discharging at 1 C. It was assumed that the surface film and charge transfer resistances of the samples increased similar to the experiment results provided in Table 4.2.1 in Part 4.2.2. Likewise, based on the same table, it was assumed that the increase in their resistance after 15 cycles at 0.3 C decreased with increasing nickel content.

Therefore, increasing nickel content enables to obtain of more stable initial discharge voltage curves at a high current (1 C) as seen in Figure 4.23.

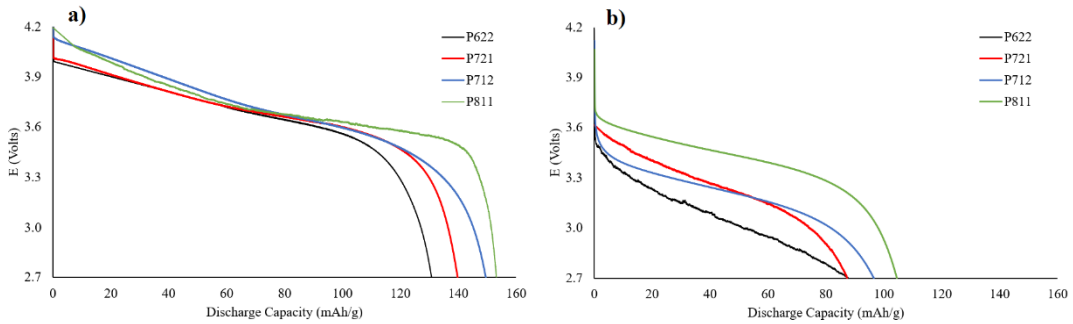


Figure 4.23. The initial discharge voltage curves of P622, P721, P712, and P811 at a) 0.3 C, and b) 1 C.

In Table 4.24, the average obtained discharge capacities of the samples at 0.1 C before and after charging-discharging at the high currents are provided. Additionally, the 1st and 15th cycles obtained discharge capacities of the samples at 0.3 C and 1 C, and corresponding capacity retentions are indicated.

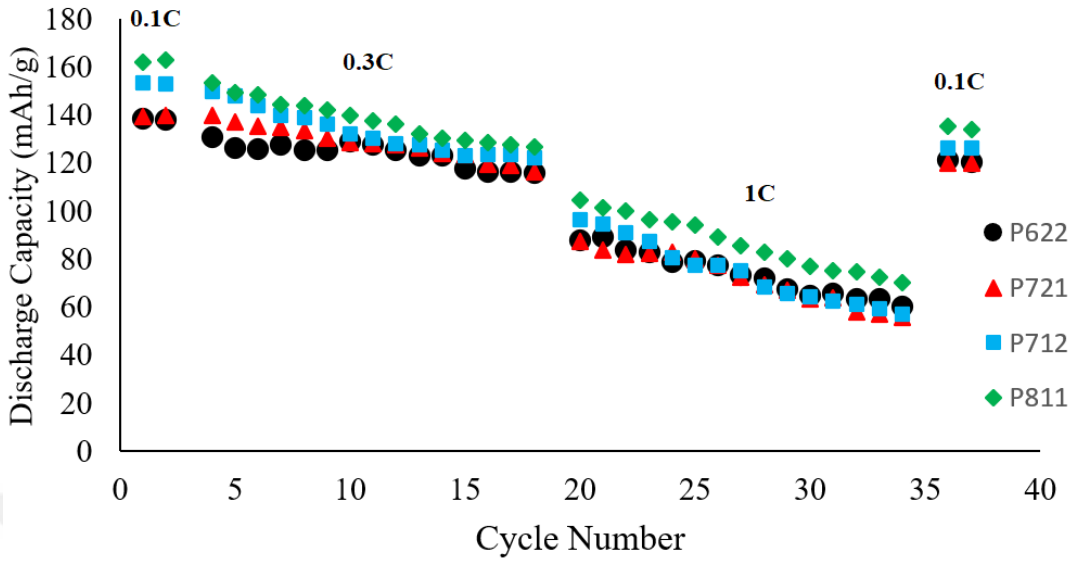


Figure 4.24. The discharge capacity graph of the P622, P721, P712, and P811 between 2.7 V - 4.2 V at 0.1 C, 0.3 C, 1 C, and 0.1 C.

The obtained capacity retentions of all the samples at 0.3 C reduce with the increasing nickel content. It is deduced that the samples show the same properties when they are charged-discharged at 0.3 C as at 0.1 C (Table 4.20).

When the obtained capacity retentions of all the samples at 1 C are examined, it is seen that the highest capacity retention belongs to P622. According to the literature, the electrochemical conductivity must increase with the rising nickel amount. As expected, the obtained capacity retention of P811 at the higher currents is higher than P712 and P721. However, it is lower than that of P622.

When compared to the average obtained discharge capacities of the samples at 0.1 C before and after charging-discharging at the high currents, the lowest change in the capacity belongs to P622. Although the P811 performance at 1 C, it is seen that P811 has the highest drop in capacity. Moreover, P721 is more stable than P712 and P811 because of its higher manganese content.

P811 shows the highest discharge energy at 1C as it has a high discharge curve besides its stability at high discharge rates.

Table 4.24. The discharge capacities of the P622, P721, P712, and P811 between 2.7 V - 4.2 V at 0.1 C, 0.3 C, 1 C, and 0.1 C.

		P622	P721	P712	P811
0.1 C	Average Discharge Capacity (mAh/g)	138.09	139.56	153.05	162.37
0.3 C	First Discharge Capacity (mAh/g)	130.78	139.80	149.50	153.16
	15. Discharge Capacity (mAh/g)	115.61	116.36	121.91	126.72
	Capacity Retention	88.40%	83.24%	81.55%	82.74%
1 C	First Discharge Capacity (mAh/g)	87.64	87.39	96.53	104.51
	15. Discharge Capacity (mAh/g)	60.15	55.75	56.95	69.99
	Capacity Retention	68.63%	63.79%	59.00%	66.97%
0.1 C	Average Discharge Capacity (mAh/g)	120.71	119.80	127.29	134.52
	Change Between 0.1 C's	87.41%	85.84%	83.17%	82.84%

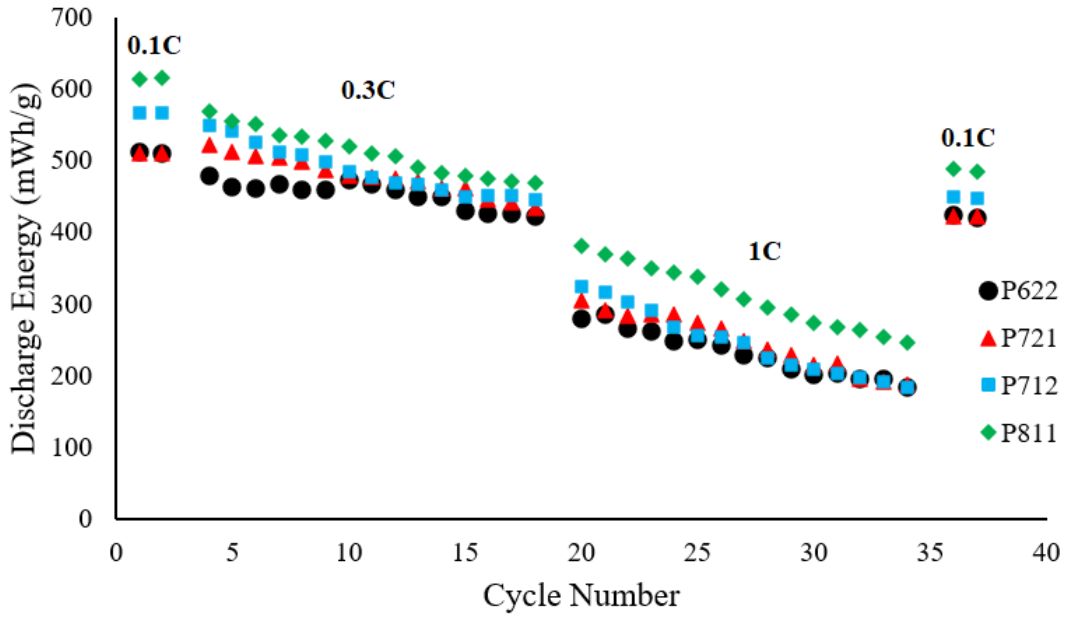


Figure 4.25. The discharge energy graph of the P622, P721, P712, and P811 between 2.7 V - 4.2 V at 0.1 C, 0.3 C, 1 C, and 0.1 C.

The discharge capacities of the D622, D721, D712, and D811 samples as a result of sequential charge-discharge for 2 cycles at 0.1 C, for 15 cycles at 0.3 C, for 15 cycles

at 1 C, and for 2 cycles at 0.1 C between 2.7 and 4.2 Volts are provided in Figure 4.27. The average discharge capacities of the doped samples at 0.1 C both before and after charging-discharging at high currents are shown in the table below. Additionally, the 1st and 15th cycle obtained discharge capacities of the samples at 0.3 C, 1 C and corresponding capacity retentions are indicated.

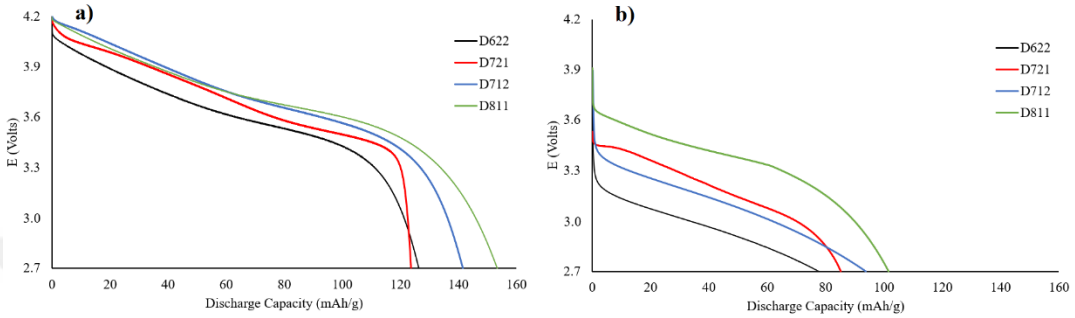


Figure 4.26. The initial discharge voltage curves of D622, D721, D712, and D811 at a) 0.3 C, and b) 1 C.

Looking at the capacity retention of the samples at 0.3 C, the capacity retention of the materials except for D721 reduces with the increasing nickel content. However, it is not correct to make a precise interpretation since the values are so close. Compared to others, the D721's capacity retention appears to be higher than expected. When compared with Table 4.24, at 0.3 C, P622 showed higher capacity retention than D622, while D721 showed higher capacity retention than P721. There is no considerable difference between the capacity retention of D712 and P712 and between D811 and P811.

The capacity retentions of the samples in Table 4.25 at 1C show higher capacity retentions with D721 and D712 than with P721 and P712 when compared with Table 4.24 after 15 cycles. Additionally, even though the first discharge capacity of D712 at 1 C is lower than P712, looking at the 15th cycle, it is seen that its discharge capacities are higher than that of P712. The capacity retention of D622 is lower than that of P622 as opposed to expected. When looking at the discharge capacities of D811 and P811, it is seen that D811 shows the same performance as P811.

Consequently, the desired effect could not be obtained at 1C charge-discharge rate in D622 and D811 samples.

When looking at the performances of all the samples doped with 2% Nb at 0.1 C after charging-discharging at 0.3 C for 15 cycles and at 1C for 15 cycles, all the Nb-doped NMC materials show a higher performance than the undoped material. This demonstrates that although Nb does not show a considerable performance at high currents, it protects the structure and reduces the capacity losses when reverting from the higher charging-discharging rates to the lower ones.

Looking at the discharge energies at 0.3 C and 1 C, the discharge energies of doped materials are lower than pure materials, as at 0.1 C. So, the niobium doping does not have a dominant effect on discharge energies at high charging rates.

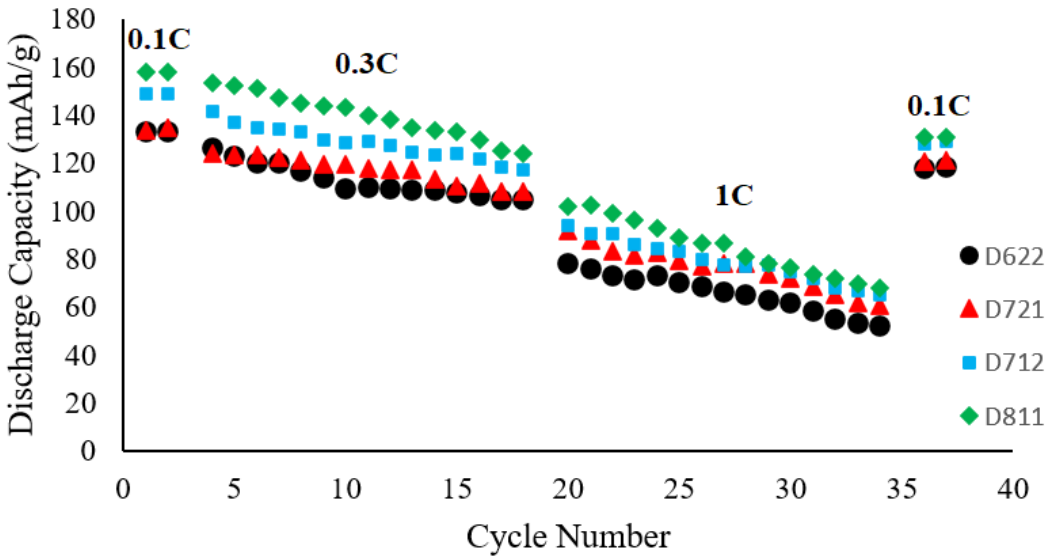


Figure 4.27. The discharge capacity graph of the D622, D721, D712, and D811 between 2.7 V - 4.2 V at 0.1 C, 0.3 C, 1 C, and 0.1 C.

Table 4.25. The discharge capacities of the D622, D721, D712, and D811 between 2.7 V - 4.2 V at 0.1 C, 0.3 C, 1 C, and 0.1 C.

		D622	D721	D712	D811
0.1 C	Average Discharge Capacity (mAh/g)	132.70	133.88	148.57	157.77
0.3 C	First Discharge Capacity (mAh/g)	126.35	123.65	141.57	153.40
	15. Discharge Capacity (mAh/g)	104.68	107.85	117.08	123.86
	Capacity Retention	82.84%	87.22%	82.70%	80.75%
1 C	First Discharge Capacity (mAh/g)	77.80	91.69	93.78	101.58
	15. Discharge Capacity (mAh/g)	52.01	60.65	65.17	67.61
	Capacity Retention	66.85%	66.14%	69.49%	66.56%
0.1 C	Average Discharge Capacity (mAh/g)	117.87	119.85	128.39	131.22
	Change Between 0.1 C's	88.83%	89.53%	86.42%	83.18%

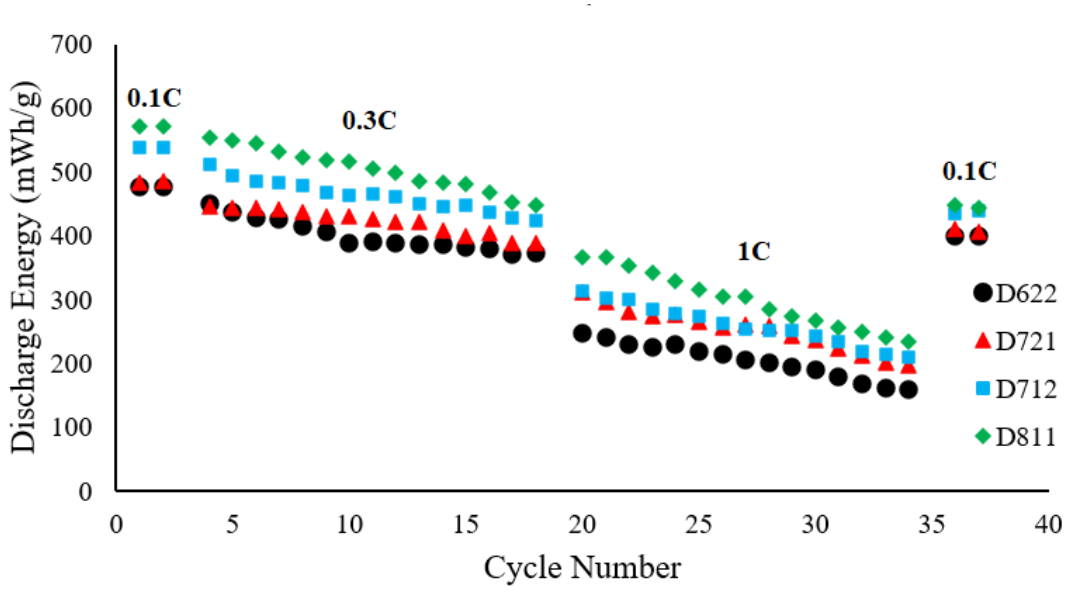


Figure 4.28. The discharge energy graph of the D622, D721, D712, and D811 between 2.7 V - 4.2 V at 0.1 C, 0.3 C, 1 C, and 0.1 C.

CHAPTER 5

CONCLUSION

The results of this study demonstrate that pure and niobium (Nb) doped materials with compositions 622, 721, 712 and 811 are perfectly produced using citric acid assisted Pechini modified sol-gel method. All pure samples have high $I_{(003)}/I_{(104)}$ ratio and good layered crystal structure. All samples were obtained with the requested stoichiometric ratios. When looking at the SEM images, it was observed that the materials have an agglomerated shape, which is far from the desired spherical and homogeneous shape in the literature. As a result, it turns out that the sol-gel method is not a suitable production method for the morphology of NMC cathode particles.

In electrochemical tests, as the nickel ratio in the structure increased, the capacity increased, but the capacity retention decreased. Looking at discharge energies, it was seen that they increased with increasing nickel content, similar to the capacities.

Examining the Nb doped NMC materials, it was observed from XRD results that not all niobium ions were incorporated into the structure, and some of them formed the Li_3NbO_4 phase. Li_3NbO_4 phase was formed too much in 4% and 8% Nb doped materials and the NMC structure deteriorated, leaving the $I_{(003)}/I_{(104)}$ ratio well below the desired value (1.2). For this reason, studies were continued with 2% Nb doped materials. 2% Nb doped samples demonstrated good $I_{(003)}/I_{(104)}$ ratio and good layered crystal structure. The resulting Li_3NbO_4 phase constituted 0.88% weight of 2% Nb-doped D622 and 0.57% weight of 2% Nb-doped D811. According to the results, it was concluded that with the increasing nickel content in NMC materials, more Nb ions were incorporated into the structure.

Moreover, it was seen that the initial discharge capacities of doped materials were lower than that of corresponding pure materials at 0.1 C due to niobium. However,

it was observed that the capacity retention of doped materials was higher than that of corresponding pure materials thanks to niobium. When the capacity retention change of doped materials was compared to pure ones, it was seen that D622 had the lowest difference and D811 had the highest one. This was because, with increasing nickel content, more Nb ions were incorporated into the structure, resulting in a further increase in capacity retention.

Looking at the discharge voltage plots of pure materials at 0.1 C, it is seen that the NMC material in the 811 composition is higher than the others. Thus, the discharge energy of the P811 sample was higher compared to the discharge capacities. There is no difference between the voltage plots of the different compositions of doped materials at 0.1 C. They are slightly below the voltage plots of pure materials. Therefore, when the discharge energies are compared, doped materials have a lower value.

It was seen clearly in the impedance tests carried out before and after charging-discharging at 0.1 C for 20 cycles that R_f and R_{ct} values of both doped and un-doped samples increased. The film layer on the surface of the samples thickened during charging-discharging. In addition, the discharge transfer resistance of the samples increased because their structure changed. This increase in charge transfer decreased slightly as the nickel ratio increased in pure materials, while it decreased more as the nickel ratio increased in 2% Nb-doped materials. It can be understood from here that as the nickel ratio in NMC increases, niobium enters the structure more and stabilizes the structure.

When the rate capabilities are evaluated for pure materials, the discharge voltage plots, discharge capacities, discharge capacity retentions and discharge energies in the tests performed at 0.3 C are similar to those performed at 0.1 C. When the discharge capacities at 1 C are examined, it is seen that NMC in composition 811 exhibits as much capacity conservation as composition 622. With the increasing nickel content, the electrochemical conductivity and the capacitance conservation increased at high discharge rates. The doped candidates charged-discharged at 0.3 C

demonstrated a parallel approach to the ones charged-discharged at 0.1 C in terms of the discharge capacity and capacity retention. Although the discharge capacities of the doped samples charged-discharged at 1 C increased with the increasing nickel content, there was no difference in their capacity retention. Considering the discharge voltage plots of pure and doped materials at 1 C, the discharge voltage plots decreased significantly as the nickel ratio decreased. Accordingly, the discharge energies showed the highest value in the material with high nickel content.

To sum up, Nb doped materials show higher capacity conservation at low discharge rates compared to pure materials, although initially they show a decrease in capacity. This study showed that Nb doping is greatly useful to improve the stability of the crystal structure and the electrochemical properties of the nickel rich NMC cathode materials.

REFERENCES

1. Warner JT. *The Handbook of Lithium-Ion Battery Pack Design: Chemistry, Components*. Elsevier; 2015.
2. Manthiram A. A reflection on lithium-ion battery cathode chemistry. *Nat Commun*. 2020;11(1):1550. doi:10.1038/s41467-020-15355-0
3. Toshiba Global, How lithium-ion batteries works?, access: 06.04.2022, https://www.global.toshiba/ww/products-solutions/battery/scib/product/module/sip/download/batteryschool/episode1.html
4. Yang Z, Xiang W, Wu Z, et al. Effect of niobium doping on the structure and electrochemical performance of LiNi0.5Co0.2Mn0.3O2 cathode materials for lithium ion batteries. *Ceram Int*. 2017;43(4):3866-3872. doi:10.1016/j.ceramint.2016.12.048
5. Liu S, Chen X, Zhao J, et al. Uncovering the role of Nb modification in improving the structure stability and electrochemical performance of LiNi 0.6 Co 0.2 Mn 0.2 O 2 cathode charged at higher voltage of 4.5 V. *J Power Sources*. 2018;374:149-157. doi:10.1016/j.jpowsour.2017.11.037
6. Xin F, Zhou H, Zong Y, et al. What is the Role of Nb in Nickel-Rich Layered Oxide Cathodes for Lithium-Ion Batteries? *ACS Energy Lett*. Published online March 18, 2021:1377-1382. doi:10.1021/acsenergylett.1c00190
7. Whittingham MS. The role of ternary phases in cathode reactions. *J Electrochem Soc*. 1976;123(3):315-320.
8. Mishra A, Mehta A, Basu S, et al. Electrode materials for lithium-ion batteries. *Mater Sci Energy Technol*. 2018;1(2):182-187. doi:10.1016/j.mset.2018.08.001

9. Julien C, Mauger A, Zaghib K, Groult H. Comparative Issues of Cathode Materials for Li-Ion Batteries. *Inorganics (Basel)*. 2014;2(1):132-154. doi:10.3390/inorganics2010132

10. GOODENOUGH J. Design considerations. *Solid State Ion*. 1994;69(3-4):184-198. doi:10.1016/0167-2738(94)90409-X

11. Wang J, Sun X. Understanding and recent development of carbon coating on LiFePO $_4$ cathode materials for lithium-ion batteries. *Energy Environ Sci*. 2012;5(1):5163-5185. doi:10.1039/C1EE01263K

12. Chen H, Hu Q, Huang Z, et al. Synthesis and electrochemical study of Zr-doped Li[Li0.2Mn0.54Ni0.13Co0.13]O2 as cathode material for Li-ion battery. *Ceram Int*. 2016;42(1):263-269. doi:10.1016/j.ceramint.2015.08.104

13. Basch A, de Campo L, Albering JH, White JW. Chemical delithiation and exfoliation of LixCoO2. *J Solid State Chem*. 2014;220:102-110. doi:10.1016/j.jssc.2014.08.011

14. G. Hu, K. Du, Z. Peng. Cathode Materials for Lithium Ion Batteries: Principle, Performance and Production Technology. *Beijing Industrial Publisher*. Published online 2017:103-133.

15. Nitta N, Wu F, Lee JT, Yushin G. Li-ion battery materials: present and future. *Materials Today*. 2015;18(5):252-264. doi:10.1016/j.mattod.2014.10.040

16. Arroyo y de Dompablo ME, Marianetti C, van der Ven A, Ceder G. Jahn-Teller mediated ordering in layered LixMO2compounds. *Phys Rev B*. 2001;63(14):144107. doi:10.1103/PhysRevB.63.144107

17. Shannon RD. Revised effective ionic radii and systematic studies of interatomic distances in halides and chalcogenides. *Acta Crystallographica Section A*. 1976;32(5):751-767. doi:10.1107/S0567739476001551

18. Ohzuku T, Ueda A, Nagayama M, Iwakoshi Y, Komori H. Comparative study of LiCoO2, LiNi Co O2 and LiNiO2 for 4 volt secondary lithium cells. *Electrochim Acta*. 1993;38(9):1159-1167. doi:10.1016/0013-4686(93)80046-3

19. Caurant D. Synthesis by a soft chemistry route and characterization of LiNixCo1−xO2 ($0 \leq x \leq 1$) cathode materials. *Solid State Ion*. 1996;91(1-2):45-54. doi:10.1016/S0167-2738(96)00418-3

20. Chen W, Li Y, Yang D, Feng X, Guan X, Mi L. Controlled synthesis of spherical hierarchical LiNi1−x−yCoxAlyO2 ($0<x, y<0.2$) via a novel cation exchange process as cathode materials for High-Performance Lithium Batteries. *Electrochim Acta*. 2016;190:932-938. doi:10.1016/j.electacta.2016.01.024

21. Duan J, Dong P, Wang D, et al. A facile structure design of LiNi0.90Co0.07Al0.03O2 as advanced cathode materials for lithium ion batteries via carbonation decomposition of NaAl(OH)4 solution. *J Alloys Compd*. 2018;739:335-344. doi:10.1016/j.jallcom.2017.12.236

22. Trease NM, Seymour ID, Radin MD, et al. Identifying the Distribution of Al^{3+} in $LiNi_{0.8}Co_{0.15}Al_{0.05}O_2$. *Chemistry of Materials*. 2016;28(22):8170-8180. doi:10.1021/acs.chemmater.6b02797

23. Park KJ, Hwang JY, Ryu HH, et al. Degradation Mechanism of Ni-Enriched NCA Cathode for Lithium Batteries: Are Microcracks Really Critical? *ACS Energy Lett*. 2019;4(6):1394-1400. doi:10.1021/acsenergylett.9b00733

24. Wang D, Liu W, Zhang X, Huang Y, Xu M, Xiao W. Review of Modified Nickel-Cobalt Lithium Aluminate Cathode Materials for Lithium-Ion Batteries. *International Journal of Photoenergy*. 2019;2019:1-13. doi:10.1155/2019/2730849

25. Yabuuchi N, Ohzuku T. Novel lithium insertion material of LiCo1/3Ni1/3Mn1/3O2 for advanced lithium-ion batteries. *J Power Sources*. 2003;119-121:171-174. doi:10.1016/S0378-7753(03)00173-3

26. Shaju KM, Subba Rao GV, Chowdari BVR. Performance of layered Li(Ni1/3Co1/3Mn1/3)O2 as cathode for Li-ion batteries. *Electrochim Acta*. 2002;48(2):145-151. doi:10.1016/S0013-4686(02)00593-5

27. Chakraborty A, Kunnikuruvan S, Kumar S, et al. Layered Cathode Materials for Lithium-Ion Batteries: Review of Computational Studies on $LiNi_{1-x-y}Co_xMn_yO_2$ and $LiNi_{1-x-y}Co_xAl_yO_2$. *Chemistry of Materials*. 2020;32(3):915-952. doi:10.1021/acs.chemmater.9b04066

28. Kim JM, Chung HT. The first cycle characteristics of Li[Ni1/3Co1/3Mn1/3]O2 charged up to 4.7 V. *Electrochim Acta*. 2004;49(6):937-944. doi:10.1016/j.electacta.2003.10.005

29. Li Z, Chernova NA, Roppolo M, et al. Comparative Study of the Capacity and Rate Capability of LiNiyMnyCo1–2yO2 (y = 0.5, 0.45, 0.4, 0.33). *J Electrochem Soc*. 2011;158(5):A516. doi:10.1149/1.3562212

30. Yoon WS, Balasubramanian M, Chung KY, et al. Investigation of the Charge Compensation Mechanism on the Electrochemically Li-Ion Deintercalated $Li_{1-x}Co_{1/3}Ni_{1/3}Mn_{1/3}O_2$ Electrode System by Combination of Soft and Hard X-ray Absorption Spectroscopy. *J Am Chem Soc*. 2005;127(49):17479-17487. doi:10.1021/ja0530568

31. Li J, Downie LE, Ma L, Qiu W, Dahn JR. Study of the Failure Mechanisms of $LiNi_{0.8}Mn_{0.1}Co_{0.1}O_2$ Cathode Material for Lithium Ion Batteries. *J Electrochem Soc*. 2015;162(7):A1401-A1408. doi:10.1149/2.1011507jes

32. Lee KS, Myung ST, Amine K, Yashiro H, Sun YK. Structural and Electrochemical Properties of Layered Li[Ni[1−2x]Co[x]Mn[x]]O[2] (x=0.1–0.3) Positive Electrode Materials for Li-Ion Batteries. *J Electrochem Soc*. 2007;154(10):A971. doi:10.1149/1.2769831

33. Noh HJ, Youn S, Yoon CS, Sun YK. Comparison of the structural and electrochemical properties of layered Li[NixCoyMnz]O2 (x = 1/3, 0.5, 0.6, 0.7, 0.8 and 0.85) cathode material for lithium-ion batteries. *J Power Sources*. 2013;233:121-130. doi:10.1016/j.jpowsour.2013.01.063

34. Xu L, Zhou F, Kong J, Chen Z, Chen K. Synthesis of Li(Ni0.6Co0.2Mn0.2)O2 with sodium DL-lactate as an eco-friendly chelating agent and its electrochemical performances for lithium-ion batteries. *Ionics (Kiel)*. 2018;24(8):2261-2273. doi:10.1007/s11581-017-2363-8

35. Venkatraman S, Shin Y, Manthiram A. Phase Relationships and Structural and Chemical Stabilities of Charged Li[1−x]CoO[2] and Li[1−x]Ni[0.85]Co[0.15]O[2] Cathodes. *Electrochemical and Solid-State Letters*. 2003;6(1):A9. doi:10.1149/1.1525430

36. Manthiram A. An Outlook on Lithium Ion Battery Technology. *ACS Cent Sci*. 2017;3(10):1063-1069. doi:10.1021/acscentsci.7b00288

37. Bak SM, Hu E, Zhou Y, et al. Structural Changes and Thermal Stability of Charged $LiNi_xMn_yCo_zO_2$ Cathode Materials Studied by Combined *In Situ* Time-Resolved XRD and Mass Spectroscopy. *ACS Appl Mater Interfaces*. 2014;6(24):22594-22601. doi:10.1021/am506712c

38. Qiao R, Liu J, Kourtakis K, et al. Transition-metal redox evolution in LiNi0.5Mn0.3Co0.2O2 electrodes at high potentials. *J Power Sources*. 2017;360:294-300. doi:10.1016/j.jpowsour.2017.06.009

39. Arai H. Reversibility of LiNiO2 cathode. *Solid State Ion*. 1997;95(3-4):275-282. doi:10.1016/S0167-2738(96)00598-X

40. Liu W, Oh P, Liu X, et al. Nickel-Rich Layered Lithium Transition-Metal Oxide for High-Energy Lithium-Ion Batteries. *Angewandte Chemie International Edition*. 2015;54(15):4440-4457. doi:10.1002/anie.201409262

41. Julien C, Mauger A, Zaghib K, Groult H. Comparative Issues of Cathode Materials for Li-Ion Batteries. *Inorganics (Basel)*. 2014;2(1):132-154. doi:10.3390/inorganics2010132

42. Dixit M, Markovsky B, Schipper F, Aurbach D, Major DT. Origin of Structural Degradation During Cycling and Low Thermal Stability of Ni-Rich Layered Transition Metal-Based Electrode Materials. *The Journal of Physical Chemistry C*. 2017;121(41):22628-22636. doi:10.1021/acs.jpcc.7b06122

43. Shannon RD, Prewitt CT. Effective ionic radii in oxides and fluorides. *Acta Crystallogr B*. 1969;25(5):925-946. doi:10.1107/S0567740869003220

44. Liu W, Oh P, Liu X, et al. Nickel-Rich Layered Lithium Transition-Metal Oxide for High-Energy Lithium-Ion Batteries. *Angewandte Chemie International Edition*. 2015;54(15):4440-4457. doi:10.1002/anie.201409262

45. Liu Z, Yu A, Lee JY. Synthesis and characterization of LiNi1−x−yCoxMnyO2 as the cathode materials of secondary lithium batteries. *J Power Sources*. 1999;81-82:416-419. doi:10.1016/S0378-7753(99)00221-9

46. Noh HJ, Youn S, Yoon CS, Sun YK. Comparison of the structural and electrochemical properties of layered Li[NixCoyMnz]O2 (x = 1/3, 0.5, 0.6, 0.7, 0.8 and 0.85) cathode material for lithium-ion batteries. *J Power Sources*. 2013;233:121-130. doi:10.1016/j.jpowsour.2013.01.063

47. Kasnatscheew J, Röser S, Börner M, Winter M. Do Increased Ni Contents in $LiNi_x Mn_y Co_z O_2$ (NMC) Electrodes Decrease Structural and Thermal Stability of Li Ion Batteries? A Thorough Look by Consideration of the Li^+ Extraction Ratio. *ACS Appl Energy Mater*. 2019;2(11):7733-7737. doi:10.1021/acsaem.9b01440

48. Dixit M, Kosa M, Lavi OS, Markovsky B, Aurbach D, Major DT. Thermodynamic and kinetic studies of $LiNi_{0.5} Co_{0.2} Mn_{0.3} O_2$ as a positive

electrode material for Li-ion batteries using first principles. *Physical Chemistry Chemical Physics*. 2016;18(9):6799-6812. doi:10.1039/C5CP07128C

49. Li J, Wang L, Zhang Q, He X. Synthesis and characterization of LiNi0.6Mn0.4−xCoxO2 as cathode materials for Li-ion batteries. *J Power Sources*. 2009;189(1):28-33. doi:10.1016/j.jpowsour.2008.12.046

50. Zhang X, Jiang WJ, Mauger A, Qilu, Gendron F, Julien CM. Minimization of the cation mixing in Li1+x(NMC)1−xO2 as cathode material. *J Power Sources*. 2010;195(5):1292-1301. doi:10.1016/j.jpowsour.2009.09.029

51. LI W, REIMERS J, DAHN J. In situ x-ray diffraction and electrochemical studies of Li1−xNiO2. *Solid State Ion*. 1993;67(1-2):123-130. doi:10.1016/0167-2738(93)90317-V

52. Sun YK, Noh HJ, Yoon CS. Effect of Mn Content in Surface on the Electrochemical Properties of Core-Shell Structured Cathode Materials. *J Electrochem Soc*. 2011;159(1):A1-A5. doi:10.1149/2.004201jes

53. Karunawan J, Floweri O, Santosa SP, Sumboja A, Iskandar F. Stable layered-layered-spinel structure of the Li1.2Ni0.13Co0.13Mn0.54O2 cathode synthesized by ball-milling assisted solid-state method. *Journal of Electroanalytical Chemistry*. 2022;907:116050. doi:10.1016/j.jelechem.2022.116050

54. Liang L, Du K, Peng Z, et al. Co–precipitation synthesis of Ni0.6Co0.2Mn0.2(OH)2 precursor and characterization of LiNi0.6Co0.2Mn0.2O2 cathode material for secondary lithium batteries. *Electrochim Acta*. 2014;130:82-89. doi:10.1016/j.electacta.2014.02.100

55. Wang L, Wu B, Mu D, et al. Single-crystal LiNi0.6Co0.2Mn0.2O2 as high performance cathode materials for Li-ion batteries. *J Alloys Compd*. 2016;674:360-367. doi:10.1016/j.jallcom.2016.03.061

56. Hwang BJ, Tsai YW, Carlier D, Ceder G. A Combined Computational/Experimental Study on LiNi $_{1/3}$ Co $_{1/3}$ Mn $_{1/3}$ O $_{2}$. *Chemistry of Materials*. 2003;15(19):3676-3682. doi:10.1021/cm030299v

57. Li T, Yuan XZ, Zhang L, Song D, Shi K, Bock C. Degradation Mechanisms and Mitigation Strategies of Nickel-Rich NMC-Based Lithium-Ion Batteries. *Electrochemical Energy Reviews*. 2020;3(1):43-80. doi:10.1007/s41918-019-00053-3

58. Eilers-Rethwisch M, Winter M, Schappacher FM. Synthesis, electrochemical investigation and structural analysis of doped Li[Ni0.6Mn0.2Co0.2-M]O2 (x = 0, 0.05; M = Al, Fe, Sn) cathode materials. *J Power Sources*. 2018;387:101-107. doi:10.1016/j.jpowsour.2018.02.080

59. Liu S, Dang Z, Liu D, Zhang C, Huang T, Yu A. Comparative studies of zirconium doping and coating on LiNi0.6Co0.2Mn0.2O2 cathode material at elevated temperatures. *J Power Sources*. 2018;396:288-296. doi:10.1016/j.jpowsour.2018.06.052

60. Park KJ, Jung HG, Kuo LY, Kaghazchi P, Yoon CS, Sun YK. Improved Cycling Stability of Li[Ni $_{0.90}$ Co $_{0.05}$ Mn $_{0.05}$]O $_{2}$ Through Microstructure Modification by Boron Doping for Li-Ion Batteries. *Adv Energy Mater*. 2018;8(25):1801202. doi:10.1002/aenm.201801202

61. Aurbach D, Srur-Lavi O, Ghanty C, et al. Studies of Aluminum-Doped LiNi $_{0.5}$ Co $_{0.2}$ Mn $_{0.3}$ O $_{2}$: Electrochemical Behavior, Aging, Structural Transformations, and Thermal Characteristics. *J Electrochem Soc*. 2015;162(6):A1014-A1027. doi:10.1149/2.0681506jes

62. Li Y, Su Q, Han Q, et al. Synthesis and characterization of Mo-doped LiNi 0.5 Co 0.2 Mn 0.3 O 2 cathode materials prepared by a hydrothermal process. *Ceram Int*. 2017;43(4):3483-3488. doi:10.1016/j.ceramint.2016.10.038

63. Xue L, Li Y, Xu B, et al. Effect of Mo doping on the structure and electrochemical performances of LiNi0.6Co0.2Mn0.2O2 cathode material at high cut-off voltage. *J Alloys Compd*. 2018;748:561-568. doi:10.1016/j.jallcom.2018.03.192

64. Huang Z, Wang Z, Jing Q, Guo H, Li X, Yang Z. Investigation on the effect of Na doping on structure and Li-ion kinetics of layered LiNi0.6Co0.2Mn0.2O2 cathode material. *Electrochim Acta*. 2016;192:120-126. doi:10.1016/j.electacta.2016.01.139

65. Xu G, Xue Q, Li J, et al. Understanding the enhanced electrochemical performance of samarium substituted Li[Li0.2Mn0.54−xSmxCo0.13Ni0.13]O2 cathode material for lithium ion batteries. *Solid State Ion*. 2016;293:7-12. doi:10.1016/j.ssi.2016.04.025

66. Kalaiselvi K, Paruthimal Kalaignan G. Structure and electrochemical performance of Samarium substituted LiNi1/3Mn1/3Co1/3O2 cathode materials for rechargeable lithium-ion batteries. *Journal of Materials Science: Materials in Electronics*. 2018;29(24):20703-20709. doi:10.1007/s10854-018-0210-y

67. Du R, Bi Y, Yang W, et al. Improved cyclic stability of LiNi0.8Co0.1Mn0.1O2 via Ti substitution with a cut-off potential of 4.5V. *Ceram Int*. 2015;41(5):7133-7139. doi:10.1016/j.ceramint.2015.02.026

68. Lee SW, Kim H, Kim MS, et al. Improved electrochemical performance of LiNi0.6Co0.2Mn0.2O2 cathode material synthesized by citric acid assisted sol-gel method for lithium ion batteries. *J Power Sources*. 2016;315:261-268. doi:10.1016/j.jpowsour.2016.03.020

69. Klein L, Aparicio M, Jitianu A, eds. *Handbook of Sol-Gel Science and Technology*. Springer International Publishing; 2017. doi:10.1007/978-3-319-19454-7

70. Lutterotti, L., MAUD Software. 1997.

71. Büyükburç, A., Development and characterization of high energy cathode materials for lithium-ion batteries, in Metallurgical and Materials Engineering. 2013, PhD. Thesis, Middle East Technical University. p. 148.

72. Savaş C., Ultrasonic sound assisted processing and characterization of li(ni-co-al) oxide as cathode active material for li-ion batteries, in Metallurgical and Materials Engineering. 2017, MSc Thesis, Middle East Technical University. p. 84.

73. Julien C, Mauger A, Zaghib K, Groult H. Optimization of Layered Cathode Materials for Lithium-Ion Batteries. Materials (Basel). 2016 Jul 19;9(7):595. doi: 10.3390/ma9070595.